

Fabrication and Optoelectronic Properties of
Y-Ba-Cu-O Thin Films with Different Oxygen Contents

by

Wei Xiong

Submitted in Partial Fulfillment of the Requirements

for the Degree

Doctor of Philosophy

Supervised by Professor Roman Sobolewski

Department of Electrical Engineering
The College
School of Engineering and Applied Sciences

University of Rochester

Rochester, New York

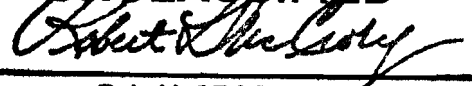
September 1995

Reviewed for Classification

11/6/95

(Date)

UNCLASSIFIED



R. L. McCRORY, JR.

Authorized Derivative Classifier

Curriculum Vitae

Wei Xiong was born on October 20, 1963 in China. After successfully passing in 1980 the country-wide entrance examination, he enrolled in Shanghai Jiao Tong University-one of the top engineering schools in China. He graduated with a B.S. and M.S.E.E. degrees in 1984 and 1987, respectively. After that, he was selected to participate the development of high density magnetic hard disk drives at the Center for Information Storage in Shanghai.

In fall of 1990, he was enrolled in the Ph.D program in the Department of Electrical Engineering at the University of Rochester. During his first year at Rochester, he was a teaching assistant. Since then, he has been a research assistant at the Laboratory for Laser Energetics (LLE) of the University of Rochester and was supported by the Frank Horton Fellowship Program. His research focuses on fabrication of high quality high-temperature superconducting (HTS) thin films and circuits, ultrafast spectroscopy of HTS, and the physics of HTS devices. His work on non-destructive laser patterning of HTS thin films was honored by the Meritorious Paper Award at the 10th International Cryogenic Materials Conference in Albuquerque, NM, July, 1993.

Mr. Xiong is a member of IEEE and OSA. He is the co-author of 17 journal publications and 14 conference communications (one invited).

Acknowledgments

I am greatly indebted to my thesis advisor, Professor Roman Sobolewski for his extraordinary guidance, support, and encouragement during my study at Rochester. His trust and interest in the direction of my research have been invaluable throughout this work.

I have been the most fortunate for the opportunity to work closely with the ultrafast group lead by Prof. Philippe M. Fauchet, whose high standard has guided my research in the area of ultrafast phenomena. I also want to thank Dr. Ting Gong, Yiogors Kostoulas, XiaoZhen Weng, Paul Rodney, and K. B. Ucer for their consistent assistance and advice on femtosecond laser systems. I want to thank ZhiWei Xu for valuable discussion on numerical simulations.

I am very appreciated of the opportunity to work with the electro-optical sampling group supervised by Prof. Thomas Y. Hsiang. For their assistance with the testing of photoconductive switching, I would like to thank Dr. Sotiris Alexandrou, Chia-Chi Wang, Marc Currie, Doug Jacob-Perkins, and Kenton Green.

For the assistance in YBCO fabrication and testing, I want to thank Dr. Witold Kula. I wish to thank Dr. Derek Mallory and Prof. Alan. M. Kadin for their support and help on thin film deposition, device fabrication and cryogenic testing.

For their professional assistance on manuscript and viewgraph preparation, I thank LaDonna Black's word processing group at LLE. For the patient and systematic support with reference reprints, I thank Linda Clement and Kenneth Harper at the LLE library. I would like to acknowledge the LLE's Frank Horton Fellowship Program and the AFOSR grant F49620-94-1-0094, which provided financial support for my research in Rochester.

Lastly, I want to thank my family members for their support and understanding.

ABSTRACT

Applications of high-temperature superconductors (HTS) demand not only high quality thin films with excellent electrical properties, but also appropriate patterning techniques. Conventional fabrication methods usually lead to a degradation of patterned HTS thin films, as a consequence of contamination, acid/water reaction, and physical damage of the film surface. In this work, we developed a non-destructive laser-writing technique for patterning $\text{YBa}_2\text{Cu}_3\text{O}_x$ (YBCO) thin films. We demonstrate that laser writing allows reproducible patterning of fine YBCO structures without the need for expensive photomasks and vacuum systems. Further, we investigated mechanisms of the optical response in YBCO for potential optoelectronic applications.

We have demonstrated that selective laser writing is capable of creating either a superconducting or insulating phase of YBCO. The patterned oxygen-rich lines exhibit the same superconducting properties as that of the as-deposited films, whereas the oxygen-depleted patterns are characterized by a semiconducting transport which is described by Mott's variable-range hopping. Since our laser-patterning is free of foreign contamination, patterns with the highest quality can be obtained. Moreover, the ability of erasing and rewriting patterns in this technique provides great flexibility for circuit restructuring and error correction. Laser-written structures are found to be stable for a period of over 2 years. Microwave testing confirmed the very low attenuation of our laser-written transmission lines.

Femtosecond pump-probe experiments have been performed on YBCO thin films with several oxygen contents. In semiconducting YBCO, band filling across the charge-transfer (CT) gap, as well as free-carrier absorption inside the O-2p band have been observed. Optical response in both white-light and low-temperature measurements was found to follow a stretched-exponential decay with a temperature-independent dispersion factor and a characteristic time which decreases with temperature. By separating the contributions from photo-induced bleaching and free-carrier absorption, we obtained the bandwidth of the O-2p band to be 1.9 eV.

Whereas the semiconductor-like CT transition still dominated the response of a 30-K YBCO sample, Fermi smearing governed the signals in films with higher oxygen doping levels. The Fermi level position was monitored as a function of the oxygen content and the observed signal sign dependence on the pump intensity was explained by a photoinduced shift in the Fermi level.

At temperatures below T_c , fast nonbolometric response was observed at low pump intensities while the slow bolometric term dominated at high intensities.

Table of Contents

<i>Curriculum Vitae</i>	<i>ii</i>
<i>Acknowledgments</i>	<i>iii</i>
<i>Abstract</i>	<i>iv</i>
<i>Table of contents</i>	<i>v</i>
<i>List of tables</i>	<i>vii</i>
<i>List of figure captions</i>	<i>viii</i>
<i>List of symbols and abbreviations</i>	<i>xi</i>
1. Introduction	1
1.1 High-temperature superconductors	1
1.2 Nonequilibrium superconductivity	4
1.3 Motivation	8
1.4 Thesis overview	9
2. Role of Oxygen in YBCO Compounds	16
2.1 Crystal structure	16
2.2 Superconducting and normal properties	18
2.3 Electronic structure	21
2.3.1 Theories	21
2.3.2 Optical investigations	23
3. Fabrication of YBCO Thin Films with Different Oxygen Contents	31
3.1 Overview of different deposition methods	31
3.2 Thin-film characterization	35
3.3 RF sputtering of 90 K and insulating YBCO thin films	36
3.4 Annealing of YBCO thin films	36
3.5 Electrical measurements	37
3.6 Microfabrication	40
3.7 Summary	40

4. Laser Processing of YBCO Films and Devices	47
4.1 Introduction	47
4.2 Technique	47
4.3 Oxygen diffusion in YBCO	49
4.4 Experimental	50
4.5 Results and discussion	51
4.5.1 Oxygen restoring	51
4.5.2 Oxygen removing	54
4.5.3 Pattern stability	56
4.5.4 Interface	56
4.5.5 Patterning of YBCO/SrTiO ₃ bilayers	59
4.6 Device fabrication and characterization	60
4.6.1 Microwave components	60
4.6.2 Photoconductive switch	62
4.7 Summary	64
5. Femtosecond Optical Response	69
5.1 Introduction	69
5.1.1 Pump-probe technique	69
5.1.2 Fermi smearing model	71
5.1.3 Nonequilibrium electron heating	73
5.2 Experimental	74
5.3 Results and discussion	76
5.3.1 Semiconducting YBCO	76
5.3.2 YBCO thin film with $T_c \approx 30$ K	82
5.3.3 YBCO thin film with $T_c \approx 60$ K	84
5.3.4 Fully oxygenated YBCO	89
5.3.5 Nonequilibrium superconductivity	90
5.4 Summary	92
6. Conclusions	98

LIST OF TABLES

<u>TABLE</u>	<u>Title</u>	<u>Page</u>
2.1	Lattice parameters for $\text{YBa}_2\text{Cu}_3\text{O}_x$	18
3.1	Physical Properties of Single-Crystal Substrates for HTS	34

LIST OF FIGURE CAPTIONS

<u>Figure</u>	<u>Title</u>	<u>Page</u>
1.1	A schematic plot of the order parameter and the resulting density of excitations for (a) an isotropic s-wave, and (b) a $d_{x^2-y^2}$ symmetry.	3
1.2	Photoexcitation dynamics in the superconducting state.	4
1.3	BCS QP recombination time as a function of temperature.	6
2.1	Crystal structure for $\text{YBa}_2\text{Cu}_3\text{O}_{6.0}$ and $\text{YBa}_2\text{Cu}_3\text{O}_{7.0}$.	17
2.2	Phase diagram of $\text{YBa}_2\text{Cu}_3\text{O}_{7-x}$.	19
2.3	Hubbard band model for the CuO_2 plane in YBCO. (a) $x < 6.4$ and (b) $x > 6.5$.	22
3.1	Schematic configurations for (a) PLD, and (b) off-axis sputtering methods.	32
3.2	Resistivity vs. temperature for sputtered YBCO films with various oxygen doping levels.	38
3.3	$\ln[R(T)/R(217\text{ K})]$ vs. $T^{-1/4}$ for the semiconducting sample shown in Fig. 3.2. The linear fit shows a variable-range hopping.	39
3.4	Schematic diagram of transport with trapping and hopping.	40
3.5	Flow chart of our lift-off procedure for patterning of YBCO circuits.	41
4.1	Schematic of a two-dimensional laser-writing system.	51
4.2	Optical transmission micrograph of a 7- μm -wide oxygen-rich microbridge laser patterned in a fully oxygen-depleted YBCO-on- LaAlO_3 film.	53
4.3	$R(T)$ and $J_c(T)$ curves of a 7- μm -wide laser-written microbridge.	53
4.4	Optical transmission micrograph of a semiconducting line overwritten on a previously patterned superconducting line.	54
4.5	Transport of a 10- μm -wide laser-written oxygen-poor gap (a) normalized R vs. T , and (b) normalized R vs. $T^{-1/4}$. The solid line represents a theoretical fit given by a 3-dimensional VRH.	55

4.6	Superconducting transitions of a YBCO microbridge measured over a period of 2 years.	57
4.7	A family of I-V characteristics of a 10- μm -long oxygen-poor YBCO structure. The inset shows the configuration of our test structure.	58
4.8	Oxygen concentration profile across laser-written YBCO structures with three different oxygen contents.	58
4.9	Laser-written patterns fabricated on YBCO/SrTiO ₃ bilayers: (a) two 35- μm -wide superconducting lines (dark region) cut by a perpendicular oxygen-depleted line (bright); and (b) part of a SuFET structure.	59
4.10	Optical micrograph of part of (a) a microwave resonator, and (b) a coplanar waveguide.	61
4.11	Transmitted powers S_{21} vs. frequency for a laser-written coplanar transmission line from room temperature to 24 K.	61
4.12	Semiconducting YBCO photoconductive switch: experimental set-up.	63
4.13	Room temperature response of an oxygen-depleted YBCO photoconductive switch with 4- μm spacing. Bias at 25.6 V.	63
5.1	Schematic of the Fermi smearing model. Photoinduced bleaching (PB) and absorption (PA) are observed by probe above and below the Fermi level, respectively.	71
5.2	Fermi smearing of differential signals. Energy zero is set to be $E_F - E_V$.	72
5.3	Experimental set-up of an ultrafast pump-probe system.	75
5.4	Converting n and k from ΔR and ΔT data taken from a semiconducting YBCO film.	75
5.5	Linear absorption spectrum of semiconducting YBCO. Solid dots in the inset are obtained from our pump-probe measurements.	77
5.6	Differential absorption of semiconducting YBCO at several probe energies. The smooth lines represent stretched-exponential fits.	78
5.7	$\Delta T/T$ of semiconducting YBCO at several temperatures. Fitting using $\Delta T/T = C_1 \exp[-(t/\tau)^\beta] + C_2$ is shown as smooth solid lines.	80

5.8	Stretched-exponential parameters for the data from Fig. 5.8. Solid lines are guides to the eye.	80
5.9	Differential absorption spectrum at several delays after the maximum bleaching.	81
5.10	Linear absorption spectrum of YBCO with $T_c=30$ K.	83
5.11	Transient reflection of YBCO with $T_c=30$ K.	83
5.12	Pump intensity dependence of a $T_c=30$ K YBCO thin film. Maximum intensity $I_0=300 \mu\text{J}/\text{cm}^2$. Probe at 1.91 eV.	84
5.13	Linear absorption spectrum of YBCO with $T_c=60$ K.	85
5.14	$\Delta R/R$ of a YBCO film with $T_c=55$ K. Pump at $300 \mu\text{J}/\text{cm}^2$.	85
5.15	$\Delta R/R$ of a YBCO film with $T_c=55$ K. Pump at $75 \mu\text{J}/\text{cm}^2$.	86
5.16	$\Delta R/R$ of a $T_c=60$ K YBCO thin film. Pump at $160 \mu\text{J}/\text{cm}^2$.	87
5.17	Pump intensity dependence of a $T_c=60$ K YBCO thin film Maximum intensity $I_0=300 \mu\text{J}/\text{cm}^2$. Probe at 2 eV.	87
5.18	Pump intensity dependence of a $T_c=60$ K YBCO thin film. Maximum intensity $I_0=160 \mu\text{J}/\text{cm}^2$. Probe at 1.91 eV.	88
5.19	Linear absorption spectrum of YBCO with $T_c=90$ K.	89
5.20	Normalized $\Delta R/R$ ($\sim 10^{-3}$) of an oxygen-rich YBCO thin film.	90
5.21	Normalized $\Delta R/R$ ($\sim 10^{-4}$) at $T=25$ K of (a) a 280-nm thick YBCO film with $T_c=89.5$ K and (b) a 80-nm thick YBCO film with $T_c=83$ K. The pump intensity was $\sim 1 \mu\text{J}/\text{cm}^2$.	91
5.22	Normalized $\Delta R/R$ ($\sim 10^{-3}$) at $T=12$ K measured on a 200-nm-thick YBCO film with $T_c=87$ K. The pump intensity was (a) $\sim 20 \mu\text{J}/\text{cm}^2$ and (b) $\sim 100 \mu\text{J}/\text{cm}^2$.	92

LIST OF SYMBOLS AND ABBREVIATIONS

<u>Symbols</u>	<u>Definition</u>
α	absorption coefficient
β	dispersion parameter
ω_D	Debye frequency
Θ	Debye temperature
$\lambda_{\langle\omega^2\rangle}$	electron-phonon coupling constant
Δ	charge-transfer gap, superconducting gap, deviation
Δ_0	unperturbed superconducting energy gap at zero K
ϵ_p	energy for O-2p band
ϵ_d	energy for Cu-3d upper Hubbard band
γ	quantum efficiency for quasiparticle creation
τ	characteristic time
τ_0	prefactor of characteristic time
τ_R	quasiparticle recombination time
τ_B	Cooper pairs breaking time
τ_γ	phonon trapping time
τ_{es}	phonon escaping time
$\tau_{s,ph}$	phonon scattering time
τ_s	relaxation time
τ_{eff}	effective relaxation time
σ	conductivity
σ_n	normal state conductivity
σ_s	superconducting state conductivity
ω_p	plasma frequency
\hbar	Plank constant
g	electron-phonon coupling constant
n	dimensionless quasiparticle number
k_B	Boltzmann constant
t	time, hopping integral
v	decay rate
x	oxygen content
$C_e (C_L)$	specific heat of electrons (lattice)
D, D_0	diffusion constant
E_a	activation energy
E_F	Fermi energy
E_g	semiconducting energy gap
F	Cooper interaction potential

I	current
J	exchange energy, current density
J_c	critical current density
N	dimensionality
N_F or $N(0)$	density of state at Fermi surface
p	numbers of hops
P	power, optical flux
R	resistivity, optical reflection
T	temperature, optical transmission
T_c	superconducting transition temperature
T_e (T_L)	electron (lattice) temperature
U	on site Coulomb repulsion energy
V	voltage, volume, interaction between Cu and O sites
W	hopping probability

Abbreviations**Definition**

<i>e-ph</i>	electron-phonon (coupling)
BCS	Bardeen-Cooper-Schrieffer theory of superconductivity
CPM	collide-pulse mode-lock laser
CT	charge transfer
CVD	chemical vapor deposition
DOS	density of states
EDX	energy dispersive x-ray analysis
FIR	far infrared
HTS	high-temperature superconductor(s)
LHB	lower Hubbard band
M-I	metal-insulator phase transition
MOCVD	metalorganic chemical vapor deposition
O-T	orthorhombic-tetragonal phase transition
PA	photoinduced absorption
PB	photoinduced bleaching
PL	photoluminescence
PLD	pulsed laser deposition
PPC	persistent photoconductivity
PVD	physical vapor deposition
QP	quasiparticles
SEM	scanning electron microscopy
SIMS	secondary ion mass spectroscopy
TEM	transmission electron microscopy
UHB	upper Hubbard band
XRD	x-ray diffraction
YBCO	high-temperature superconducting $YBa_2Cu_3O_x$ compound

1 INTRODUCTION

1.1 High-temperature superconductors

The discovery of high-temperature superconductors (HTS) nearly ten years ago [1.1, 1.2] brought a great challenge to the physics, chemistry, and materials science. Immense efforts have been made to understand the fundamental pairing mechanism behind the surprisingly high superconducting transition temperature (T_c) in HTS and to fabricate practical devices.

In conventional superconductors, the pairing mechanism has been successfully modeled by the Bardeen-Cooper-Schrieffer (BCS) theory of superconductivity [1.3]. According to BCS, two electrons interacting with a weak attraction via the electron-phonon ($e-ph$) coupling form a bound state (Cooper pair). The condensation of Cooper pairs leads to the superconducting state below T_c . Upon entering the superconducting state, a gap of 2Δ , which corresponds to the energy needed to break a Cooper pair, is opened at the Fermi surface. The energy gap is isotropic over 3 dimensions (s-wave). In the vicinity of T_c , BCS theory yields

$$\Delta(T) \approx 1.74\Delta(0)[1-T/T_c]^{1/2}, \quad (1.1)$$

where

$$2\Delta(0) \approx 4\hbar\omega_D \exp(-1/FN_F) \approx 3.52k_B T_c, \quad (1.2)$$

and

$$T_c = 1.13\Theta \exp(-1/FN_F), \quad (1.3)$$

where $\hbar\omega_D$ is the Debye energy for the phonons, Θ is the Debye temperature, F is the strength of Cooper interaction potential, and N_F is the density of states (DOS) at the Fermi level (E_F). Weak coupling corresponds to $FN_F \ll 1$. As temperature increases, the superconducting order parameter $\Delta(T)$ decreases continuously to zero. Therefore, superconducting transition is a *second order* phase transition.

In Eliashberg's approach (extended BCS theory) [1.4], the transition temperature is expressed as [1.5]

$$T_c \approx 0.18(\lambda \langle \omega^2 \rangle)^{1/2} \quad (1.4)$$

where $\lambda \langle \omega^2 \rangle$ is the $e-ph$ coupling strength.

The superconducting gap manifests itself as an abrupt change in the absorption spectrum. At energies below the gap, no photon absorption is possible. Only those photons with the energy larger than the gap can be absorbed. In

conventional superconductors, the gap opening has been experimentally confirmed by the measurements of the absorption spectrum [1.6]. The obtained Δ follows closely the prediction of the BCS theory [Eq.(1.2)].

For HTS, one obvious question is whether the BCS theory can explain properties of these new materials. A related issue is the confirmation of the gap opening. Unlike in conventional superconductors, far-infrared (FIR) absorption spectrum measurements haven't resolved any signature of the gap opening in HTS [1.7-1.9]. On the other hand, tunneling investigations seem to indicate the existence of the superconducting gap [1.10]. However, the obtained gap ratio $\Delta(T)/k_B T_c$ appears to be several times larger than that in conventional superconductors.

The difficulty that the BCS theory encounters in the case of HTS leads to speculations about various pairing mechanisms other than the phonon-mediated model. Among them, Hubbard models based on spin fluctuations have received particular attention [1.11-1.13]. One of the most appealing features of the Hubbard model is the prediction of long-range antiferromagnetic ordering which has been observed in the insulating phase of HTS [1.11, 1.12].

Further controversy involves the symmetry of $\Delta(T)$ in HTS. The BCS theory predicts an isotropic Δ function over the Fermi surface. However, magnetic pairing mechanisms expect a d-wave ($d_{x^2-y^2}$) symmetry in HTS [1.16, 1.17]. The d-wave symmetry leads to an anisotropic $\Delta(k)$ with nodes along certain directions. Figure 1.1 displays the major distinctions between conventional, isotropic s-wave (BCS-like) and d-wave superconductors.

For s-symmetry, the density of excited states is given by [1.18]

$$N(E) = N(0)E/(E^2-\Delta^2)^{1/2} , \quad (1.5)$$

where $N(0)$ is the density of states on the Fermi surface.

No excited states within the gap are allowed in the s-wave superconductors (Fig. 1.1a). Also, an activation energy on the order of 2Δ is required to excite quasiparticles (QP) out of the superconducting state. This thermally activated process determines that the QP number varies exponentially with temperature. By contrast, a gapless behavior is expected for superconductors with the d-wave symmetry (Fig. 1.1b). QP can be excited with any incrementally small energy. Therefore, the temperature dependence of the QP number should follow a power law rather than exponential [1.16].

Many parameters such as the heat capacity, scattering rate, and relaxation rate depend directly on the QP density. Difference in the temperature dependence of QP

between the d-wave and conventional s-wave superconductors will result in different temperature behavior of these parameters. Experiments capable of detecting those properties are pursued to distinguish between the s-wave and d-wave symmetries.

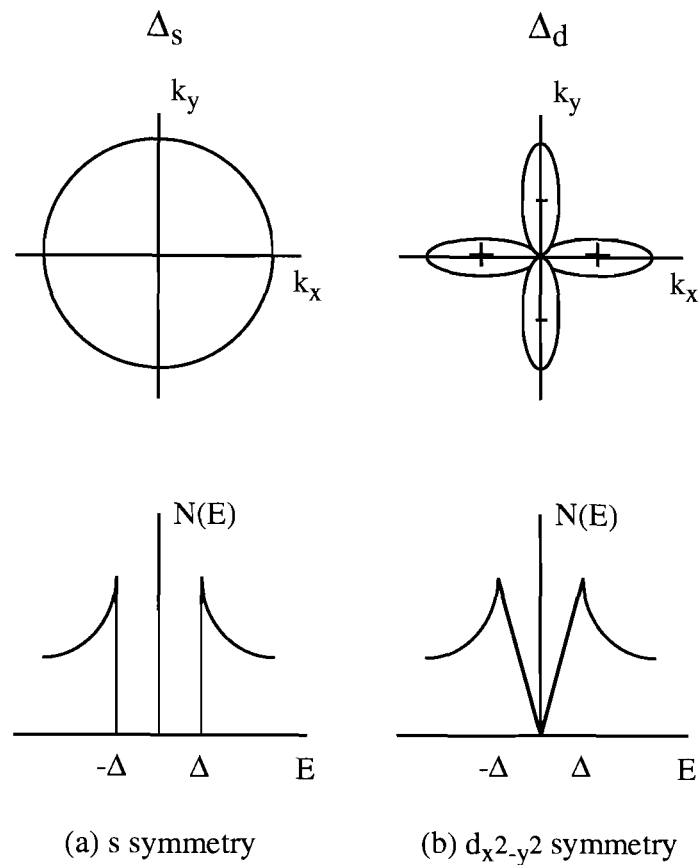


Fig. 1.1 A schematic plot of the order parameter and the resulting density of excitations for (a) an isotropic s-wave, and (b) a $d_{x^2-y^2}$ symmetry [1.15].

1.2 Nonequilibrium superconductivity

The ability to generate nonequilibrium superconducting states by short-pulse laser excitation permits direct observation of the relaxation process of the order parameter. Incident photons with energy greater than 2Δ can break Cooper pairs into QP with the excess energy of $\hbar\omega - 2\Delta$. The excited QP may lose their energy by either emitting low-energy phonons or breaking more Cooper pairs if the excess energy is higher than 2Δ . QP with lower energy may recombine to form Cooper pairs accompanied by the release of phonons with the excess energy of at least 2Δ (2Δ phonons). These 2Δ phonons trapped within the excited volume may further break Cooper pairs before escaping out of the film. Figure 1.2 shows schematically the complex three-body problem of photoexcitation dynamics in the superconducting state.

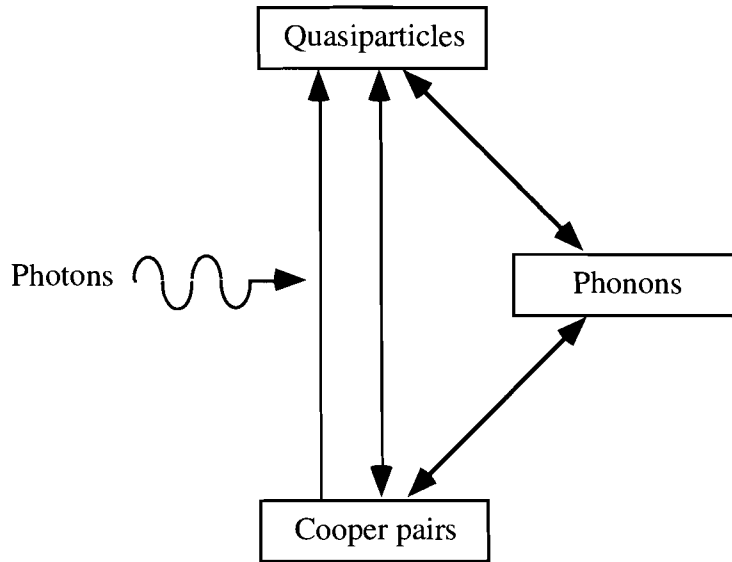


Fig. 1.2 Photoexcitation dynamics in the superconducting state.

QP recombination kinetics in superconductors was modeled by Rothwarf and Taylor using the following two rate equations [1.19]:

$$d(\delta N_{qp})/dt = -(\delta N_{qp})^2/\tau_R + 2(\delta N_{ph})/\tau_B, \quad (1.6a)$$

$$d(\delta N_{ph})/dt = (\delta N_{qp})^2/2\tau_R - (\delta N_{ph})/\tau_B - (\delta N_{ph})/\tau_\gamma, \quad (1.6b)$$

where δN_{qp} and δN_{ph} are the excess QP and 2Δ phonons released in the QP recombination process, respectively. τ_{R} , τ_{B} , and τ_{γ} are the QP recombination time, Cooper-pair breaking time, and phonon trapping time, respectively.

The phonon trapping time τ_{γ} is a combination of the time to escape from the sample (τ_{es}) and the time to scatter into low-energy phonons ($\tau_{\text{s}^{\text{ph}}}$) that are unable to break pairs, $\tau_{\gamma}^{-1} = (\tau_{\text{es}})^{-1} + (\tau_{\text{s}^{\text{ph}}})^{-1}$ [1.22]. In the weak perturbation limit, an effective time constant τ_{eff} is expressed as [1.22]

$$\tau_{\text{eff}} \approx \tau_{\gamma} + \tau_{\text{R}}[1 + \tau_{\gamma}/\tau_{\text{B}}]. \quad (1.7)$$

Breaking of Cooper pairs is a much faster process than the phonon escape ($\tau_{\text{B}} \ll \tau_{\gamma}$). Due to the slow phonon trapping, there is a significant enlargement ($\tau_{\gamma}/\tau_{\text{B}} \gg 1$) in τ_{R} . As is seen in Eq. (1.7), the recovery of nonequilibrium superconducting state is determined by τ_{γ} and τ_{R} .

The temperature dependence of τ_{R} can be explained in the context of the two-fluid model. Since the fraction of the normal state decreases as the temperature drops, less QP are available for recombination at lower temperatures. Moreover, the QP number is governed by the activation energy of the BCS gap. Hence, the recombination time is expected to increase exponentially with the temperature decrease. For gapless superconductors, however, the temperature dependence of the recombination time should follow a power law.

At temperatures close to T_{c} , photoexcitation may throw the whole system out of the superconducting state. The relaxation of Δ begins to influence the recovery process. As T_{c} is approached from the low temperature side, a divergence in τ_{R} is observed [1.20].

For superconductors with the BCS Δ , the τ_{R} in the vicinity of T_{c} is expected to change as [1.20]

$$\tau_{\text{R}} \sim \Delta^{-1}, \quad (1.8a)$$

while for a gapless superconductor, τ_{R} is expected to depend on Δ as [1.20]

$$\tau_{\text{R}} \sim \Delta^{-2}, \quad (1.8b)$$

Figure 1.2 shows schematically the temperature dependence of the BCS-like QP recombination time. Evidently, τ_{R} is larger at temperatures either far below T_{c} or very close to T_{c} . Experimental investigations have verified both the exponential

dependence at low temperatures [1.21] and the divergence near T_c [1.22] in conventional superconductors.

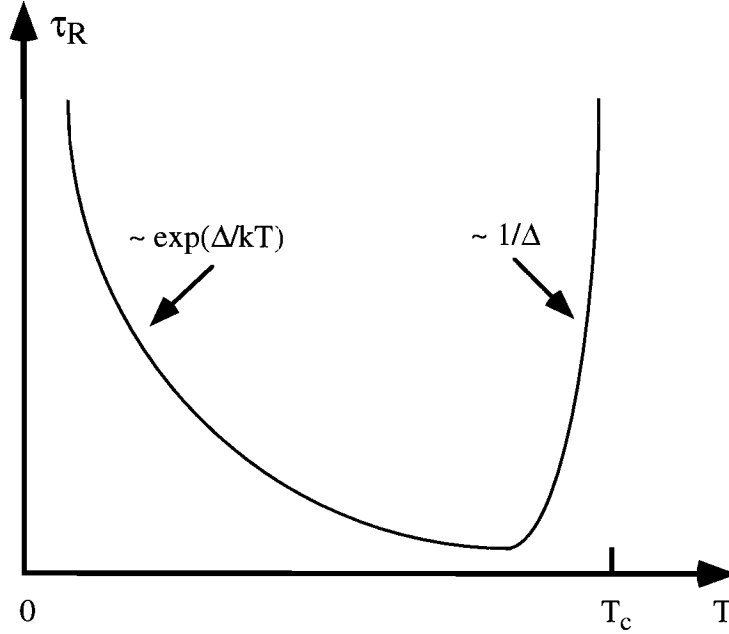


Fig. 1.3 BCS QP recombination time as a function of temperature.

Beside its temperature dependence, Δ also varies with the amount of excess QP. Sufficient QP injection can fully suppress the order parameter. For BCS-like superconductors, the perturbation of Δ and the resulting collapse of the superconducting state upon QP generation were modeled by Owen and Scalapino (μ^* model) [1.23]. Since the time for QP to recombine is much longer than the time for them to thermalize with respect to the lattice, Owen and Scalapino assumed that both paired and unpaired electrons are in thermal equilibrium with the lattice but not in chemical equilibrium with each other. The order parameter is expressed as a function of the excess QP number as

$$(\Delta/\Delta_0)^3 = \{[(\Delta/\Delta_0)^2 + n^2]^{1/2} - n\}^2, \quad (1.9)$$

where Δ_0 is the unperturbed energy gap at $T=0$, n is the dimensionless QP number in units of $4N(0)\Delta_0$.

As predicted by Eq. (1.9), the gap will decrease with the increase of excess QP until an abrupt *first-order* phase transition to the normal state occurs at a critical value

of n . Therefore, the superconducting state can be fully destroyed by sufficient QP injection.

For small n , Eq. (1.9) reduces to [1.24]

$$\Delta(n)/\Delta_0 \approx 1 - 2n, \quad (1.10a)$$

and

$$n = \gamma P \tau_R / [4N(0)\Delta_0 V], \quad (1.10b)$$

where γ is the number of QP produced per photon, P is the optical flux, and V is the volume of the illuminated superconductor.

Two straightforward predictions can be extracted from the μ^* model. First, the gap is expected to decrease proportionally to the optical intensity [Eq. (1.9)]. Second, Δ will decrease exponentially with temperature, because τ_R is approximately proportional to $\exp(\Delta/k_B T)$. Both of these predictions have been experimentally verified in conventional Sn-oxide-Sn tunnel junctions [1.24]. The predicted first-order transition has been also observed [1.25].

In addition to the μ^* model, a T^* model, which predicts a *second-order* phase transition upon QP injection, was developed by Parker [1.26]. At low QP density, the T^* model is similar to the μ^* model. At high QP injection level, however, the T^* model requires a much higher QP injection to suppress the superconductivity completely. Besides the μ^* model and T^* models, various other models were also developed to explain the nonequilibrium process in superconductors [1.27-1.29]. Elesin *et al.* developed an intermediate-state model which combined both the μ^* and T^* models [1.27]. Once the injection level is above a certain threshold, Elesin's model predicts an appearance of spatially inhomogeneous state that consists of superconducting and normal domains - so-called the intermediate state. The intermediate state was experimentally confirmed by Sobolewski *et al.* [1.28].

Femtosecond lasers are a powerful tool to generate nonequilibrium superconducting states. Femtosecond pump-probe technique has been applied to investigate the QP dynamics in HTS [1.30-1.38]. The relaxation times obtained from transient signals display a clear divergence near T_c , indicating the gap opening [1.30-1.36, 1.38]. However, there are controversies between different groups over the interpretations for the observed transients in HTS [1.33, 1.34, 1.38].

Han *et al.* reported that the temperature dependence of the maximum reflectivity change can be fitted nicely by the two-fluid model, but not the BCS theory [1.30]. However, Eesley *et al.* emphasized a BCS-like relaxation rate $\tau_s \sim T/\Delta(T)$

[1.31]. Moreover, Reitze *et al.* indicated that neither the simple two-fluid model nor the BCS theory are adequate to explain the transient photorefectivity response and the details of the electronic band structure have to be considered to interpret the magnitude and the sign of the measured optical transients [1.38].

Beside the gap investigation, femtosecond pump-probe studies of the normal state HTS offer the opportunity to obtain directly the *e-ph* coupling strength [1.38-1.41]. According to the model of nonequilibrium electron heating (will be discussed in detail in Chapter 5), relaxation process relies on the thermalization between the electron and lattice subsystems. Numerical fitting of the relaxation is used to extract *e-ph* coupling constant. In HTS, a consistent *e-ph* coupling strength ($\lambda\langle\omega^2\rangle$) has been found by various groups to be $\sim 400 \text{ meV}^2$ [1.38-1.41]. According to Eq. (1.4), this number is too small to account for the high T_c in HTS.

Femtosecond spectroscopy has been also applied to determine the position of E_F in HTS [1.37, 1.38, 1.42-1.44]. Due to the change in electron distribution function caused by laser heating (Fermi smearing), transients probed above and below E_F should correspond to photoinduced bleaching (PB) and absorption (PA), respectively. Hence, the sign change of the transient signals is considered an indication of probing across E_F . Even though the sign flip has been clearly observed in HTS, controversies over its dependence on pump intensity and oxygen doping remain.

In HTS, superconducting phase can be obtained by sufficient oxygen doping of the insulating phase. Hence, the parent, insulating phase plays the central role in all models of HTS and its electronic structure has been extensively studied by a variety of techniques. However, not until very recently, pump-probe investigations have been performed on insulating HTS samples and both PB and PA observed [1.45]. The fast component was assigned to the two-magnon scattering, whereas the origin of the PA signals below 1.6 eV remained unclear. More detailed studies have been conducted by us and will be presented in Chapter 5 of this thesis.

1.3 Motivation

Fabrication techniques are crucial for HTS applications [1.46-1.49]. Conventional semiconductor fabrication methods usually result in HTS patterns with degraded electrical parameters. Therefore, there is an urgent need for developing new patterning techniques dedicated to HTS.

The fabrication part of this work (Chapters 3 and 4) reflect our efforts to meet such a demand. Electrical and structural properties of HTS YBCO are very sensitive to its oxygen content. As a consequence, it is possible to selectively modify the oxygen content on a local scale by a focused laser beam. The oxygen-rich YBCO region is metallic above T_c and superconducting below the T_c . Whereas the oxygen-depleted area is insulating at low temperatures. In this thesis, a non-destructive laser-writing patterning technique has been developed to fabricate YBCO patterns with minimum degradation of their electrical properties. The technique has been proven to be a practical and reliable method of patterning YBCO thin films. Test devices have been fabricated to display the advantages of laser writing [1.50-1.55].

For optical applications of YBCO, it is of great interest to understand the physical origin of the photoresponse. The controversies in the earlier pump-probe observations have addressed the importance of band structure in the interpretation of the photoresponse signals in HTS. For the YBCO compound, the best understood band structure so far is that of the semiconducting phase. Hence, the studies of semiconducting YBCO help to understand how the optical response is related with the material's intrinsic properties. They should also shed light on the origin of optical response in highly oxygenated YBCO.

In this work, we performed extensive pump-probe investigations on semiconducting and superconducting YBCO thin films. The Hubbard band model has been applied to explain the observed optical response. By probing the optical response of YBCO samples with different oxygen contents, we managed to analyze the influence of oxygen doping on the Hubbard bands. We also studied the variation in Fermi energy upon doping by using the Fermi smearing model and investigated nonequilibrium states in superconducting samples illuminated by laser pulses.

1.4 Thesis overview

Following the introduction, we review in Chapter 2 the effects of oxygen stoichiometry on the crystal structure, band diagram, and electrical/optical properties of YBCO.

In Chapter 3, we discuss the deposition techniques developed for HTS thin films. We emphasize the *in situ* growth methods and report on the magnetron sputtering procedure which was used for our sample deposition. We also present how to prepare YBCO films with desired oxygen contents and test their electrical

properties as a function of temperature. We further outline a reliable photolithography process for patterning microstructures on YBCO thin films.

Chapter 4 focuses on our efforts in developing the laser-writing technique for non-destructive patterning of YBCO circuits and devices. We demonstrate how to selectively modify the oxygen content by local laser heating. We test electrical properties of our oxygen-rich and oxygen-depleted patterns. Microwave components and photoconductive switches fabricated by laser writing are also presented and their properties are discussed.

In Chapter 5, we study the femtosecond time-resolved optical response of YBCO thin films with several different oxygen contents. For semiconducting YBCO, we discuss the dominating sources of the optical response on the basis of the three-band Hubbard model. For partially oxygen-doped and oxygen-rich samples, we probe the position of the Fermi energy by combining the Fermi smearing model and the Hubbard model. The intensity dependence on the sign of the photoresponse signal is discussed. Finally, the existence of the nonequilibrium superconducting state in oxygen-rich YBCO films is studied.

Chapter 6 presents major conclusions coming from our work and directions for future investigations.

References

Discovery of HTS

- [1.1] J. G. Bednorz and K. A. Müller, "Possible high T_c superconductivity in the Ba-La-Cu-O system," *Z. Phys. B* **64**, 189 (1986)
- [1.2] M. K. Wu, J. R. Ashburn, C. J. Torng, P. H. Hor. R. L. Meng, L. Gao, Z. J. Huang, Y. Q. Wang, and C. W. Chu, "Superconductivity at 93 K in a new mixed phase Y-Ba-Cu-O compound system at ambient pressure," *Phys. Rev. Lett.* **58**, 908 (1987)

BCS Theory and Conventional superconductors

- [1.3] J. Bardeen, L. N. Cooper, and J. R. Schrieffer, "Theory of superconductivity," *Phys. Rev.* **108**, 1175 (1957)
- [1.4] P. B. Allen and B. Mitrovic, in *Solid State Physics*, v. **37**, p. 1, 1982
- [1.5] P. B. Allen, "Electron pairing: how and why?" in *High Temperature Superconductivity*, edited by J. W. Lynn, ch. 9, p.323, (Springer-Verlag, New York, 1990).
- [1.6] P. L. Richards and M. Tinkham, "Far-infrared energy gap measurements in bulk superconducting In, Sn, Hg, Ta, V, Pb, and Nb," *Phys. Rev.* **119**, 575 (1960)

FIR Spectrum and HTS gap

- [1.7] K. Kamaras, S. L. Herr, C. D. Porter, N. Tache, D. B. Tanner, S. Etemad, T. Venkatesan, E. Chase, A. Inam, X. D. Wu, M. S. Hegde, and B. Dutta, "In a clean high- T_c superconductor you do not see the gap," *Phys. Rev. Lett.* **64**, 84 (1990)
- [1.8] F. Gao, G. L. Carr, C. D. Porter, D. B. Tanner, S. Etemad, T. Venkatesan, A. Inam, B. Dutta, X. D. Wu, G. P. Williams, and C. J. Hirschmugl, "Far-infrared transmittance and reflectance studies of oriented $YBa_2Cu_3O_{7-\delta}$ thin films," *Phys. Rev. B* **43**, 10383 (1991)
- [1.9] D. Mandrus, M. C. Martin, C. Kendziora, D. Koller, L. Forro, and L. Mihaly, "No far-infrared-spectroscopic gap in clean and dirty high- T_c superconductors," *Phys. Rev. Lett.* **70**, 2629 (1993)
- [1.10] M. Lee, D. B. Mitzi, A. Kapitulnik, and M. R. Beasley, "Electron tunneling and the energy gap in $Bi_2Sr_2CaCu_2O_x$," *Phys. Rev. B* **39**, 801 (1989)

Hubbard Models

- [1.11] P. W. Anderson, "The resonating valence bond state in La_2CuO_4 and superconductivity," *Science* **235**, 96 (1987)

- [1.12] V. J. Emery, "Theory of high- T_c superconductivity in oxides," *Phys. Rev. Lett.* **58**, 2794 (1987)
- [1.13] S. Uchida, T. Ido, H. Takagi, T. Arima, Y. Tokura, and S. Tajima, "Optical spectra of $\text{La}_{2-x}\text{Sr}_x\text{CuO}_4$: effect of carrier doping on the electronic structure of the CuO_2 plane," *Phys. Rev. B* **43**, 7942 (1991)

Antiferromagnetic Ordering

- [1.14] J. M. Tranquada, D. E. Cox, W. Kunmann, H. Moudden, G. Shirane, M. Suenaga, and P. Zolliker, D. Vaknin, S. K. Sinha, M. S. Alvarez, A. J. Jacobson, and D. C. Johnston, "Neutron-diffraction determination of antiferromagnetic structure of Cu ions in $\text{YBa}_2\text{Cu}_3\text{O}_{6+x}$ with $x = 0.0$ and 0.15 ," *Phys. Rev. Lett.* **60**, 156 (1988)
- [1.15] K. B. Lyons, P. A. Fleury, L. F. Schneemeyer, and J. V. Waszczak, "Spin fluctuations and superconductivity in $\text{Ba}_2\text{YCu}_3\text{O}_{6+\delta}$," *Phys. Rev. Lett.* **60**, 732 (1988)

Order Parameter and Symmetry

- [1.16] R. C. Dynes, "The order parameter of high- T_c superconductors: experimental probes," *Solid State Commun.* **92**, 53 (1994)
- [1.17] J. R. Schrieffer, "Symmetry of the order parameter in high temperature superconductors," *Solid State Commun.* **92**, 53 (1994)
- [1.18] T. Van Duzer and C. W. Turner, in *Principles of Superconductive Devices and Circuits*, ch. 2, p. 71, (Elsevier North Holland, New York, 1981)

Nonequilibrium Process in BCS Superconductors

- [1.19] A. Rothwarf and B. N. Taylor, "Measurement of recombination lifetime in superconducting aluminum," *Phys. Rev. Lett.* **19**, 27 (1967)
- [1.20] I. Schuller and K. E. Gray, "Experimental observation of the relaxation time of the order parameter in superconductors," *Phys. Rev. Lett.* **36**, 429 (1976)
- [1.21] J. J. Chang and D. J. Scalapino, "Nonequilibrium superconductivity," *J. Low Temp. Phys.* **31**, 1 (1978)
- [1.22] M. Johnson, "Direct real time measurement of quasiparticle lifetimes in a superconductor," *Phys. Rev. Lett.* **67**, 374 (1991)
- [1.23] C. S. Owen and D. J. Scalapino, "Superconducting state under the influence of external dynamic pair breaking," *Phys. Rev. Lett.* **28**, 1559 (1972)
- [1.24] W. H. Parker and W. D. Williams, "Photoexcitation of quasiparticles in nonequilibrium superconductors," *Phys. Rev. Lett.* **29**, 924 (1972)

- [1.25] J. Fuchs, P. W. Epperlein, M. Welte, and W. Eisenmenger, "Energy gap reduction in superconducting tin films by quasiparticle injection," *Phys. Rev. Lett.* **38**, 919 (1977)
- [1.26] W. H. Parker, "Modified theory of nonequilibrium superconductors," *Phys. Rev. B* **12**, 3667 (1975);
- [1.27] V. F. Elesin, *Sov. Phys. JEPT* **39**, 862 (1974); A. I. Golovashkin, V. F. Elesin, O. M. Ivanenko, K. V. Mitsen, and G. P. Motulevich, "Conditions for the appearance of spatially inhomogeneous states in superconductors under laser pumping conditions," *Sov. Phys. Solid State* **22**, 60 (1980)
- [1.28] R. Sobolewski, D. P. Butler, T. Y. Hsiang, C. V. Stancampiano, and G. A. Mourou, "Dynamics of the intermediate state in nonequilibrium superconductors," *Phys. Rev. B* **33**, 4604 (1986)
- [1.29] I. Iguchi and H. Konno, "New instability model for the inhomogeneous gap states of a nonequilibrium superconductor," *Phys. Rev. B* **28**, 4040 (1983); Y. Nisida, T. Nishimura, A. Nishiura, and I. Iguchi, "Optical probing of the inhomogeneous gap distribution in nonequilibrium superconductors," *Solid State Commun.* **50**, 553 (1984); T. Kobayashi, S. Sawada, and K. Fujisawa, "Nonequilibrium superconductivity based on quasithermal phonon and quasiparticle distributions," *Phys. Rev. B* **31**, 6150 (1985)

Pump-Probe on HTS

- [1.30] S. G. Han, Z. V. Vardeny, O. G. Symko, and G. Koren, "Femtosecond optical detection of quasiparticle dynamics in high- T_c $\text{YBa}_2\text{Cu}_3\text{O}_{7-\delta}$ superconducting thin films," *Phys. Rev. Lett.* **65**, 2708, (1990)
- [1.31] G. L. Eesley, J. Heremans, M. S. Meyer, and G. L. Doll, "Relaxation time of the order parameter in a high-temperature superconductor," *Phys. Rev. Lett.* **65**, 3445, (1990)
- [1.32] J. M. Chwalek, C. Uher, J. F. Whitaker, and G. A. Mourou, "Femtosecond optical absorption studies of nonequilibrium electronic processes in high T_c superconductors," *Appl. Phys. Lett.* **57**, 1696, (1990)
- [1.33] S. G. Han, Z. V. Vardeny, O. G. Symko, and G. Koren, "Quasiparticle relaxation in a high- T_c superconductor," *Phys. Rev. Lett.* **67**, 1053 (1991)
- [1.34] G. L. Eesley, J. Heremans, M. S. Meyer, and G. L. Doll, "Eesley et al. reply:" *Phys. Rev. Lett.* **67**, 1054 (1991)
- [1.35] S. G. Han, Z. V. Vardeny, O. G. Symko, and G. Koren, "Femtosecond dynamics of quasi-particles in $\text{YBa}_2\text{Cu}_3\text{O}_{7-\delta}$ superconducting films," *IEEE Trans. Magn.* **MAG-27**, 1548 (1991)

- [1.36] S. V. Chekalin, V. M. Farztdinov, V. V. Golovlyov, V. S. Letokhov, Yu. E. Lozovik, Yu. A. Matveets, and A. G. Stepanov, "Femtosecond spectroscopy of $\text{YBa}_2\text{Cu}_3\text{O}_{7-\delta}$: electron-phonon-interaction measurement and energy-gap observation," *Phys. Rev. Lett.* **67**, 3860, (1991)
- [1.37] D. W. Face, S. D. Brorson, A. Kazeroonian, J. S. Moodera, T. K. Cheng, G. L. Doll, M. S. Dresselhaus, G. Dresselhaus, E. P. Ippen, T. Venkatesan, X. D. Wu, and A. Inam, "Femtosecond thermomodulation studies of low and high- T_c superconductors," *IEEE Trans. Magn.* **MAG-27**, 1556, (1991)
- [1.38] D. H. Reitze, A. M. Weiner, A. Inam, and S. Etemad, "Fermi-level dependence of femtosecond response in nonequilibrium high- T_c superconductors," *Phys. Rev. Lett.* **46**, 14306, (1992)
- [1.39] S. D. Brorson, A. Kazeroonian, J. S. Moodera, D. W. Face, T. K. Cheng, E. P. Ippen, M. S. Dresselhaus, and G. Dresselhaus, "Femtosecond room-temperature measurement of the electron-phonon coupling constant λ in metallic superconductors," *Phys. Rev. Lett.* **64**, 2172, (1990)
- [1.40] A. L. Dobryakov, V. V. Golovlev, V. S. Letokhov, Y. E. Lozovik, Y. A. Matveets, A. G. Stepanov, V. M. Farztdinov, and S. V. Chekalin, "Femtosecond spectroscopy of $\text{YBa}_2\text{Cu}_3\text{O}_{7-\delta}$ superconductors. Measurement of the electron-phonon coupling parameter and observation of the superconducting gap," *Optics and Spectroscopy* **76**, 871 (1994)
- [1.41] W-S. Zeng, W-Z. Lin, D. Mo, F. P. Pi, Z-J. Xia, Y-H. Zhou, and G-C. Xiong, Z. "Femtosecond relaxation dynamics of electronic processes and electron-phonon coupling in $\text{YBa}_2\text{Cu}_3\text{O}_{7-\delta}$ and $\text{PrBa}_2\text{Cu}_3\text{O}_7$ epitaxial films," *Phys. B* **96**, 5 (1994)
- [1.42] A. S. Kazeroonian, T. K. Cheng, S. D. Brorson, Q. Li, E. P. Ippen, X. D. Wu, T. Venkatesan, S. Etemad, M. S. Dresselhaus, and G. Dresselhaus, "Probing the Fermi level of $\text{Y}_{1-x}\text{Pr}_x\text{Ba}_2\text{Cu}_3\text{O}_{7-\delta}$ by femtosecond spectroscopy," *Solid State Commun.* **7**, 95, (1991)
- [1.43] T. Gong, L. X. Zheng, W. Xiong, W. Kula, Y. Kostoulas, R. Sobolewski, and P. M. Fauchet, "Femtosecond optical response of Y-Ba-Cu-O thin films: the dependence on optical frequency, excitation intensity, and electric current," *Phys. Rev. B* **47**, 14495, (1993)
- [1.44] W. Albrecht, Th. Kruse, K. Leo, and H. Kurz, "Oxygen dependence of the Fermi-level and electron-phonon coupling constant in $\text{YBa}_2\text{Cu}_3\text{O}_x$ films," *Appl. Phys. A* **56**, 463, (1993)

- [1.45] K. Matsuda, I. Hirabayashi, K. Kawamoto, and T. Nabatame, T. Tokizaki, and A. Nakamura, "Femtosecond spectroscopic studies of the ultrafast relaxation process in the charge-transfer state of insulating cuprates," *Phys. Rev. B* **50**, 4097 (1994)

HTS Microwave Devices

- [1.46] J. H. Winters, "High- T_c superconductor waveguides: theory and applications," *IEEE Trans. Microwave Theory and Techniques* **39**, 617 (1991)
- [1.47] N. Newman, W. G. Lyons, "High-temperature superconducting microwave devices: fundamental issues in materials, physics, and engineering," *J. Supercond.* **6**, 119 (1993)
- [1.48] K. H. Young, M. Robinson, G. V. Negrete, J. Zhao, C. S. Chern, Y. Q. Li, and P. E. Norris, "Microwave resonators from $\text{YBa}_2\text{Cu}_3\text{O}_{7-\delta}$ thin films made by plasma-enhanced metalorganic chemical vapor deposition," *Appl. Phys. Lett.* **61**, 543 (1992)
- [1.49] J. S. Martens, T. E. Zipperian, D. S. Ginley, V. M. Hietala, C. G. Tigges, and T. A. Plut, "The effects of processing sequences on the microwave surface resistance of TlCaBaCuO ," *J. Appl. Phys.* **69**, 8268 (1991)

Laser Writing

- [1.50] R. Sobolewski, W. Xiong, and W. Kula, "Patterning of thin-film high- T_c circuits by the laser-writing method," *IEEE Trans. Appl. Supercon.* **3**, 2896 (1993)
- [1.51] R. Sobolewski, W. Xiong, W. Kula, and J. R. Gavaler, "Laser patterning of Y-Ba-Cu-O thin-film devices and circuits," *Appl. Phys. Lett.* **64**, 643 (1994)
- [1.52] W. Xiong, W. Kula, and R. Sobolewski, "Fabrication of High- T_c superconducting electronic devices using the laser-writing technique," in *Advances in Cryogenic Engineering*, **40**, p. 385, edited by R. P. Reed et al., (Plenum Press, 1994).
- [1.53] W. N. Maung, D. P. Butler, W. Xiong, W. Kula, and R. Sobolewski, "Propagation characteristics of monolithic YBaCuO coplanar strip transmission lines fabricated by laser-writing patterning technique," *IEEE Microwave and Guided Wave Lett.* **4**, 132 (1994)
- [1.54] W. Kula and R. Sobolewski, "Charging effect in partially oxygen-depleted superconducting Y-Ba-Cu-O thin films," *Phys. Rev. B* **49**, 6428 (1994)
- [1.55] W. Kula, W. Xiong, and R. Sobolewski, "Laser patterning of $\text{YBa}_2\text{Cu}_3\text{O}_x$ thin films protected by *in-situ* grown SrTiO_3 cap layer," *IEEE Trans. Appl. Supercond.* **5**, 1177 (1995)

2 ROLE OF OXYGEN IN YBCO COMPOUNDS

Oxygen stoichiometry plays a key role in HTS. It determines crystal structures as well as the normal and superconducting properties of HTS. In YBCO compounds, these properties vary drastically with oxygen doping. In general, superconducting YBCO can be obtained by consequent doping of its parent semiconducting phase with oxygen. For oxygen content $x > 6.4$, YBCO is metallic above T_c and superconducting below T_c . The crystal structure is orthorhombic and belongs to space group Pmmm. In contrast, oxygen-poor YBCO ($x < 6.4$) is semiconducting at room temperature and virtually insulating at low temperature. Its crystal structure is tetragonal and belongs to space group P4/mmm. With increasing oxygen doping, the crystal structure changes from tetragonal for oxygen-poor YBCO to orthorhombic for oxygen-rich YBCO.

2.1 Crystal structure

Figure 2.1 shows the crystallographic structures for oxygen-depleted ($x \sim 6.0$) and oxygen-rich ($x \sim 7.0$) YBCO crystals [2.1]. The most important feature in YBCO is the existence of CuO_2 planes or layers, consisting of O(2)-Cu(2)-O(3) atoms. Another unique features are the Cu-O chains comprised of Cu(1)-O(1) sites and Cu(1)-O(4)-Cu(2) chains along the c -axis which interconnect the CuO_2 planes and Cu-O chains.

In oxygen-depleted YBCO, all of the chain O(1) sites are empty. At the intermediate oxygen level, oxygen atoms fill partially the chain O(1) sites and a portion of the chain O(5) sites which are in the middle of Cu(1) sites along the a -axis. Oxygen filling at O(5) leads to 3-fold Cu(1) bonding with the unstable $\text{Cu}^{+1.5}$ state [2.2]. Since the stable charge states for Cu are Cu^{+1} and Cu^{+2} , the unstable $\text{Cu}^{+1.5}$ state can either temporally fluctuate between Cu^{+2} and Cu^{+1} or spatially equilibrate with an appropriate number of Cu^{+1} and Cu^{+2} . Therefore, the oxygen atoms at O(5) tend to move to other empty O(1) sites to form the stable Cu^{+1} or Cu^{+2} states - a process which is often referred to as oxygen ordering. During oxygen ordering, long chain segments are favored from the energy point of view. Oxygen ordering plays an important role in the theory of photodoping and persistent photoconductivity observed in oxygen-depleted YBCO [2.3, 2.4]. It is also believed to be responsible for the aging effect of T_c after the annealing [2.7-2.13].

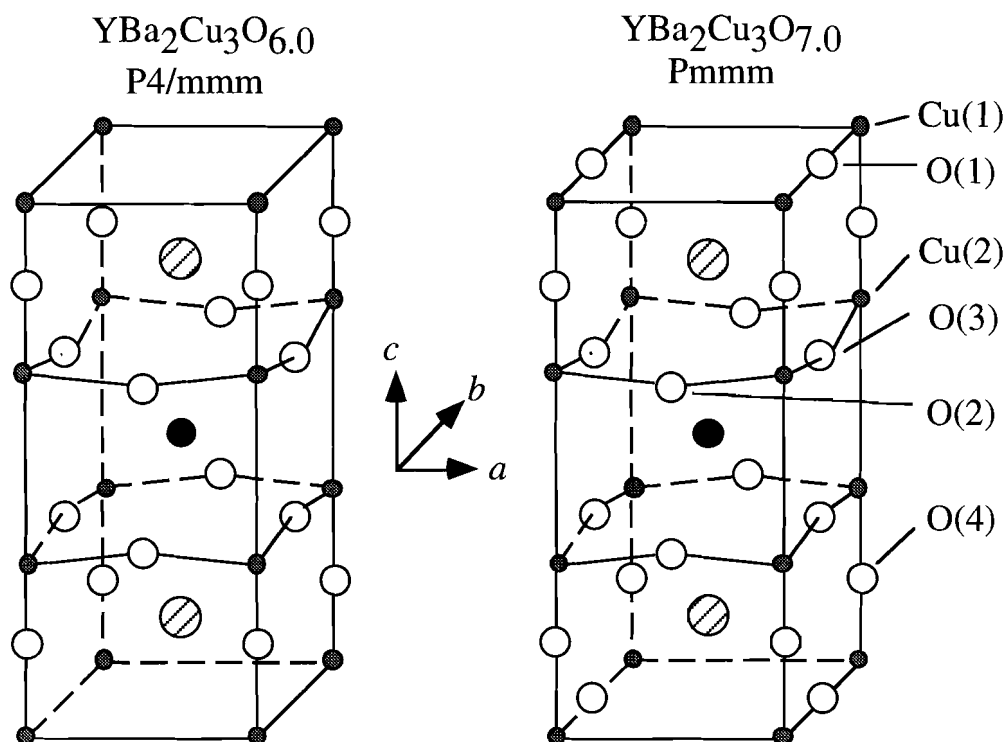


Fig. 2.1 Crystal structures for $\text{YBa}_2\text{Cu}_3\text{O}_{6.0}$ and $\text{YBa}_2\text{Cu}_3\text{O}_{7.0}$.

In oxygen-rich YBCO, the chain O(1) sites are fully occupied and the O(5) sites are vacant. The bonding at Cu(1) sites corresponds to the stable Cu^{+2} state. The strong anisotropy observed in oxygen-rich YBCO arise from the difference in oxygen occupancy between the a -axis and b -axis in the chain layers. Once the oxygen content is close to $x \sim 6.4$, phase transition between the orthorhombic and tetragonal structure occurs. Exact oxygen stoichiometry for the orthorhombic-tetragonal (O-T) transition depends on the sample preparation process.

Lattice constants corresponding to the tetragonal and orthorhombic phases are listed in Table 2.1. The anisotropy of the orthorhombic phase is evident in the difference between the lattice constants a and b . Moreover, oxygen doping causes a shrinkage in the c parameter vertical to the film plane. Such a reduction is crucial for the interlayer coupling between the CuO_2 layers.

Table 2.1 Lattice parameters for $\text{YBa}_2\text{Cu}_3\text{O}_x$ [2.1].

Phase	x	Space group	a (Å)	b (Å)	c (Å)
Tetragonal	6.07	P4/mmm	3.8570	3.8570	11.8194
Orthorhombic	~7.0	Pmmm	3.8198	3.8849	11.6762

2.2 Superconducting and normal properties

Beside the distinction in crystal structures, different oxygen content also leads to a significant variation in electrical properties of YBCO. For superconducting YBCO, T_c exhibits a remarkable correlation with the concentration of oxygen vacancies [2.5, 2.6]. Figure 2.2 shows a typical phase diagram of the YBCO system. Evidently, two plateaus of T_c appear, one at 60 K and the other at 90 K. The 60-K and 90-K plateaus are commonly observed in YBCO samples, regardless the sample preparation procedure, and are often referred to as the 60-K phase and the 90-K phase, respectively. The 90-K phase exists for oxygen-rich YBCO ($6.8 < x < 7.0$) whereas the 60-K phase occurs for partially doped YBCO ($6.5 < x < 6.8$). The transition between the 60-K and 90-K phases is so sharp that samples with T_c in between are difficult to prepare. Near $x=6.4$, metal-insulator (M-I) transition occurs in analogy with the O-T transition. Below the transition ($x < 6.4$), YBCO becomes semiconducting or insulating at low temperatures.

YBCO samples with the intermediate T_c can be prepared by controlling the oxygen content through a variety of annealing processes. Reliable annealing methods in either oxygen or an oxygen-free atmosphere have been reported [2.7-2.13]. Right after the annealing, an aging of T_c is commonly observed at both low and room temperatures [2.8]. During the aging process, T_c increases gradually with time. The shift in T_c is found to follow a stretched-exponential equation

$$T_c(t) = T_c(\infty) - [T_c(\infty) - T_c(0)]\exp[-(t/\tau)^{1/2}], \quad (2.1a)$$

and the characteristic time τ is found to be governed by a thermally activated process

$$\tau = \tau_0 \exp(E_a/k_B T), \quad (2.1b)$$

where E_a is the activation energy and is estimated to be 0.96 eV from the fitting, and $\tau_0=1.4$ ps.

At room temperature, the typical time scale of τ for a $x\approx 6.45$ sample is about 500 min. Therefore, T_c increases drastically in the first few hours after the annealing and slowly saturates after a few days. The amount of the T_c shift depends strongly on the oxygen content [2.8]. Maximum shift occurs near the M-I transition. For $x<6.6$, the T_c shift grows linearly with the increasing of oxygen vacancies to as high as 10 K at $x\approx 6.4$. For oxygen doping $x>6.6$, however, only a very small shift of $\Delta T_c\sim 2$ K is observed. Clearly, the T_c shift shares the same oxygen dependence as the occupancy of the O(5) sites. Thus, T_c aging must originate from the oxygen ordering [2.8].

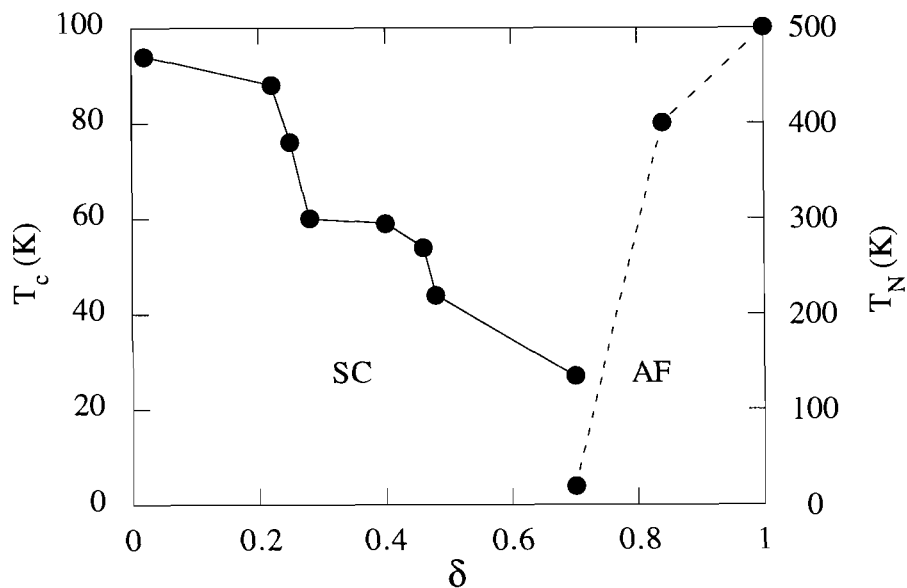


Fig. 2.2 Phase diagram of YBa₂Cu₃O_{7-δ} (adapted from Ref. 2.5).

There is a significant difference in the electrical conductivity between oxygen-rich and oxygen-depleted YBCO. In the normal state, oxygen-rich YBCO shows a metallic behavior with a linear resistance-temperature dependence. On the other hand, oxygen-depleted YBCO ($x<6.4$) shows a semiconductor behavior. At low

temperatures, its resistivity follows Mott's variable-range hopping (VRH) [2.13], with the sheet resistivity higher than 10 M Ω /square.

The theory of VRH developed by Mott has been applied to a broad range of materials, including transition-metal oxides, sulfides, alkali-halides, and doped semiconductors. It has successfully depicted another important category of temperature dependence other than the thermally activated exponential processes. Because of its importance in the transport of insulating YBCO, we briefly review the Mott's VRH theory.

For two impurities separated by R in real space, the probability W of phonon-assisted hopping due to acoustic phonons can be expressed as [2.13]

$$W \sim \exp(-2\alpha R) \exp[-\Delta E/(k_B T)] , \quad (2.2)$$

where ΔE is the average energy needed to hop to the nearest neighboring impurities.

If the electron hops a much larger distance (say pR with $p \gg 1$), it has a choice of p^N as many sites, where N is the dimensionality. Therefore, it may find some sites with energy much closer to its own. With an energy difference of $\Delta E/p^N$, the hopping probability is

$$W \sim \exp[-2\alpha pR - \Delta E/(p^N k_B T)] , \quad (2.3a)$$

and the maximum probability corresponds to

$$p^{N+1} = N\Delta E/(2\alpha R k_B T) . \quad (2.3b)$$

If p is greater than unity, the VRH probability is no longer proportional to $\exp(-\Delta E/k_B T)$ but to

$$W \sim \exp[-(\alpha R)^{N/(N+1)} (\Delta E/k_B T)^{1/(N+1)}] . \quad (2.3c)$$

Correspondingly, the conductivity is expressed as

$$\sigma(T) = \sigma(T_0) \exp[-(T_0/T)^{1/(N+1)}] . \quad (2.4)$$

Therefore, the temperature dependence of the conductivity can be used to distinguish between the thermal activated process and Mott's VRH.

2.3 Electronic structure

2.3.1 Theories

We have already mentioned that the most common feature in HTS compounds is the existence of two-dimensional CuO_2 planes. Within the CuO_2 planes, an antibonding band is formed by the Cu-3d and O-2p electrons. Generally, CuO_2 planes are accepted as the conducting planes and the location for the Cooper pair density [2.14]. According to the high-energy electron energy-loss spectroscopy, the dominant bands in the CuO_2 plane arise from the σ -bonding between the Cu- $3d_{x^2-y^2}$ and O- $2p_{x,y}$ orbitals [2.15].

In semiconductors, band-diagram calculations using one-electron approximation have successfully predicted their electronic properties. One-electron approximation has also been applied to YBCO [2.16-2.19]. For oxygen-rich YBCO, the calculations yield a band structure consisting of two bands for the CuO_2 plane and two other bands for the Cu-O chain. Although these calculations reproduced the metallic behavior of oxygen-rich YBCO, they failed to predict the semiconducting properties and the long-range antiferromagnetic ordering in undoped YBCO. The latter fact suggests the strong correlation within the electronic system.

To account for the high electron correlation, Hubbard models based on spin fluctuations were proposed for the band structure of HTS [2.20-2.22]. Within the framework of the Hubbard model, the electronic structure of the CuO_2 plane is modeled by a two-dimensional lattice consisting of Cu ($3d_{x^2-y^2}$) and O ($2p_x$) or O ($2p_y$) electrons. The antiferromagnetic ordering originates from the half filling of the CuO_2 planes. Despite the controversy over the choice between the one-band [2.20] and extended three-band [2.21] Hubbard models, the three-band Hubbard model has been generally accepted in the field of optical excitations.

For the extended Hubbard model [2.21], both the diagonal and off-diagonal terms are included in the Hamiltonian. The site-diagonal terms (ϵ_{ii} , U_{ii}) are (ϵ_p , U_p) and (ϵ_d , U_d) for O(2p) and Cu(3d) states, respectively. The nonvanishing off-diagonal terms $\epsilon_{ij}=\pm t$ and $U_{ij}=V$ are the hopping integrals and the interaction between neighboring Cu and O sites, respectively.

Figure 2.3 plots a schematic of three-band Hubbard diagram for a YBCO compound. The Cu-3d band is split by the on-site Coulomb repulsion into a upper Hubbard band (UHB) and a lower Hubbard band (LHB). The O-2p band resides between the UHB and LHB. In undoped YBCO, the O-2p band is fully occupied and

the Cu-3d UHB is empty. A charge-transfer (CT) gap E_{CT} of about 1.75 eV separates the O-2p band and the Cu-3d UHB. Since the on-site Coulomb repulsion $U \sim 8$ eV is much larger than the CT energy Δ ($U \gg \Delta$), the undoped YBCO is defined as a charge-transfer insulator [Fig. 2.3(a)] instead of a Mott-Hubbard insulator where $U \ll \Delta$. The minimum energy for interband transitions across the CT gap is estimated by $E_{CT} \approx 2(\Delta^2 - 4t^2)^{1/2}$ [2.21, 2.23].

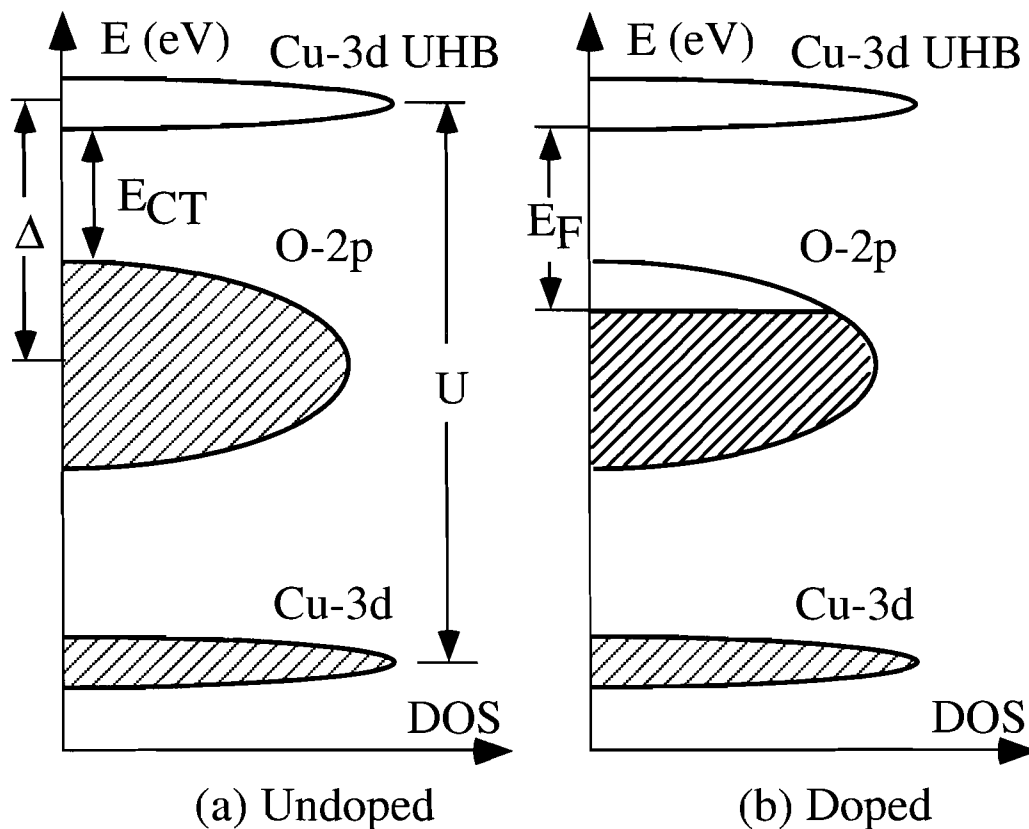


Fig. 2.3. The Hubbard band model for the CuO_2 plane in YBCO.
(a) $x < 6.4$, and (b) $x > 6.5$.

The Hubbard model has been successful in predicting the antiferromagnetic ordering and semiconducting properties in oxygen-depleted YBCO. For doped YBCO, however, the band structure is still a subject of continuing debate. Issues regarding how the Hubbard bands vary with oxygen doping are unclear. If the Hubbard bands are assumed to remain unchanged in the doped system (rigid-band

assumption), the Fermi level is predicted to move into the middle of the O-2p band. In this way, conducting holes are introduced to the CuO₂ plane (Fig. 2.3b). Moreover, the rigid-band assumption predicts that Fermi energy is a function of the oxygen content. Therefore, experimental monitoring of the Fermi energy upon oxygen doping will be insightful to understand the band model. Since the CT gap energy is on the order of the visible light, optical investigations are considered the most intuitive way to probe the CT band structure. Indeed, among the abundant studies reported, most of them were related with the parent semiconducting phase of YBCO where the band structure is best described by the Hubbard model.

2.3.2 Optical investigations

CT gap has been confirmed by a variety of experimental observations. In the reflectance spectra of YBCO, a fundamental absorption peak near 1.75 eV was observed at room-temperature in insulating YBCO [2.24]. Also observed was a strong transition at 4.1 eV which is believed to come from several out-of-plane transitions including intra-atomic transitions on the Cu(1) site, Cu(1)-O(4) transitions, and Ba-O(4) excitations. Furthermore, the optical reflectance in the *ab* plane was investigated with respect to the oxygen doping level [2.24]. In general, doping causes a loss of spectral weight above the CT gap and a development of low-energy absorption. The increase in plasma frequency was considered as an indication of the increased effective numbers of electrons by doping. A linear relation was obtained between the effective electron numbers and the oxygen content.

Raman scattering has been a powerful tool in studying the electronic structure of YBCO. The long-range antiferromagnetic ordering in undoped YBCO was verified by the resolved two-magnon feature at 2650-cm⁻¹ in the Raman spectra [2.25-2.29]. In a two-dimensional antiferromagnetic system, the interaction between the spins and the excitation photon can be described by a three-step process [2.26]: first, an electric-dipole transition of a Cu-d electron; then, a superexchange to a neighboring Cu-d electron via oxygen; and finally, a second electric-dipole transition emitting a photon. The strength of the two-magnon scattering arises from the two subsequent spin flips. The exchange energy $J \approx 950 \text{ cm}^{-1}$ was also obtained from the peak position of the two-magnon scattering [2.25]. Since two-magnon scattering originates from the long-range antiferromagnetic ordering, it relies strongly on the oxygen content in YBCO [2.26]. Its peak magnitude decreases with the increased oxygen doping and disappears once the M-I transition is reached ($x \approx 6.4$). Moreover,

the two-magnon peak for YBCO near the M-I transition shows an aging behavior as a result of oxygen ordering.

Besides two-magnon scattering, another high-order process, namely two-phonon scattering, has also been observed in YBCO [2.27-2.29]. The Raman shift for the two-phonon scattering is nearly twice that of the fundamental phonons in insulating YBCO.

Both two-magnon and two-phonon processes are sensitive to the excitation energy. It was found that with excitations close to the CT gap, two-phonon peaks were enhanced while the two-magnon peak was suppressed [2.28, 2.29]. The strong suppression of the two-magnon peak near the CT gap is consistent with the fact that CT transition corresponds to carrier excitations from oxygen to copper and not between the Cu UHB and LHB [2.28].

Resonant Raman scattering in insulating YBCO showed resonance features near 1.7, 2.1, and 2.5 eV which were assigned to the in-plane CT excitations [2.30]. Corresponding band diagrams based on the extended Hubbard model have been developed for both the undoped and oxygen-rich YBCO.

A strong Raman feature with A_{2g} symmetry has been resolved near the CT gap [2.31]. From the symmetry point of view, it has been assigned to either intra-atomic transitions between the Cu-d orbitals ($d_{x^2-y^2}$ to d_{xy}) or photon-assisted d to p_{σ} transition followed by photon-assisted p_{σ} to p_{π} hole hopping. In the latter case, a linear combination of neighboring p_{π} holes is required to attain the correct phase match with the center $d_{x^2-y^2}$ hole. Moreover, the A_{2g} feature displays a dependence on the oxygen content. The distinct peak at $x \sim 6.1$ remains nearly unchanged until oxygen doping reaches $x \sim 6.3$. Once $x > 6.6$, the A_{2g} peak disappears.

Further, the Raman spectrum excited at 1.16 eV displays a group of three features which are sensitive to oxygen doping. With the increase of oxygen content, the center peak at 507 cm^{-1} becomes dominant and associates with several overtones. The shift and strength variation is assigned to A_g vibration of the apex O(4) atoms adjacent to the O(1) sites which are filled upon doping [2.32].

Beside Raman scattering, other optical investigations have also been performed on YBCO. Photoluminescence (PL) has resolved deep intragap states in semiconducting YBCO [2.32]. With a 2.54 eV excitation, a midgap PL emission was observed near 1.3 eV. The PL peak dropped significantly when the oxygen content increased from $x \sim 6.0$ to $x \sim 6.15$. Recombination between the exciton level below the UHB and the deep intragap states are believed to be responsible for the PL emission.

A band model based on the above investigation has been proposed for undoped YBCO.

Photoconductivity studies of insulating YBCO have observed similar spectral features near 1.75, 2.7, and 4.2 eV as that of optical conductivity [2.33, 2.34]. The coincidence between the photoconductivity and optical conductivity spectra implies that CT transition results in mobile carriers (separate charges) rather than neutral excitons. In addition, the 1.5-eV feature resolved in low-temperature photoconductivity determines the lowest interband CT transition. The 1.5-eV feature is found to exist over a broad oxygen range for $6.0 < x < 6.3$.

While optical conductivity still demonstrates a strong peak at 1.7 eV for YBCO with oxygen content $x \sim 6.3$, the photoconductivity is weak below 2 eV [2.33]. It is concluded that electronic states involving the 1.5- and 1.7-eV transitions are localized for $x \sim 6.3$ -6.4. Consequently, CT insulator, Fermi glass, and metallic band diagrams have been proposed for oxygen-depleted, intermediate doping level, and oxygen-rich YBCO systems, respectively. Moreover, transient photoconductivity investigations showed that photoexcited carriers in insulating YBCO have lifetime on the order of 10 ns [2.34].

In addition to oxygen doping, an increase in carrier density can be achieved via photodoping of oxygen-poor YBCO. Photodoping has been observed in YBCO system over a broad range of oxygen contents ($6.35 < x < 6.70$) [2.35-2.39]. The resistivity of YBCO was found to decrease substantially under the exposure of visible light. Such a decrease in resistivity persists at low temperatures. Prolonged light irradiation leads to the full loss of resistivity or an enhancement in T_c . The relaxation of the photodoping effect has been found to follow a stretched-exponential decay [2.35]:

$$\Delta\sigma(t) = \Delta\sigma(0)\exp[-(t/\tau)^\beta], \quad (2.5a)$$

where τ is the characteristic decay time, β is the dispersion parameter.

The dispersion parameter can be well fitted with an empirical linear function between temperatures of 270 and 330 K

$$\beta(T) = -0.63 + T/264.6. \quad (2.5b)$$

The characteristic decay time can be described by thermally activated relaxation across an energy barrier as [2.35]

$$\tau = \tau_0 \exp(E_a/k_B T). \quad (2.5c)$$

where activation energy $E_a=0.935$ eV, and $\tau_0=1.4$ ps. Coincidentally, these values are very close to that obtained from investigations on the T_c aging and oxygen ordering (see Sec. 2.2).

From the value of β obtained in the photodoping effect, the width of the trap distribution in the sample was estimated by Eq. (2.8a) to be ~ 0.1 eV [2.35].

Currently, there are two competing mechanisms proposed for photodoping: photoinduced charge transfer [2.35] and photo-assisted oxygen ordering [2.3, 2.35]. The first mechanism emphasizes the photoexcitation inside the CuO_2 plane. The excited electrons are transferred to the adjacent CuO chains and trapped in the localized O^- levels. As a consequence, unpaired photoinjected holes contribute to the total concentration of free holes in the CuO_2 planes. Oxygen ordering mechanism favors photoexcitation within the CuO_x chain layer. Photo assisted oxygen defect ordering tends form longer chain segments. The result is the charge transfer of additional holes to the CuO_2 plane. As in the previous case, an increase in the sample conductivity is expected.

References

Crystal Structure

- [2.1] A. Santoro, "Crystallography: the system $\text{Ba}_2\text{MCu}_3\text{O}_8$ ($M = \text{Y, Gd, Eu, etc.}$)," in *High Temperature Superconductivity*, edited by J. W. Lym, (Springer-Verlag, New York), p. 105, 1990

Oxygen Ordering

- [2.2] N. Chandrasekhar, O. T. Valls, and A. M. Goldman, "Charging effects observed in $\text{YBa}_2\text{Cu}_3\text{O}_{7-x}$ films: influence of oxygen ordering," *Phys. Rev. B* **39**, 6619 (1989)
- [2.3] G. Nieva, E. Osquiguil, J. Guimpel, M. Maenhoudt, B. Wuyts, Y. Bruynseraede, M. B. Maple, and I. K. Schuller, "Photoinduced enhancement of superconductivity," *Appl. Phys. Lett.* **60**, 2159 (1992)
- [2.4] E. Osquiguil, M. Maenhoudt, B. Wuyts, Y. Bruynseraede, D. Lederman, and I. K. Schuller, "Photoexcitation and oxygen ordering in $\text{YBa}_2\text{Cu}_3\text{O}_x$ films," *Phys. Rev. B* **49**, 3675 (1994)

Phase Diagram

- [2.5] J. Zaanen, A. T. Paxton, O. Jepsen, and O. K. Andersen, "Chain-fragment doping and the phase diagram of $\text{YBa}_2\text{Cu}_3\text{O}_{7-x}$," *Phys. Rev. Lett.* **60**, 2685 (1988)
- [2.6] J. D. Jorgensen, B. W. Veal, A. P. Paulikas, L. J. Nowicki, G. W. Crabtree, H. Claus, and W. K. Kwok, "Structural properties of oxygen-deficient $\text{YBa}_2\text{Cu}_3\text{O}_{7-\delta}$," *Phys. Rev. B* **41**, 1863 (1990)

Oxygen Annealing

- [2.7] P. K. Gallagher, "Characterization of $\text{Ba}_2\text{YCu}_3\text{O}_x$ as a function of oxygen partial pressure I. thermoanalytical measurements," *Adv. Cer. Mater.* **2**, 632 (1987)
- [2.8] B. W. Veal, H. You, A. P. Paulikas, H. Shi, Y. Fang, and J. W. Downey, "Time-dependent superconducting behavior of oxygen-deficient $\text{YBa}_2\text{Cu}_3\text{O}_x$: possible annealing of oxygen vacancies at 300 K," *Phys. Rev. B* **42**, 4770 (1990); B. W. Veal, A. P. Paulikas, H. You, H. Shi, Y. Fang, and J. D. Downey, "Observation of temperature-dependent site disorder in $\text{YBa}_2\text{Cu}_3\text{O}_{7-\delta}$ below 150 °C," *Phys. Rev. B* **42**, 6305 (1990)

- [2.9] E. Osquiguil, M. Maenhoudt, B. Wuyts, and Y. Bruynseraede, "Controlled preparation of oxygen deficient $\text{YBa}_2\text{Cu}_3\text{O}_x$ films," *Appl. Phys. Lett.* **60**, 1627 (1992)
- [2.10] P. Meuffels, B. Rupp, and E. Pörschke, "Physical and structural properties of $\text{YBa}_2\text{Cu}_3\text{O}_x$ prepared by a defined oxygen sorption technique," *Physica C* **156**, 441 (1988)
- [2.11] D. Shi and D. W. Capone, "60-90 K superconducting phase transition in $\text{YBa}_2\text{Cu}_3\text{O}_{7-\delta}$," *Appl. Phys. Lett.* **53**, 159 (1988)
- [2.12] E. Takayama-Muromachi, Y. Uchida, M. Ishii, T. Tanaka, and K. Kato, "High T_c superconductor $\text{YBa}_2\text{Cu}_3\text{O}_y$ -oxygen content vs T_c relation-," *Jpn. J. Appl. Phys.* **26**, L1156 (1987)

Variable-range Hopping

- [2.13] N. F. Mott, "Conduction in non-crystalline materials III. localized states in a pseudogap and near extremities of conduction and valence bands," *Phil. Mag.* **19**, 835 (1969); "Conduction in glasses containing transition metal ions," *J. Non Cryst. Solid* **1**, 1 (1968)

Band Structure

- [2.14] R. C. Dynes, "The order parameter of high T_c superconductors: experimental probes," *Solid State Commun.* **92**, 53 (1994)
- [2.15] N. Nücker, H. Romberg, X. X. Xi, F. Fink, B. Gegenheimer, and Z. X. Zhao, "Symmetry of holes in high- T_c superconductors," *Phys. Rev. B* **39**, 6619 (1989)
- [2.16] See W. E. Pickett, "Electronic structure of the high-temperature oxide superconductors," *Rev. Mod. Phys.* **61**, 433 (1989) and references there after.
- [2.17] S. Massidda, J. Yu, A. J. Freeman, and D. D. Koelling, "Electronic structure and properties of $\text{YBa}_2\text{Cu}_3\text{O}_{7-\delta}$, a low dimensional, low density of states superconductor," *Phys. Lett. A* **122**, 198 (1987)
- [2.18] J. Yu, S. Massidda, A. J. Freeman, and D. D. Koelling, "Bonds, bands, charge transfer excitations and superconductivity of $\text{YBa}_2\text{Cu}_3\text{O}_{7-\delta}$," *Phys. Lett. A* **122**, 203 (1987)
- [2.19] L. F. Mattheiss and D. R. Hamann, "Electronic structures of high T_c superconducting $\text{Ba}_2\text{YCu}_3\text{O}_{6.9}$," *Solid State Commun.* **63**, 395 (1987)

Hubbard Models

- [2.20] P. W. Anderson, "The resonating valence bond state in La_2CuO_4 and superconductivity," *Science* **235**, 96 (1987)

- [2.21] V. J. Emery, "Theory of high- T_c superconductivity in oxides," *Phys. Rev. Lett.* **58**, 2794 (1987)
- [2.22] S. Uchida, T. Ido, H. Takagi, T. Arima, Y. Tokura, and S. Tajima, "Optical spectra of $\text{La}_{2-x}\text{Sr}_x\text{CuO}_4$: effect of carrier doping on the electronic structure of the CuO_2 plane," *Phys. Rev. B* **43**, 7942 (1991)
- [2.23] C. A. Balseiro, M. Avignon, A. G. Rojo, and B. Alascio, "Electronic Properties of High- T_c superconductors," *Phys. Rev. Lett.* **62**, 2624 (1989)

Optical Reflectance

- [2.24] S. L. Cooper, D. Reznik, A. Kotz, M. A. Karlow, R. Liu, M. V. Klein, W. C. Lee, J. Giapintzakis, and D. M. Ginsberg, "Optical studies of the a -, b -, and c -axis charge dynamics in $\text{YBa}_2\text{Cu}_3\text{O}_{6+x}$," *Phys. Rev. B* **47**, 8233 (1993)

Raman Scattering

- [2.25] K. B. Lyons, P. A. Fleury, L. F. Schneemeyer, and J. V. Waszczak, "Spin fluctuations and superconductivity in $\text{Ba}_2\text{YCu}_3\text{O}_{6+\delta}$," *Phys. Rev. Lett.* **60**, 732 (1988)
- [2.26] A. A. Maksimov, I. I. Tartakovskii, M. V. Klein, and B. W. Veal, "Two-magnon light scattering in $\text{YBa}_2\text{Cu}_3\text{O}_{6+x}$ single crystals near the metal-insulator transition," *Phys. Rev. B* **49**, 15385 (1994)
- [2.27] C. Thomsen, E. Schönherr, B. Friedl, and M. Cardona, "Identification of the 1250-cm^{-1} Raman feature in $\text{YBa}_2\text{Cu}_3\text{O}_6$," *Phys. Rev. B* **42**, 943 (1990)
- [2.28] M. Yoshida, S. Tajima, N. Koshizuka, S. Tanaka, S. Uchida, and T. Itoh, "Two-magnon and two-phonon excitations in some parent insulating compounds of high- T_c cuprates," *Phys. Rev. B*, **46**, 6505 (1992)
- [2.29] M. V. Klein, R. Liu, D. Salamon, S. L. Cooper, W. C. Lee, D. M. Gindberg, and S. W. Cheong, "New features of Mott-Hubbard insulator gap of parent HTS compounds found by resonance Raman scattering and UV-excited ordinary Raman scattering," *J. Supercond.* **7**, 429 (1994)
- [2.30] E. T. Heyen, J. Kircher, and M. Cardona, "Resonant Raman scattering in insulating $\text{YBa}_2\text{Cu}_3\text{O}_6$ as a probe of its electronic structure," *Phys. Rev. B* **45**, 3037 (1992)
- [2.31] R. Liu, D. Salamon, M. V. Klein, S. L. Cooper, W. C. Lee, S-W. Cheong, and D. M. Ginsberg, "Novel Raman-active electronic excitations near the charge-transfer gap in insulating cuprates," *Phys. Rev. Lett.* **71**, 3709 (1993)

Photoluminescence

- [2.32] V. N. Denisov, C. Taliani, A. G. Mal'shukov, V. M. Burlakov, E. Schönherr, and G. Ruani, "Infrared-excited Raman scattering and photoluminescence of

deep intragap states in semiconducting $\text{YBa}_2\text{Cu}_3\text{O}_{6+x}$,” *Phys. Rev. B* **48**, 16714 (1993)

Photoconductivity

- [2.33] G. Yu, C. H. Lee, D. Mihailovic, A. J. Heeger, C. Fincher, N. Herron, and E. M. McCarron, “Photoconductivity in insulating $\text{YBa}_2\text{Cu}_3\text{O}_{6+x}$: from Mott-Hubbard insulator to Fermi glass via oxygen doping,” *Phys. Rev. B* **48**, 7545 (1993)
- [2.34] G. Yu, A. J. Heeger, G. Stucky, N. Herron, and E. M. McCarron, L. Cong, G. C. Spalding, C. A. Nordman, and A. M. Goldman, “Phase separation of photogenerated carriers and photoinduced superconductivity in high- T_c materials,” *Phys. Rev. B* **45**, 4964 (1992)

Photodoping and Persistent Photoconductivity

- [2.3] G. Nieva, *et al. ibid.*
- [2.4] E. Osquiguil, *et al. ibid.*
- [2.35] V. I. Kudinov, I. L. Chaplygin, A. I. Kirilyuk, N. M. Kreines, R. Laiho, E. Lähderanta, and C. Ayache, “Persistent photoconductivity in $\text{YBa}_2\text{Cu}_3\text{O}_{6+x}$ films as a method of photodoping toward metallic and superconducting phases,” *Phys. Rev. B* **47**, 9017 (1993)
- [2.36] S. L. Bud’ko, H. H. Feng, M. F. Davis, J. C. Wolfe, and P. H. Hor, “Persistent photoconductivity in insulating and superconducting $\text{YBa}_2\text{Cu}_3\text{O}_x$ thin films: temperature and spectral dependence,” *Phys. Rev. B* **48**, 16707 (1993)
- [2.37] K. Tanabe, S. Kubo, F. H. Teherani, H. Asano, and M. Suzuki, “Effects of photoinduced hole doping on normal-state and superconducting transport in oxygen-deficient $\text{YBa}_2\text{Cu}_3\text{O}_y$,” *Phys. Rev. Lett.* **72**, 1537 (1994)
- [2.38] J. Hasen, D. Lederman, I. Schuller, V. Kudinov, M. Maenhoudt, and Y. Bruynseraede, “Enhancement of persistent photoconductivity in insulating high- T_c thin films,” *Phys. Rev. B* **51**, 1342 (1995)
- [2.39] G. Yu, A. J. Heeger, G. Stucky, N. Herron, and E. M. McCarron, “Transient photoinduced conductivity in semiconducting single crystals of $\text{YBa}_2\text{Cu}_3\text{O}_{6.3}$: search for photoinduced metallic state and for photoinduced superconductivity,” *Solid State Commun.* **72**, 345 (1989)

3 Fabrication of YBCO Thin Films with Different Oxygen Contents

3.1 Overview of different deposition methods

Deposition of HTS thin films using all major physical vapor deposition (PVD) and chemical vapor deposition (CVD) techniques has been widely studied [3.1-3.28]. Depending on whether post annealing after the film growth is necessary or not, the deposition techniques are divided into *in-situ* and *ex-situ* methods. For multi-source processes such as vacuum evaporation [3.4, 3.5] and metal-organic chemical vapor deposition (MOCVD) [3.6-3.11], subsequent high-temperature annealing is mandatory and more important than the deposition process itself. *Ex-situ* methods have been used to produce nearly all known HTS thin films. Moreover, thin films of Bi-Sr-Ca-Cu-O and Tl-Ba-Ca-Cu-O families are found to be readily possible to fabricate only by *ex-situ* techniques.

The main advantage of the *in-situ* growth is that no post annealing is needed to rearrange the lattice structure of as-deposited films. The *in-situ* process produces thin films with minimum contamination and with a single-crystal structure on epitaxial substrates. Hence, *in situ* deposition results in films of the highest quality. Laser ablation [3.12-3.18] and sputtering [3.19-3.28] are the most often used *in-situ* PVD techniques. For both methods, substrates must be heated to temperatures above the crystallization point of the deposited material. Figure 3.1 plots schematic configurations for pulsed laser deposition (PLD) and off-axis sputtering.

In PLD, short-pulse excimer (KrF_2) laser beam is focused on a ceramic YBCO target to generate a plume of evaporated atoms [3.12-3.18]. With a proper power density ($\sim 1 \text{ J/cm}^2$), the composition of the target can be accurately reproduced on the substrate. Short-pulse and short-wavelength laser is preferred to reduce the overheating of the target. Laser power is found to be crucial in depositing smooth films without particulate formation during the process [3.18]. PLD has the advantage of depositing thin films at a much faster rate than off-axis sputtering. The size of the PLD grown films, however, is limited by the evaporant plume diameter and is usually up to 1 cm^2 .

By contrast, sputtering is capable of depositing YBCO thin films with large areas (*e.g.* 2-inch wafers). Sputtering has been the standard technique in deposition of conventional superconductor thin films, magnetic media, and metal interconnects in VLSI technology. In YBCO thin-film deposition, single-target magnetron sputtering

has proven to be a simple and reliable process. Both *dc* and *rf* sputtering methods have been used to deposit high quality YBCO films.

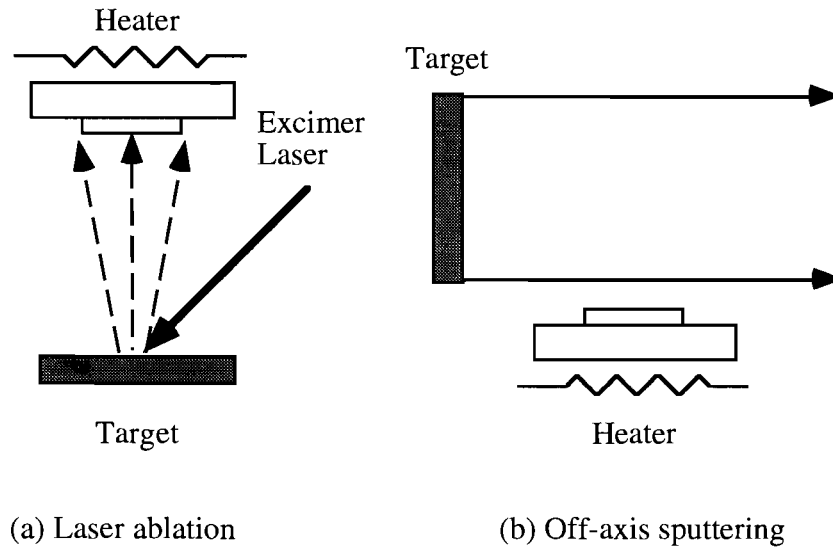


Fig. 3.1 Schematics configurations for (a) PLD, and (b) off-axis sputtering methods.

Low deposition rate of sputtering arises from the difficulty in obtaining the stoichiometry of deposited films exactly the same as that of the target. Due to preferential backsputtering by negative oxygen ions, stoichiometry of the sputtered YBCO films may be different from the target composition [3.23]. Such a deviation in composition causes a significant degradation in the superconducting properties of YBCO films.

In principle, it is always possible to offset the effects of preferential backsputtering by modifying the target composition, but this approach leads to a complicated stoichiometry dependence on sputtering parameters. Hence, modifying target composition is not a practical method for reliable deposition of YBCO films. Instead, other approaches, such as the increase of the sputtering pressure or special target-substrate configurations, have proven to be much easier to implement.

High pressure sputtering is preferred to reduce the backsputtering. The efficient scattering of energetic particles by the sputtering gas greatly lowers the bombardment energy. In a parallel target-substrate orientation, high quality YBCO

films with $T_c=90$ K were obtained by high pressure sputtering [3.25]. However, the drawbacks of the high-pressure sputtering include a very low deposition rate and potentially unstable plasma (arcing). Moreover, high-pressure sputtering causes a heavy load for vacuum pumps, e.g., requiring frequent regeneration of cryopumps.

Alternatively, special target-substrate configurations such as off-axis sputtering and negative-ion shields were designed to minimize the impact of preferential backsputtering. In the off-axis configuration, a substrate is placed outside the region of sputtering plasma [see Fig. 3.1(b)]. Direct bombardment of energetic particles is avoided at the expense of the deposition rate. Despite its extremely low deposition rate, off-axis sputtering has been used to deposit YBCO films with the highest T_c 's and J_c 's.

In addition to the off-axis sputtering, a configuration using a negative-ion shield has also proven to be a reliable method of depositing YBCO with excellent properties [3.26]. In this case, a negative-ion shield is placed above the target center to reduce the bombardment and the substrate is placed inside the magnetron erosion ring. Due to its parallel target-substrate orientation, this approach has a deposition rate much higher than the off-axis sputtering.

Correct gas ratio between argon and oxygen is also an important parameter to obtain high quality YBCO films [3.25]. Sputtering in pure oxygen is capable of depositing high quality films. However, it leads to slightly Y-rich composition on the surface of the target. On the other hand, pure argon sputtering results in very Y-rich films which are not superconducting and require *ex-situ* annealing. The degraded target due to long-time sputtering in pure argon could be fully recovered once the sputtering gas is switched to pure oxygen. For mixed sputtering gases, the argon to oxygen ration below 10:1 is recommended in order to obtain YBCO films with the high T_c 's and J_c 's.

Crystal structure of the target also influences the quality of sputtered YBCO films. Thin films deposited using tetragonal (nonsuperconducting) targets display a degraded T_c [3.25]. In contrast, orthorhombic targets lead to films with excellent superconducting properties. The contrast is related to the difference in the embedded active oxygen atoms in tetragonal and orthorhombic targets. During the deposition, the stabilization of the orthorhombic phase is very sensitive to the amount of oxygen available. Insufficient oxygenation leads to films with degraded T_c 's. Moreover, it is well known that active oxygen atoms are much more efficient than molecular oxygen in forming the orthorhombic phase [3.4, 3.5, 3.30]. One of the sources for active oxygen atoms is the target itself. For the orthorhombic target, the embedded active

oxygen is adequate to assist the orthorhombic formation on the substrate. For the tetragonal target, however, much less active oxygen is available. Oxidation has to rely on oxygen from the sputtering gas. As a result, degraded YBCO films with a less orthorhombic structure are obtained.

Substrates selection is another key issue for high-quality HTS films growth. General requirements for the substrates include good mechanical property, low cost and chemical stability. In addition, epitaxial growth demands good lattice and thermal expansion match between the substrate and thin film. Commonly used substrates for YBCO deposition are MgO, LaAlO₃, and SrTiO₃. Among them, SrTiO₃ and LaAlO₃ provide YBCO films with the best T_c 's, J_c 's, and sharp superconducting transition widths. Unfortunately, a large dielectric constant ($\epsilon \sim 300$) of SrTiO₃ is inappropriate for high-frequency applications. On the other hand, MgO has a much smaller dielectric constant ($\epsilon \sim 10$) and is suitable for high-frequency applications. Further, MgO is much cheaper than SrTiO₃ or LaAlO₃. In terms of thermal conductivity, MgO is also a better thermal conductor than LaAlO₃ and SrTiO₃. On the other hand, LaAlO₃ substrates provide a better epitaxial conditions than MgO and enable deposition of very high quality films. At the same time, the dielectric constant of LaAlO₃ is comparable with that of MgO. Table 3.1 lists properties of commercially available SrTiO₃, LaAlO₃, and MgO substrates [3.46]

Table 3.1 Physical Properties of Single-Crystal Substrates for HTS [3.46]

Substrate	YBCO Lattice Mismatch	Dielectric Constant	Loss $\tan\delta$
SrTiO ₃	1.2%	310 (300 GHz)	3×10^{-2} (300 GHz)
LaAlO ₃	1.8%	20 (700 GHz)	8×10^{-3} (700 GHz)
MgO	9.0%	9.9 (300 GHz)	1×10^{-3} (300 GHz)

Preheating of the substrate above the crystallization temperature of YBCO (600-900 °C) is essential to growth high quality thin films using PVD. High substrate temperature is necessary to produce c-axis oriented films [3.29-3.31]. At temperatures lower than 650 °C, formation of a degraded phase with a-axis

orientation takes place. Furthermore, high temperature is preferred for sufficient oxygenation [3.32].

3.2 Thin-film characterization

Proper stoichiometry of YBCO films is crucial for attaining good superconducting properties. It can be determined using the non-destructive energy dispersive x-ray analysis (EDX). With proper calibration, EDX is capable of detecting the composition with high accuracy. For oxygen diffusion studies, secondary ion mass spectroscopy (SIMS) is used to trace tiny variations in oxygen stoichiometry.

X-ray diffraction (XRD) is the most common technique for determining the film crystalline structure. It provides information about the preferred orientation and lattice constants normal to the film surface. Also, the uniformity of c-axis orientation is reflected in the sharpness of the 2θ peak.

Transmission electron microscopy (TEM) is another powerful tool in defining the crystallographic relations. The diffraction patterns of TEM contain enriched information about the crystal orientation, phase, defects, and grain boundaries, which play an important role in the fabrication of HTS Josephson junctions. Furthermore, the high magnification of TEM also permits detection of submicron features which are invisible by other techniques.

In YBCO thin films, the most common defects revealed by TEM are dislocations and twinning at the film/substrate interface which originate from mismatch between YBCO and the substrate [3.25]. Such defects are intrinsic to all kinds of epitaxial growth and hence directly indicate the imperfection of epitaxy. The second major source of defects are the second-phase particles with structures other than “123”. TEM is capable of resolving these particles even in the case when they are too sparse to be detected by EDX. Formation of second-phase structures is also responsible for the stacking fault observed in the cross-section TEM images of c-axis oriented films.

For investigating surface morphology of films, scanning electron microscopy (SEM) is widely used. Advanced SEM has even the ability of performing cryogenic testing at the liquid nitrogen temperature (77 K).

3.3 RF magnetron sputtering YBCO thin films

YBCO thin films studied in this thesis were fabricated by *in-situ* RF magnetron sputtering [3.25]. The best YBCO thin films were deposited on LaAlO₃ substrates using off-axis configuration (deposited by Dr. J. Gavalier at the Westinghouse Science and Technology Center). These films displayed an extremely sharp, about 0.5-K wide (10-90%) superconducting transition width, high zero-resistance critical temperature T_{c0} of 89.5 K and J_c above 2 MA/cm² at 77 K. We have also performed in-house sputtering of YBCO thin films on polished LaAlO₃, SrTiO₃ and MgO substrates, using CVC's SC8000 RF magnetron sputtering system. These films exhibited T_{c0} 's between 84 K and 89 K with ΔT_c of 1-2 K. The thickness of our YBCO films ranged from 80 to 300 nm. A composite YBCO target was used for *rf* sputtering. Substrates were preheated to approximately 750 °C and stabilized prior to deposition. The sputtering gas consisted of 10 mTorr of Ar and 5 mTorr of O₂. A negative-ion shield of 3 inches in diameter was placed above the target to reduce the back etching of our films. The spacing between the target and the substrate was 1-3/4 inches. The *rf* power output was 450 W and zero reflection was achieved by automatic impedance matching. Presputtering was applied to minimize possible contamination from the target surface. The deposition rate was about 35 Å/min.

Either 90-K or semiconducting YBCO films were deposited by the above method. For fully oxygenated (90-K) samples, as-deposited films were *in situ* annealed in 100 mTorr of O₂. Conversely, fully oxygen-depleted (semiconducting) films were obtained by *in-situ* annealing in 100 mTorr of Ar. Oxygen-depleted YBCO/MgO samples were prepared by for femtosecond pump-probe investigations.

3.4 Annealing of YBCO thin films

Besides the *in-situ* annealing following the deposition, YBCO thin films can be *ex-situ* annealed to achieve various oxygen contents. Various annealing methods have been reported for preparing YBCO samples with the desired oxygen content [3.33-3.38]. For annealing in oxygen atmosphere, the oxygen pressure-temperature phase diagrams were obtained [3.33-3.35]. These phase diagrams have been used as a guide for dependable control of the oxygen content inside YBCO. Other annealing methods include controlled oxidation of insulating YBCO at high temperatures

[3.36], constant-temperature annealing in controlled time [3.37], and quenching from high temperature into liquid nitrogen [3.38].

The oxygen stoichiometry of our samples was modified either by furnace annealing or by radiative heating in vacuum. Specifically, oxygen-depleted samples for laser writing were prepared by deoxygenating the superconducting films inside a vacuum chamber. The YBCO-on-LaAlO₃ films were heated to 650 °C in 15 mTorr Ar. Partially oxygen-deficient samples for femtosecond pump-probe experiments were also vacuum annealed. The heating temperatures were 400, 365, and 340 °C for YBCO/LaAlO₃ samples with T_c of 30 K, 55 K, and 60 K, respectively. Constant dwell time of 1 hour was maintained during the annealing process.

Furnace annealing was also applied to decrease or recover the oxygen content in YBCO films. Although furnace annealing is less clean (often results in surface contamination) than the vacuum process, it is much more convenient to operate. Continuous flow of ultra pure Ar or O₂ gas was guided through the oven for removing or restoring oxygen, respectively.

3.5 Electrical measurements

The resistivity and critical current density versus temperature, $R(T)$ and $J_c(T)$, curves were measured in a standard four-probe geometry. To ensure good ohmic contacts, silver contact pads of 300-nm thick were vacuum evaporated directly on top of our test structures. Aluminum wires were wire bonded to electrically connect the contact pads with corresponding leads in the testing probe. The samples were placed on a cold finger inside the probe, which was cooled down by liquid nitrogen or liquid helium. The temperature and the cooling process were computer monitored by a Lakeshore[®] temperature controller. Data acquisition was achieved by using customized Labview[®] programs.

Electrical transport of YBCO thin films with various oxygen contents was tested. The $R(T)$ curves for superconducting samples with T_c 's of 89.5 K, 60 K, 55 K, 30 K and a semiconducting film are shown in Fig. 3.2. To assure enough T_c aging of the intermediately doped YBCO, cryogenic testing was performed at least 1 day after the annealing. Thus, further shift in T_c was considered negligible.

The grain boundary characteristics can be reflected by the slope of the normal state $R(T)$ curves. While films with T_c 's above 55 K exhibit nearly zero resistance at zero temperature (extrapolation), the 30-K film shows a large positive zero-

temperature resistance intercept. It is well known that the positive zero-temperature resistance offset originates from high-angle grain boundaries in the film [3.39]. Therefore, the nearly zero offset for samples with T_c above 55 K indicates well aligned grain boundaries in these films. As opposite to that, the big zero-resistance offset in the 30-K sample implies the large content of high-angle grain boundaries.

Moreover, the sharp transitions for samples with $T_c \geq 55$ K suggest that oxygen was distributed relatively homogeneously in these films [3.35]. By contrast, the broad transition in 30-K sample indicates an inhomogeneous oxygen distribution. Hence, the 30-K sample is considered a mixture of the semiconducting and the superconducting phases. A significant rounding of the transition for the 30-K sample is probably related to increased two-dimensional fluctuations [3.40-3.41].

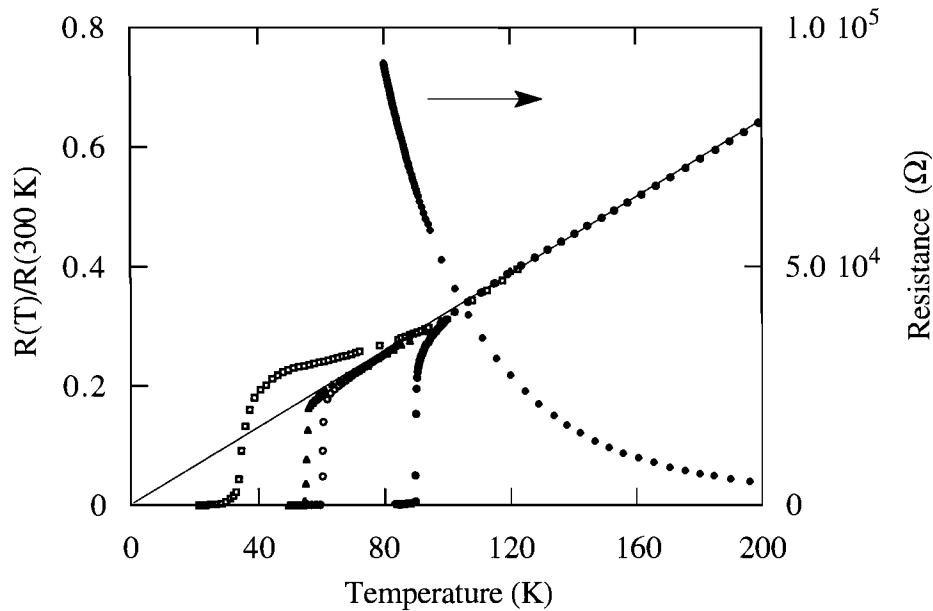


Fig. 3.2 Resistivity vs. temperature for sputtered YBCO films with various oxygen doping levels.

The magnitude of the temperature-dependent resistance, on the other hand, indicates the defect density in the grains. Despite potential difference in the contact resistance, a significant increase in the 300-K resistance from the 90-K to 30-K was observed. This fact indicates an increasing defect density towards the M-I transition and is consistent with the expectation that perfect crystal structures correspond to

either oxygen-poor or fully oxygenated films. Maximum lattice distortion is expected near the M-I phase transition.

As shown in Fig. 3.2, the resistance of a semiconducting sample increased strongly at low temperatures and exceeded $10 \text{ M}\Omega/\text{square}$ below 100 K . The temperature dependence of semiconducting YBCO cannot be fitted by a simple exponential law that corresponds to thermal activation of localized states. Instead, it follows Mott's VRH [3.42]. Figure 3.3 replots the resistance data from the semiconducting sample in Fig. 3.2 and fits to the formalism of VRH. For the defect states inside the bandgap, conducting current could be formed either by multiple trapping or by electron tunneling between the localized states in the same direction (hopping). The tunneling rate is a sensitive function of the intersite distance and the energy separation between these states. A schematic diagram of trapping and hopping is plotted in Fig. 3.4. As indicated in Chapter 2, the *dc* conductivity σ for Mott's VRH is proportional to $T^{-1/(N+1)}$, where N is the number of dimensions involved in the hopping process.

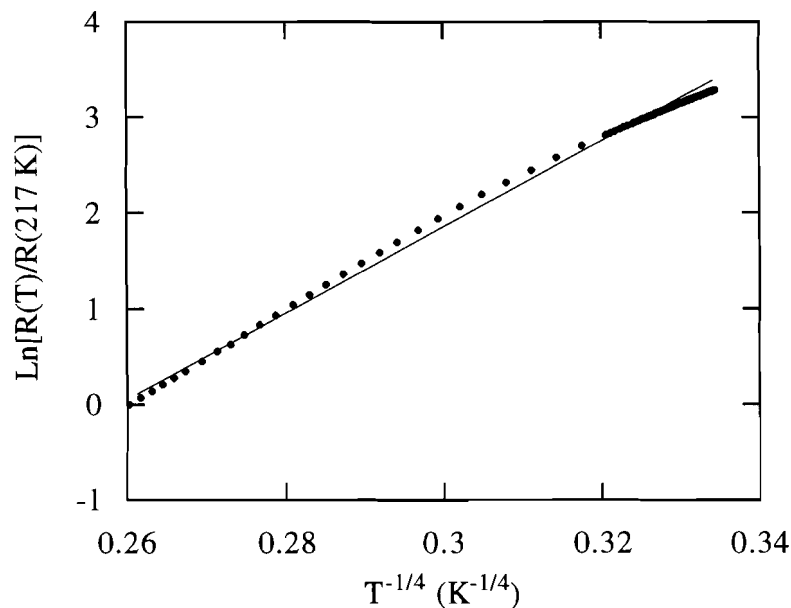


Fig. 3.3 $\text{Ln}[R(T)/R(217 \text{ K})]$ vs. $T^{-1/4}$ for the semiconducting sample shown in Fig. 3.2. The linear fit shows a variable-range hopping.

Evidently, the resistance of our semiconducting sample in Fig. 3.3 follows closely to the $T^{-1/4}$ behavior. As a result, the low-temperature transport of semiconducting YBCO can be concluded as a 3-dimensional VRH.

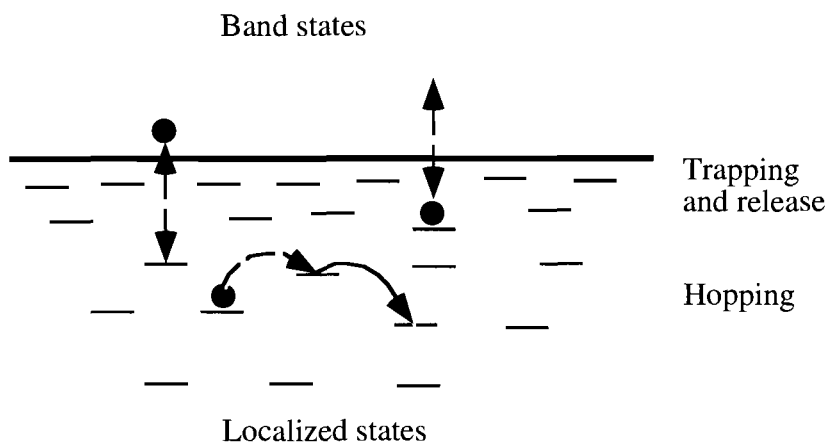


Fig. 3.4 Schematic diagram of transport with trapping and hopping [3.43].

3.6 Microfabrication

Photolithography and lift-off procedures were applied for patterning of our YBCO microstructures. These patterns include YBCO microbridges designed for critical-current measurements and ultrafast optoelectrical response tests on a double-bridge configuration [3.44]. Microstrip lines and coplanar waveguides [3.45] were also lifted off for testing of the photoconductive performance of YBCO thin films. Figure 5.5 shows a typical flow chart of our lift-off procedure.

3.7 Summary

RF magnetron sputtering has been used for depositing our high quality YBCO thin films. Sputtering configuration and parameters are crucial to the deposition process. Off-axis and negative-ion shield configurations are the two approaches that can efficiently eliminate the preferential backsputtering of freshly deposited thin films. Both semiconducting and superconducting (with high T_c and sharp superconducting transitions) YBCO thin films have been deposited by *in-situ* RF

magnetron sputtering. YBCO films with different oxygen contents have been successfully prepared by either vacuum or furnace annealing methods. The electrical properties of YBCO thin films were measured by cryogenic testing.

Wet etch and photo lift-off procedures were also used to pattern microbridges and coplanar transmission lines on YBCO films.

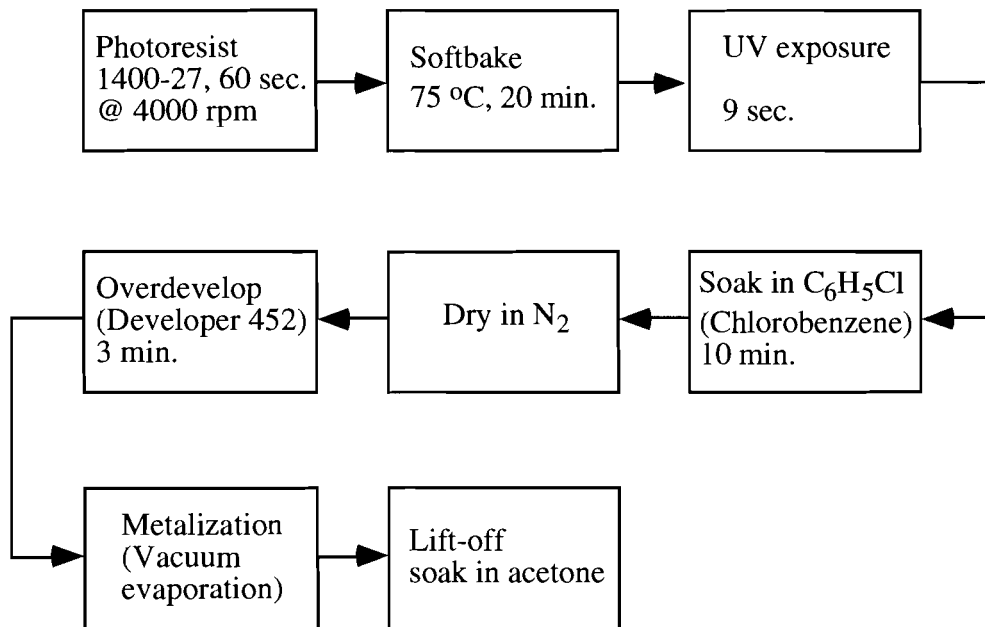


Fig. 3.5 Flow chart of our lift-off procedure for patterning of YBCO circuits.

References

Fabrication Review

- [3.1] R. G. Humphreys, J. S. Satchell, N. G. Chew, J. A. Edwards, S. W. Goodyear, S. E. Blenkinsop, O. D. Dosser, and A. G. Cullis, "Physical vapour deposition techniques for the growth of $\text{YBa}_2\text{Cu}_3\text{O}_7$ thin films," *Supercond. Sci. Technol.* **3**, 38 (1990)
- [3.2] R. Simon, "High- T_c thin films and electronic devices," *Phys. Today*, **June** p. 64, 1991
- [3.3] X. X. Xi, T. Venkatesan, Q. Li, X. D. Wu, A. Inam, C. C. Chang, R. Ramesh, D. M. Hwang, T. S. Ravi, A. Findikoglu, D. Hemmick, S. Etemad, J. A. Martinez, and B. Wilkens, "Preparation of thin film high temperature superconductors," *IEEE Trans. Magn.* **MAG-27**, 9982 (1991)

Vapor Evaporation

- [3.4] N. Missert, R. Hammond, J. E. Mooj, V. Matijasevic, P. Rosenthal, T. H. Geballe, A. Kapitulnik, M. R. Beasley, S. S. Laderman, C. Liu, E. Garwin, and R. Barton, "*In situ* growth of superconducting YBaCuO using reactive electron-beam coevaporation," *IEEE Trans. Magn.* **MAG-25**, 2418 (1989)
- [3.5] T. Terashima, Y. Bando, K. Iijima, K. Yamamoto, and K. Hirata, "Epitaxial growth of $\text{YBa}_2\text{Cu}_3\text{O}_{7-x}$ thin films on (110) SrTiO_3 single crystals by activated evaporation," *Appl. Phys. Lett.* **53**, 2232 (1988)

MOCVD

- [3.6] K. Zhang, B. S. Kwak, E. P. Boyd, A. C. Wright, and A. Erbil, "*c*-axis oriented $\text{YBa}_2\text{Cu}_3\text{O}_{7-x}$ superconducting films by metalorganic chemical vapor deposition," *Appl. Phys. Lett.* **54**, 380 (1989)
- [3.7] D. S. Richeson, B. W. Wessels, J. Zhao, J. M. Zhang, H. O. Marcy, T. J. Marks, L. M. Tonge, and C. R. Kannewurf, "Organometallic chemical vapor deposition routes to high T_c superconducting Tl-Ba-Ca-Cu-O films," *Appl. Phys. Lett.* **54**, 2154 (1989)
- [3.8] K. Zhang, E. P. Boyd, B. S. Kwak, A. C. Wright, and A. Erbil, "Metalorganic chemical vapor deposition of $\text{Tl}_2\text{CaBa}_2\text{Cu}_2\text{O}_y$ superconducting thin films on sapphire," *Appl. Phys. Lett.* **55**, 1258 (1989)
- [3.9] G. Malandrino, D. S. Richeson, T. J. Marks, D. C. DeGroot, J. L. Schindler, and C. R. Kannewurf, "Phase-selective route to high T_c superconducting

Tl₂Ba₂Ca_{n-1}Cu_nO_{2n+4} films: combined metalorganic chemical vapor deposition using an improved barium precursor and stoichiometry-controlled thallium vapor diffusion,” *Appl. Phys. Lett.* **58**, 182 (1991)

- [3.10] K. H. Young, M. Robinson, G. V. Negrete, J. Zhao, C. S. Chern, Y. Q. Li, and P. E. Norris, “Microwave resonators from YBa₂Cu₃O_{7-δ} thin films made by plasma-enhanced metalorganic chemical vapor deposition,” *Appl. Phys. Lett.* **61**, 543 (1992)
- [3.11] Z. Lu, J. K. Truman, M. E. Johansson, D. Zhang, C. F. Shih, G. C. Liang, “Large area double-sided YBa₂Cu₃O_{7-δ} films grown by single-source metalorganic chemical vapor deposition,” *Appl. Phys. Lett.* **67**, 712 (1995)

Pulsed Laser Ablation

- [3.12] X. D. Wu, A. Inam, T. Venkatesan, C. C. Chang, E. W. Chase, P. Barboux, J. M. Tarascon, and B. Wilkens, “Low-temperature preparation of high T_c superconducting thin films,” *Appl. Phys. Lett.* **52**, 754 (1988)
- [3.13] A. Inam, M. S. Hegde, X. D. Wu, T. Venkatesan, P. England, P. F. Miceli, E. W. Chase, C. C. Chang, J. M. Tarascon, J. B. Wachtman, “As-deposited high T_c and J_c superconducting thin film made at low temperatures,” *Appl. Phys. Lett.* **53**, 908 (1988)
- [3.14] Z. P. Zheng, Q. Y. Ying, S. Witanachchi, Z. Q. Huang, D. T. Shaw, and H. S. Kwok, “Role of the oxygen atomic beam in low-temperature growth of superconducting films by laser deposition,” *Appl. Phys. Lett.* **54**, 954 (1989)
- [3.15] G. Koren, A. Gupta, and R. J. Baseman, “Role of atomic oxygen in the low-temperature growth of YBa₂Cu₃O_{7-δ} thin films by laser ablation,” *Appl. Phys. Lett.* **54**, 1920 (1989)
- [3.16] F. Fuso, L. N. Vyacheslavov, G. Masciarelli, E. Arimondo, “Stark broadening diagnostics of the electron density in the laser ablation plume of YBa₂Cu₃O_{7-δ} and PbZr_xTi_{1-x}O₃,” *J. Appl. Phys.* **76**, 8088 (1994)
- [3.17] S. Proyer, E. Stangl, P. Schwab, D. Bäuerle, P. Simon, and C. Jordan, “Patterning of YBCO films by excimer-laser ablation,” *Appl. Phys. A* **58**, 471 (1994)
- [3.18] Y. Watanabe, M. Tanamura, S. Matsumoto, and Y. Seki, “Laser power dependence of particulate formation on pulse laser deposited films,” *J. Appl. Phys.* **78**, 2029 (1995)

Sputtering

- [3.19] H. C. Li, G. Linker, F. Ratzel, R. Smithey, and J. Geerk, “*Appl. Phys. Lett.* **52**, 1098 (1988)

- [3.20] R. L. Sandstrom, W. J. Gallagher, T. R. Dinger, R. H. Koch, R. B. Laibowitz, A. W. Kleinsasser, R. J. Gambino, B. Bumble, and M. F. Chisholm, *Appl. Phys. Lett.* **53**, 444 (1988)
- [3.21] U. Poppe, J. Schubert, R. R. Arons, W. Evers, C. H. Freiburg, W. Reichert, K. Schmidt, W. Sybertz, and K. Urban, *Solid State Commun.* **66**, 661 (1988)
- [3.22] N. Terada, H. Ihara, M. Jo, M. Hirabayashi, Y. Kimura, K. Matsutani, K. Hirata, E. Ohno, R. Sugise, and F. Kawashima, *Jpn. J. Appl. Phys.* **27**, L639 (1988)
- [3.23] S. M. Rossnagel and J. J. Cuomo, in *Thin Film Processing and Characterization of high-Temperature Superconductors*, edited by J. M. E. Harper, R. J. Colton, and L. C. Feldman, (American Institute of Physics, New York 1988), p. 106
- [3.24] C. B. Eom, J. Z. Sun, K. Yamamoto, A. F. Marshall, K. E. Luther, T. H. Geballe, and S. S. Laderman, "In situ grown $\text{YBa}_2\text{Cu}_3\text{O}_{7-d}$ thin films from single-target magnetron sputtering," *Appl. Phys. Lett.* **55**, 595 (1989)
- [3.25] J. R. Gavaler, J. Talvacchio, T. T. Braggins, M. G. Forrester, and J. Gregg, "Critical parameters in the single-target sputtering of $\text{YBa}_2\text{Cu}_3\text{O}_7$," *J. Appl. Phys.*, **70**, 4383 (1991)
- [3.26] P. H. Ballentine, A. M. Kadin, and D. S. Mallory, "In-situ sputtering of YBCO films for microwave applications," *IEEE Trans. Magn.*, **MAG-27**, 997 (1991)
- [3.27] B. F. Cole, G. C. Liang, N. Newman, K. Char, G. Zaharchuk, and J. S. Martens, "Large-area $\text{YBa}_2\text{Cu}_3\text{O}_{7-\delta}$ thin films on sapphire for microwave applications," *Appl. Phys. Lett.* **61**, 1727 (1992)
- [3.28] B. V. Vuchic, K. L. Merkle, K. A. Dean, D. B. Buchholz, R. P. H. Chang, and L. D. Marks, "Sputter-induced grain boundary junctions in $\text{YBa}_2\text{Cu}_3\text{O}_{7-x}$ thin films on MgO," *J. Appl. Phys.* **77**, 2591 (1995)

Oxidation

- [3.29] H. Asano, M. Asahi, and O. Michikami, "Epitaxy and orientation of $\text{Eu}_1\text{Ba}_2\text{Cu}_3\text{O}_{7-y}$ films grown *in situ* by magnetron sputtering," *Jpn. J. Appl. Phys.* **28**, L981 (1989)
- [3.30] J. Kwok, M. Hong, D. J. Trevor, R. M. Fleming, A. E. White, J. P. Mannaerts, R. C. Farrow, A. R. Kortan, and K. T. Short, "In-situ growth of $\text{Y}_1\text{Ba}_2\text{Cu}_3\text{O}_{7-x}$ films by molecular beam epitaxy with an activated oxygen source," *Physica C* **162-164**, 623 (1989)

- [3.31] G. Linker, X. X. Xi, O. Meyer, Q. Li, and J. Geerk, "Control of growth direction of epitaxial YBaCuO thin films on SrTiO₃-substrates," *Solid State Commun.* **69**, 249 (1989)
- [3.32] X. X. Xi, H. C. Li, J. Geerk, G. Linker, O. Meyer, B. Obst, F. Ratzel, R. Smithey, and F. Wechesenfelder, "Growth and properties of YBaCu-oxide superconducting thin films prepared by magnetron sputtering," *Physica C* **153-155**, 794 (1989)

Annealing

- [3.33] P. K. Gallagher, "Characterization of Ba₂YCu₃O_x as a function of oxygen partial pressure I. thermoanalytical measurements," *Adv. Cer. Mater.* **2**, 632 (1987)
- [3.34] J. D. Jorgensen, B. W. Veal, A. P. Paulikas, L. J. Nowicki, G. W. Crabtree, H. Claus, and W. K. Kwok, *Phys. Rev. B* **41**, 1863 (1990)
- [3.35] E. Osquiguil, M. Maenhoudt, B. Wuyts, and Y. Bruynseraede, *Appl. Phys. Lett.* **60**, 1627 (1992)
- [3.36] P. Meuffels, B. Rupp, and E. Pörschke, "Physical and structural properties of YBa₂Cu₃O_x prepared by a defined oxygen sorption technique," *Physica C* **156**, 441 (1988)
- [3.37] D. Shi and D. W. Capone, "60-90 K superconducting phase transition in YBa₂Cu₃O_{7-δ}," *Appl. Phys. Lett.* **53**, 159 (1988)
- [3.38] E. Takayama-Muromachi, Y. Uchida, M. Ishii, T. Tanaka, and K. Kato, "High T_c superconductor YBa₂Cu₃O_y -oxygen content vs T_c relation-," *Jpn. J. Appl. Phys.* **26**, L1156 (1987)

Transport

- [3.39] B. H. Moeckly, D. K. Lathrop, and R. A. Buhrman, "Electromigration study of oxygen disorder and grain-boundary effects in YBa₂Cu₃O_{7-δ} thin films," *Phys. Rev. B* **47**, 400 (1993)
- [3.40] B. Oh, K. Char, A. D. Kent, M. Naito, M. R. Beasley, T. H. Geballe, R. H. Hammond, A. Kapitulnik, and J. M. Graybeal, "Upper critical field, fluctuation conductivity, and dimensionality of YBa₂Cu₃O_{7-x}," *Phys. Rev. B* **37**, 7861 (1988)
- [3.41] W. Bauhofer, W. Biberacher, B. Gegenheimer, W. Joss, R. K. Kremer, H. Mattaush, A. Muller, and A. Simon, "Anisotropic superconducting properties of YBa₂Cu₃O_{7-δ} ($\delta = 0.1$ and 0.4) untwinned single crystals," *Phys. Rev. Lett.* **63**, 2520 (1989)

- [3.42] N. F. Mott, "Conduction in non-crystalline materials III. localized states in a pseudogap and near extremities of conduction and valence bands," *Phil. Mag.* **19**, 835 (1969); "Conduction in glasses containing transition metal ions," *J. Non Cryst. Solid* **1**, 1 (1968)
- [3.43] H. Scher, M. F. Shlesinger, and J. T. Bendler, "Time-scale invariance in transport and relaxation," *Physics Today*, **January**, p.26, 1991

Patterning

- [3.44] R. Sobolewski, L. Shi, T. Gong, W. Xiong, X. Weng, Y. Kostoulas, and P. M. Fauchet, in *High-Temperature Superconducting Detectors: Bolometric and Nonbolometric*, edited by M. Nahum, J. Villegier, SPIE, **2159**, p. 110, 1994.
- [3.45] A. Sotiris, Ph.D. Dissertation, EE Dept., University of Rochester, 1994.

Substrate Properties

- [3.46] R. Sobolewski, P. Gierlowski, W. Kula, S. Zarembinski, S. J. Lewandowski, M. Berkowski, A. Pajaczkowska, B. P. Gorshunov, D. B. Lyudmirsky, and O. I. Sirotinsky, "High-Tc thin films on low microwave loss alkaline-rare-earth-aluminate crystals," *IEEE Trans. Magn.* **MAG-27**, 876 (1991)

4 LASER PROCESSING OF YBCO THIN FILMS

4.1 Introduction

This Chapter presents a laser-writing technique developed by us for patterning high-quality YBCO circuits. We demonstrate that oxygen can be selectively diffused in or out of YBCO by a focused laser beam. We show that laser writing is a reversible process and the patterned structures display a long-term stability. Microwave testing showed a low surface defect level of our laser-written transmission lines.

4.2 Technique

Developing a technique suitable for patterning of HTS thin-film devices and circuits has been an active subject of study in the past few years. Various methods, such as wet and dry chemical etching, ion milling, and laser ablation, have been implemented to fabricate YBCO structures [4.1]. However, these methods are usually costly because of expensive photolithography procedures and vacuum systems. Baking of photoresist causes oxygen effusion and degrades properties of HTS films. Chemical or physical etching processes often result in structures with degraded surfaces and/or edges. These latter effects can reduce the supercurrent carrying abilities and lead to excessive RF losses. Aqueous etching solutions and deionized water lead to undesirable increases in the high-frequency surface resistance and hence degraded performance of HTS components such as phase shifters, delay lines, transmission lines, and resonators [4.2]. Moreover, a very important and still not completely resolved technological issue is planarization of HTS structures.

Recently, a new planar patterning technique using selective laser heating has been proposed for YBCO thin films [4.3-4.10]. The method is based on the strong dependence of electrical and optical properties of YBCO compounds on their oxygen stoichiometry [4.11-4.12].

As described in Chapter 2, in the fully oxygenated state, orthorhombic YBCO is metallic at temperatures above T_c and superconducting below 90 K. On the other hand, oxygen-depleted YBCO has a tetragonal crystalline structure, it is semiconducting at room temperature and virtually insulating below 100 K. Although the oxygen stoichiometry of YBCO is stable at room temperature, it may be easily modified by moderate heating (>300 °C). During annealing, oxygen can diffuse into

oxygen-poor region in the presence of an oxygen atmosphere or diffuse out of the oxygen-rich part in an oxygen-free ambient. In the case of laser writing, modification of the oxygen content can be controlled on a micrometer scale. Only selected regions of the film are heated with a focused laser beam. Therefore, either oxygen-rich lines in an oxygen-depleted background or oxygen-depleted lines in the oxygen-rich surrounding can be produced to form any desired patterns or circuits.

Early studies on laser-induced phase transitions in YBCO have been discussed in Ref. 4.4-4.7. Following the light absorption change in a thin-film YBCO deposited on YSZ substrate, Rothschild *et al.* [4.3, 4.4] first observed a reversible phase transition caused by laser heating in N₂ or O₂ ambients. Krchnavek *et al.* [4.5] also demonstrated a reversible modification between T_c=87 K and T_c=76 K of superconducting thin film YBCO on SrTiO₃. Using a Nd³⁺: YAG pulsed laser, Dye *et al.* [4.6] selectively patterned T_c=92 K lines in T_c=58 K YBCO films deposited on SrTiO₃ or LaAlO₃ substrates. Shen *et al.* [4.7] reported reversible laser patterning of YBCO thin films on MgO substrates. However, no complete phase transition studies and real circuit applications had been achieved in the above works.

After systematic studies, we accomplished laser writing with fully reversible phase transitions and demonstrated that indeed this technique is a practical tool for non-destructive patterning of YBCO films [4.8-4.11].

In semiconductor industry, laser direct writing has been widely used in VLSI fabrication to produce highly localized patterns [4.15-4.17]. According to its functions, laser direct writing can be divided into etching, deposition, and doping processes. Low temperature photochemical and high temperature thermal processes have been involved in the laser direct writing techniques. Due to a sharp spatial gradient in the temperature distribution produced by laser, it is practical to obtain patterns with micrometer or even submicrometer linewidths [4.15]. Because of the strong temperature dependence of many reactions, localization can be achieved with a spatial resolution greater than the laser-beam size. Linewidths of ~0.3 μm have been reported for laser doping [4.15], etching [4.16], and deposition [4.17] of silicon.

Basically, the principle of our laser writing patterning is the same as that of laser doping. For laser doping, there are two qualitatively different regimes of diffusion, depending on whether the rate-limiting kinetics is interface-limited transport of the dopant to the surface or solid-state diffusion of dopant in the bulk solid. In case of faster solid-state diffusion, such as in polycrystalline materials, it is possible to control the dopant density by adjusting the arrival rate of dopant at the

surface. The depth of doping can be controlled independently by adjusting the surface temperature and the duration of heating.

Several distinctive properties of laser writing make it a promising alternative to the existing patterning techniques for YBCO films. First, laser writing is a non-destructive and fully reversible process. Not only does laser writing generate structures free of surface contamination and edge degradation and hence with minimum loss, but it is also powerful in circuit restructuring and fault correction. Previously patterned structures can be easily erased and rewritten by laser beams. Second, it is the only technique capable of patterning structures containing different YBCO phases in a single film. The planar combination of superconducting and semiconducting YBCO regions into a single structure has an important potential for microwave and optoelectronic applications. Third, the technique does not require any photomasks or vacuum systems. As a result, laser writing is a convenient and inexpensive patterning technique.

4.3 Oxygen diffusion in YBCO

Oxygen diffusion in YBCO plays an important role in understanding the kinetics and the mechanisms of the O-T or M-I phase transformations [4.18-4.26]. The Arrhenius type of intrinsic diffusivity D could be expressed as

$$D = D_0 \exp(-E_a/k_B T), \quad (4.1)$$

where E_a is the activation energy for dopant diffusion and T is the temperature. A relatively consistent activation energy on the order of ~ 1 eV has been obtained for YBCO by various measuring techniques.

For a single-crystal sample, it has been found that oxygen diffusion is limited primarily to CuO_2 planes and is the fastest along CuO chains. For polycrystalline YBCO, however, grain boundaries serve as a high diffusive pathway for oxygen diffusion into or out the interior of the grain [4.26]. The fast initial accumulation of oxygen atoms makes grain boundaries an oxygen sink for lateral diffusion into the grain. On the other hand, oxygen diffused out of the grain into the grain boundaries can be quickly removed.

Oxygen may enter (in-diffusion) or leave (out-diffusion) the chain O(1) sites according to the defect relation [4.25]:



where O_{O^x} and V_{O} are the neutral and doubly ionized O(1) sites, respectively.

Although investigations on polycrystalline samples showed a faster in-diffusion than out-diffusion [4.18, 4.20], resistivity measurements on single crystals exhibited that the in-diffusion process was an intrinsically slower process [4.27]. The slow in-diffusion is attributed to the initial formation of highly oxygenated shell. The high oxygen concentration within the shell hinders the further in-diffusion process, which is very sensitive to the spatial gradient.

Moreover, it has been found that the efficiency of the in-diffusion depends on whether the oxygen is of molecular, atomic, or ionic form [4.28-4.35]. It has been shown that molecular oxygen is not active enough to oxidize copper at low pressure [4.27]. Atomic oxygen has been demonstrated in the reactive evaporation to produce the best films over the molecular or ionic oxygen [4.29]. It is clear that the *rf* discharge is capable of create activated species of oxygen [4.30-4.32]. In laser ablation, laser pulse has been found to trigger a plasma discharge and dissociate oxygen gas [4.33-4.35].

4.4 Experimental

Figure 4.1 shows the schematics of our laser writing system. A YBCO thin film was mounted inside a gas chamber on a computer controlled X-Y translation stage with a 1- μm step resolution. To reduce heat transfer between substrate and metal stage holder, a glass substrate is sandwiched between the substrate and the holder. The ambient atmosphere is either pure O_2 or N_2 , depending on the desired direction of the oxygen diffusion. Continuous flow of either gas is delivered to the chamber. The near atmospheric pressure of oxygen gas is sufficient to promote the diffusion of molecular oxygen into the film.

The optical part of the system consisted of a *cw* Ar-ion laser ($\lambda=514$ nm), shutter, mirrors, and 20x focusing microscope objective. The laser beam is focused on the surface of the film. The beam spot size is controlled to be 4 to 60- μm in diameter and defines the pattern width. Wider patterns are created by multiple scanning over the desired area. The applied laser fluence is typically between 0.2 and 5 $\text{mW}/\mu\text{m}^2$. The speed of the translation stage is in the range of 0.5-5 $\mu\text{m}/\text{s}$ for in-diffusion and about 50 $\mu\text{m}/\text{s}$ for out-diffusing processes. The above conditions were

selected to ensure that the laser beam provides enough heating to activate effective oxygen diffusion, without causing any structural damage (e.g., surface melting or ablation) to the film at the same time. The temperature of the process is estimated to be 650-600 °C, with most of the laser power used to heat up the substrate rather than YBCO film itself. Due to the block of initially formed oxygen-rich shell, dwell time is required for sufficient oxygen diffusing into YBCO films. The speed of the translation stage is adjusted accordingly to obtain enough time for complete oxygenation or deoxygenation.

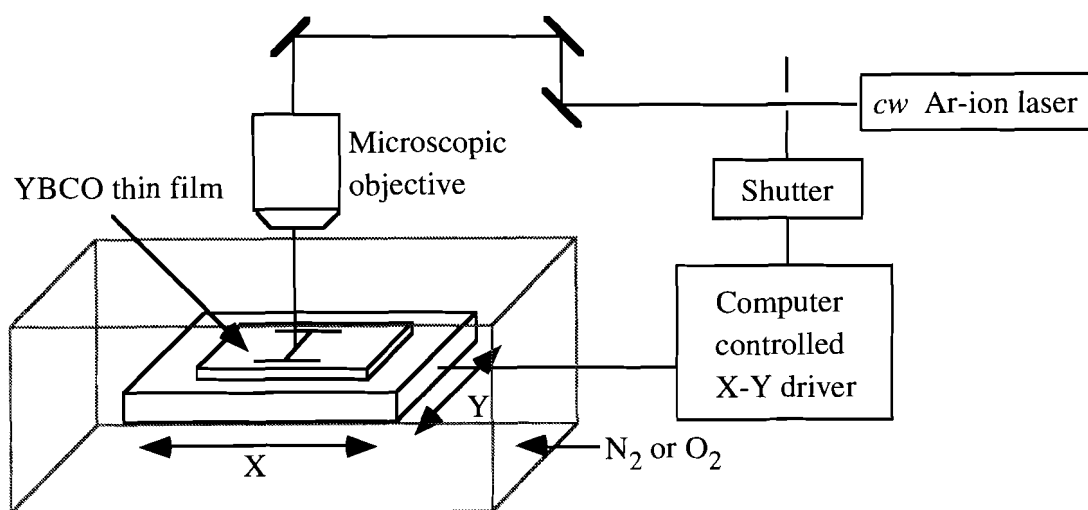


Fig. 4.1 Schematic of a two-dimensional laser-writing system.

4.5 Results and discussion

4.5.1 Oxygen restoring

Laser writing technique is applied to diffuse oxygen into localized patterns on undoped YBCO thin films. Owing to the activation energy of oxygen diffusion, correct temperature profile is important to control both the spatial resolution and the uniformity through whole film thickness. Because of its excellent thermal conductivity, MgO substrate is considered by us as not suitable for writing uniform patterns across the whole film thickness. Although laser heating generates a high temperature on top of the film, the bottom side is nearly as cool as the ambient. The

low temperature near the bottom of YBCO-on-MgO films prevents efficient oxygen diffusion into the grains. To obtain a more uniform temperature profile, a substrate heater is necessary to raise the substrate temperature. On the other hand, the sharp temperature gradient due to effective cooling of the MgO substrate is a possible method for patterning multilayer structures where only a shallow surface layer is required to be modified.

In terms of providing uniform temperature profile, LaAlO₃ substrate is superior to MgO for laser writing. Its low thermal conductivity prevents heat loss to the ambient and causes a much more uniform profile along the film depth. As a result, on LaAlO₃ substrates, it is possible to produce patterns with very uniform depth profiles.

Once the beam size is given by the linewidth of any designed patterns, the other two adjustable parameters for laser writing are the laser power and the speed of the X-Y stage. To find out the optimized parameters of the process, the best conditions must be selected from this two-parameter array. The upper limit of the laser power is set to correspond to the beginning of the film melting. A relative narrow parameter window is found for oxygen in-diffusion process. Outside this window, non-uniform lines with an overwritten center and flurry edges were observed. By contrast, repeatable uniform lines with well defined boundaries were produced when the process parameters were within the optimized window.

Figure 4.2 shows an optical transmission micrograph of a 7- μm -wide oxygen-rich microbridge laser-patterned in a fully oxygen-depleted YBCO-on-LaAlO₃ film. As expected, laser patterned oxygen-rich line (dark) is clearly distinguishable from the surrounding oxygen-poor (light) region. The strong contrast between the oxygen-rich and oxygen-poor regions originates from a large difference in the optical absorption between the two YBCO phases. The width of the patterned line is in good agreement with the beam size. The interface between the oxygen-rich and oxygen-poor YBCO is well defined and very sharp. High magnification investigation using SEM indicated a single micron width of the interface. Therefore, oxygen diffusion is observed to occur in the highly localized region confined by laser beam.

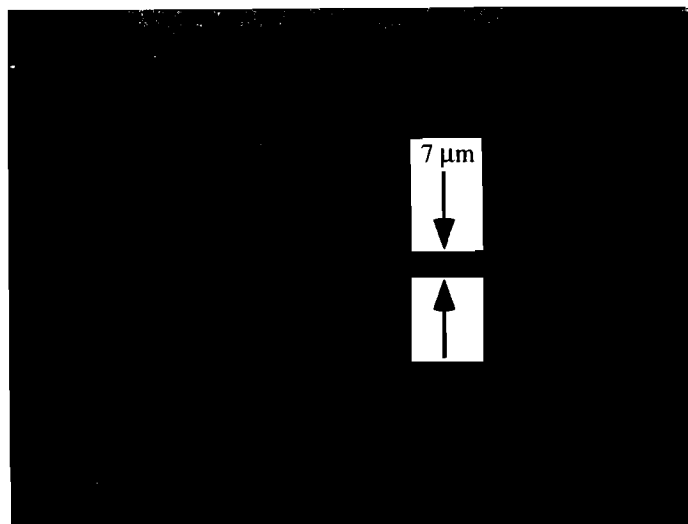


Fig. 4.2 Optical transmission micrograph of a 7- μm -wide oxygen-rich microbridge laser patterned in a fully oxygen-depleted YBCO-on-LaAlO₃ film.

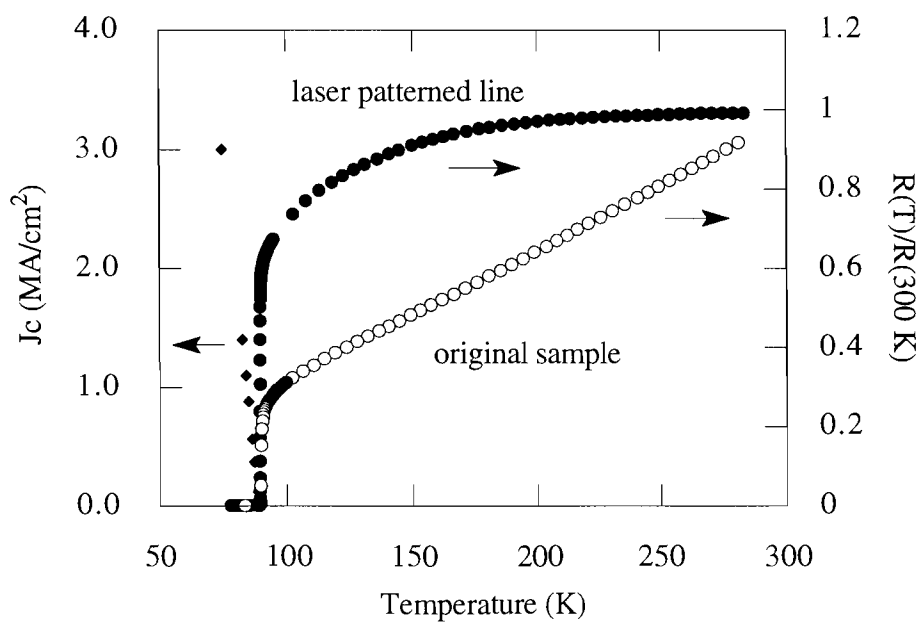


Fig. 4.3 $R(T)$ and $J_c(T)$ curves of a 7- μm -wide laser-written microbridge.

The good superconducting properties of the microbridge shown in Fig. 4.2 are proven by the $R(T)$ and $J_c(T)$ curves displayed in Fig. 4.3. Due to the finite resistivity of the surrounding oxygen-depleted region above 150 K, the $R(T)$ curve above T_c shows a unconventional curve rather than a linear correlation with the temperature. Resistivity measurements show that our laser-patterned line retrieves the same T_c and ΔT_c as that of the as-deposited film ($T_{c0}=89.5$ K and $\Delta T_c=0.5$ K). Moreover, the J_c of the patterned microbridge is found to increase almost linearly as temperature decreases, reaching 3 MA/cm² at 77 K. Such a high value of J_c indicates that laser-written patterns are indeed very uniform and free of structural damages.

4.5.2 Oxygen removing

Besides patterning high-quality oxygen-rich lines in oxygen-poor films, laser writing is also capable of removing O₂ from either fully or partially oxygen-rich YBCO. From the “power-speed” array, a broad parameter window is found for oxygen out-diffusion process.

Figure 4.4 shows a micrograph of a 2- μ m-wide semiconducting line overwritten in N₂ by a laser beam across a 10- μ m-wide superconducting stripe previously patterned by laser writing. Like the semiconducting surrounding, the 2- μ m light region corresponds to the tetragonal phase of oxygen-poor YBCO.

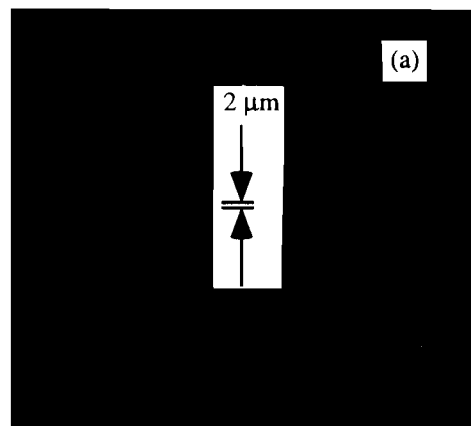


Fig. 4.4 Optical transmission micrograph of a semiconducting line overwritten on a previously patterned superconducting line.

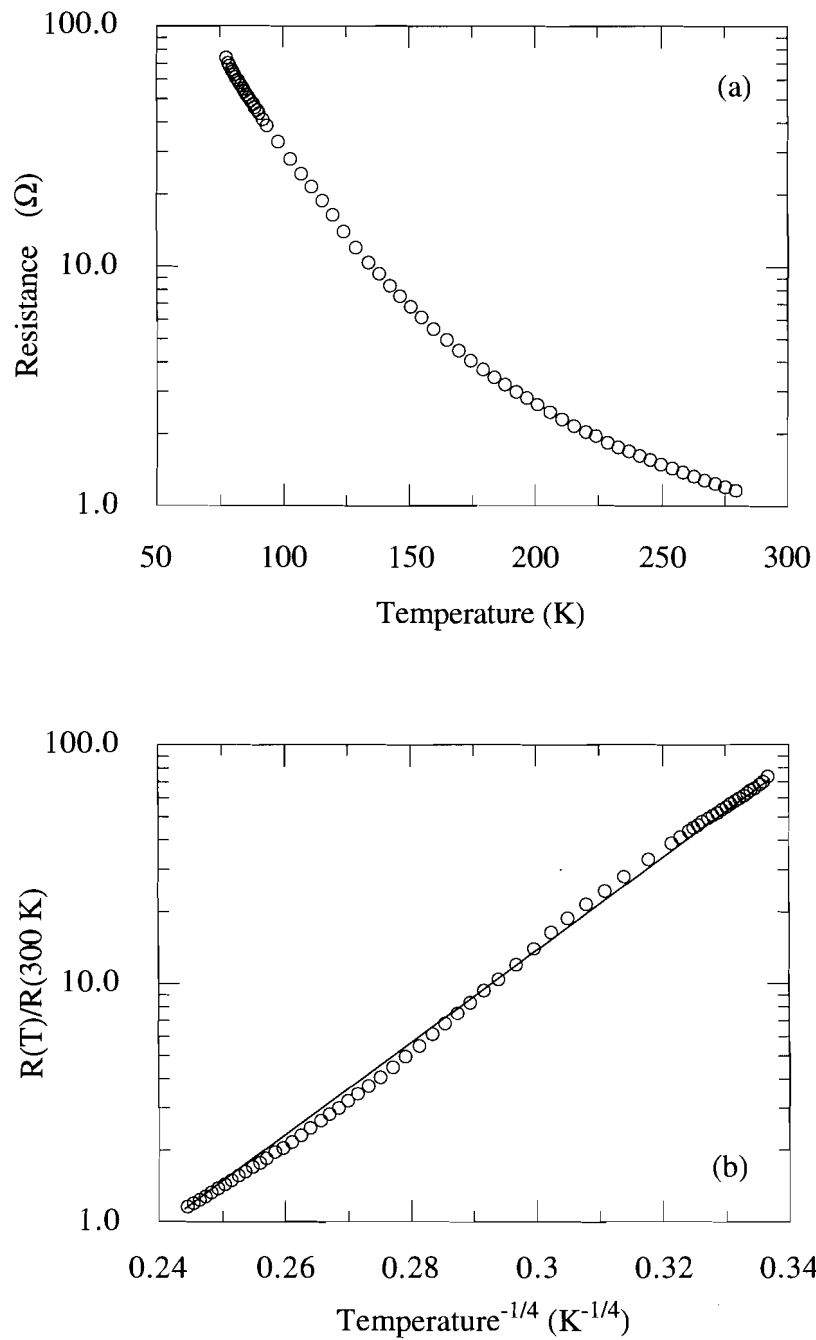


Fig. 4.5 Transport of a 10- μm -wide laser-written oxygen-poor gap. (a) normalized R vs. T , and (b) normalized R vs. $T^{-1/4}$. The solid line represents a theoretical fit given by a 3-dimensional VRH.

The removal of oxygen by laser beam is evident in the $R(T)$ curve of another super/semi/super structure as displayed in Fig. 4.5(a). Figure 4.5(a) displays a typical semiconducting resistive behavior, the same as in the case of furnace-deoxygenated samples. Figure 4.5(b) shows that the $R(T)$ curve follows VRH, a characteristic behavior of semiconducting YBCO (see Sec. 3.5). Therefore, it can be concluded that laser writing is capable of producing oxygen-depleted patterns.

The ability of writing and erasing patterns with desired phase distinguishes laser writing from other existing patterning techniques for YBCO. It also enables the real-time circuit designing and fault correction of YBCO devices.

4.5.3 Pattern stability

While elevated temperatures are required to activate oxygen diffusion, it is almost impossible for oxygen to diffuse in or out of the YBCO film at room temperature [4.22]. Either the semiconducting or the superconducting phase is stoichiometrically stable from the crystallographic point of view. The temporal stability of laser patterned structures was tested by repetitively monitoring a 50- μm wide and 250- μm long superconducting microbridge over the period of 2 years. Figure 4.6 shows the T_c aging investigations of this microbridge.

Up to 8 months, no degradation in the critical temperature and transition width is found in the measured $R(T)$ curves as shown in Fig. 4.6. Instead of suspected degradation, the structure exhibited even a slight enhancement of T_c . This effect is most likely related to a very slow process of chain oxygen ordering at room temperature [4.35, 4.36]. In addition, optical microscope observations showed no change in the morphology of our lines and sharp interfaces of the patterns. The 0.5-K decrease of T_c after 2 years could be a result of surface degradation from the humidity in the lab atmosphere.

4.5.4 Interface

A superconducting/semiconducting/superconducting YBCO structure was used to determine whether electrical behavior of the oxygen-rich/oxygen-poor interface is nonlinear or ohmic. Nonlinear transport interface has been observed in a bulk YBCO samples [4.38]. Figure 4.7 presents a family of current-voltage (I-V) characteristics for a 10- μm -long semiconducting microbridge sandwiched between two 50- μm -wide superconducting strips. All the I-V curves are completely linear in

the entire testing temperature range from 77 to 300 K, indicating the purely resistive behavior of our laser-written interfaces [4.39]. This linear behavior was reproducible as long as the surface of the film was kept free of contamination and damage.

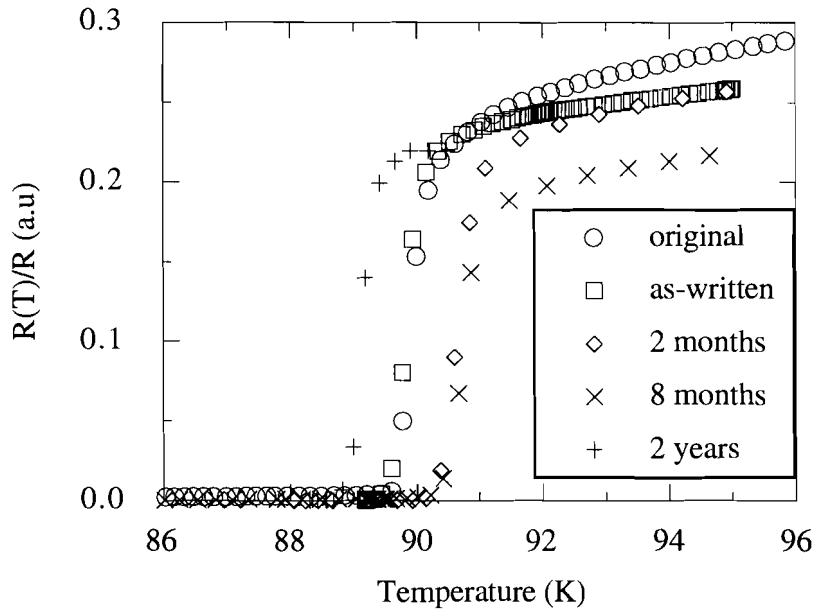


Fig. 4.6 Superconducting transitions of a YBCO microbridge measured over a period of 2 years.

The sharpness of the phase transition in our patterns has been monitored by a Raman spectroscopy measurement which trace the oxygen-concentration across the YBCO films (performed by D. Duke and A. D. Caplin from the Imperial College, London, UK). Figure 4.8 shows the profile of oxygen concentration calculated from Raman measurements. The sample contains 70- μm -wide oxygen-depleted and oxygen-rich lines laser written on a partially oxygen-doped YBCO ($x \sim 6.5$). We note that the phase transition width is on the order of 2 μm , which is the instrumentation resolution of the Raman microscope.

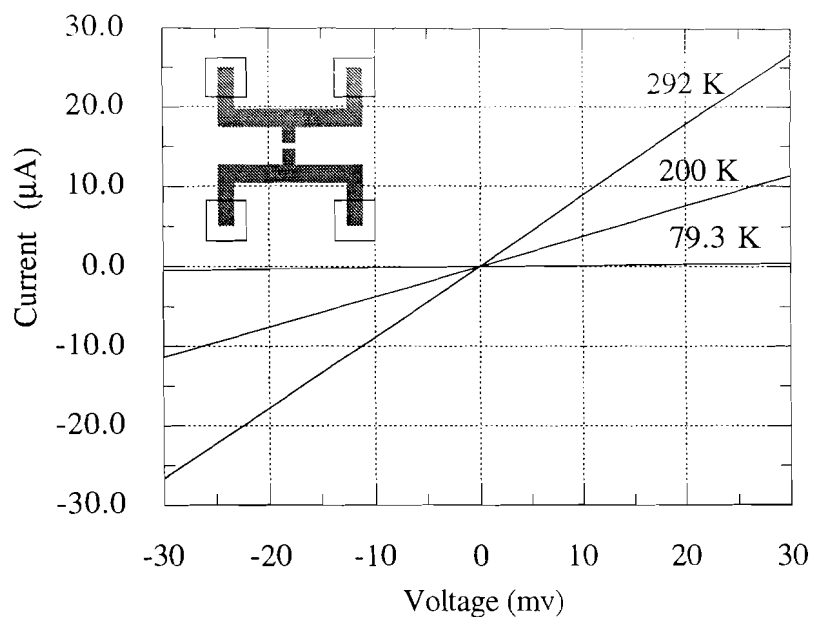


Fig. 4.7 A family of I-V characteristics of a 10- μm -long oxygen-poor YBCO structure. The inset shows the configuration of our test structure.

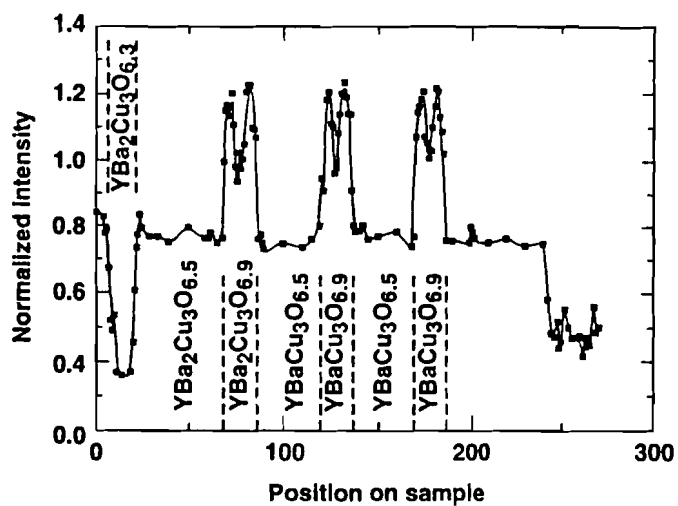


Fig. 4.8 Oxygen concentration profile across laser-written YBCO structures with three different oxygen contents.

4.5.5 Patterning of YBCO/SrTiO₃ bilayers

To test the ability of laser writing to pattern multilayer YBCO structures, we investigated the patterning of YBCO/SrTiO₃ bilayers. 150-nm-thick YBCO thin films sputtered on LaAlO₃ or SrTiO₃ substrates were protected with *in-situ* grown 100-nm-thick SrTiO₃ cap layers [4.11]. The YBCO/SrTiO₃ bilayers were deoxygenated by furnace annealing at 700 °C for 1-2 hours in an Ar atmosphere.

Laser writing has successfully recovered the superconducting properties of the YBCO films beneath the SrTiO₃ top layer. Figure 4.9 demonstrates the oxygen-rich (dark) and oxygen-depleted (bright) patterns fabricated by controlling the oxygen *in-* or *out-*diffusion through the SrTiO₃ top layer. The background is a partially oxygenated YBCO.

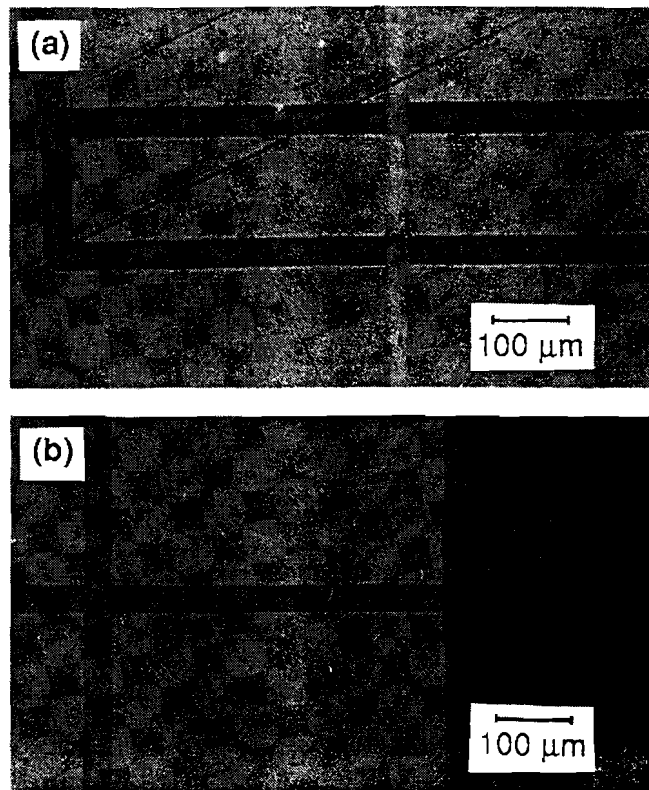


Fig. 4.9 Laser-written patterns fabricated on YBCO/SrTiO₃ bilayers: (a) two 35-μm-wide superconducting lines (dark region) cut by a perpendicular oxygen-depleted line (bright); and (b) part of a SuFET structure [4.44].

4.6 Device fabrication and characterization

4.6.1 Microwave components

To test the performance of the laser written structures, a number of microwave and optoelectronic circuits have been designed and fabricated. For microwave testing, a superconducting coplanar strip (CPS) transmission line and an open-ended superconducting CPS resonator were fabricated on an insulating YBCO film using laser writing. Figure 4.10 shows the optical micrograph of part of the CPS transmission line and resonator. In the CPS resonator, the 10- μm -wide oxygen-poor coupling slots were patterned by erasing in N_2 the previously written oxygen-rich line. Microwave testing of the above structures was performed at Prof. Don Butler's group at the Southern Methodist University. For the open-ended resonator, the unloaded Q-factor measured at 24 K was about 5000 at 6.05 GHz [4.40]. At temperature above T_c (100 K), the unloaded Q-factor was measured to be approximately unity.

Figure 4.11 displays the measured S_{21} parameter of the CPS transmission line as a function of frequency. At room temperature, the line exhibits a lossy attenuation as the structure consists of parallel metallic $\text{YBa}_2\text{Cu}_3\text{O}_7$ and semiconducting $\text{YBa}_2\text{Cu}_3\text{O}_6$ regions. As the temperature drops, the conductivity of the $\text{YBa}_2\text{Cu}_3\text{O}_7$ strips linearly increases and the resistivity of the $\text{YBa}_2\text{Cu}_3\text{O}_6$ area increases according to the Mott's VRH. The attenuation decreases as a result of reduced series and shunt losses. At temperatures below T_c , the CPS strips become superconducting and the $\text{YBa}_2\text{Cu}_3\text{O}_6$ region is almost insulating. The S_{21} parameter is near 0 dB for all the temperatures below T_c , indicating low microwave losses of our CPS transmission line.

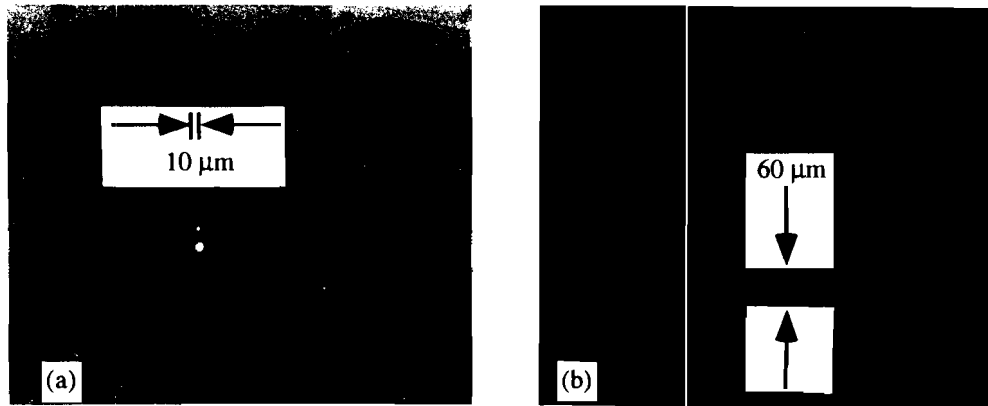


Fig. 4.10 Optical micrograph of part of (a) a microwave resonator, and (b) a coplanar waveguide.

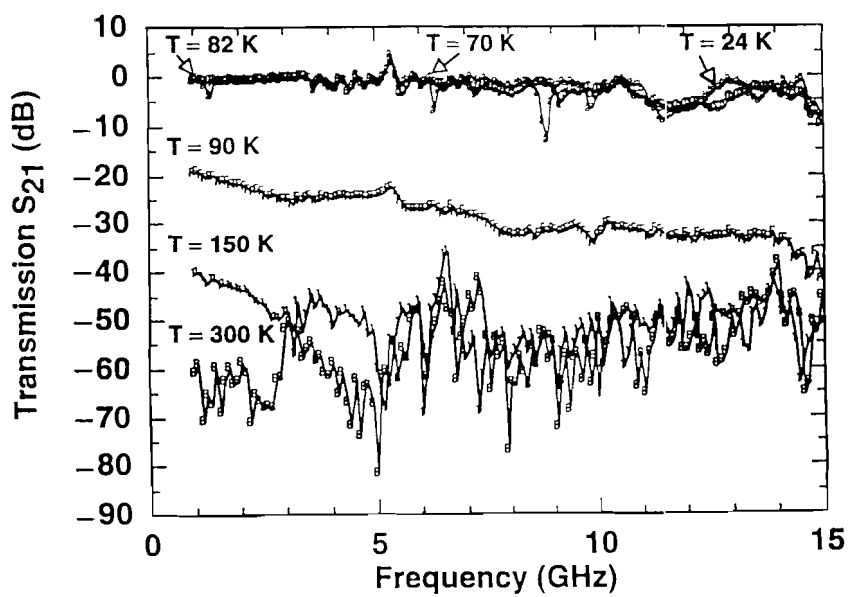


Fig. 4.11 Transmitted power S_{21} versus frequency for a laser written coplanar transmission line from room temperature to 24 K.

4.6.2 Photoconductive switch

Figure 4.13 shows a test structure of a photoconductive switch based on oxygen-depleted YBCO and incorporated into a superconducting coplanar transmission line. The superconducting strips as well as the semiconducting switch were patterned by the laser-writing technique. An interdigitated finger geometry with $4\ \mu\text{m}$ spacing was implemented in the switch design to enhance the signal gain. The incident excitation beam came from a Ti:sapphire laser and was modulated by an acoustic-optic crystal. The beam was then focused on the switch structure to excite free carriers.

The frequency response of this photoconductive switch is shown in Fig. 4.14. Due to a slow response time of the oscilloscope used in these experiments, we did not observe the direct response from individual femtosecond pulses generated by the Ti:sapphire laser. Instead, the photo-induced voltage pulses followed the acoustic-optical crystal modulation frequency. Frequencies above 3 MHz already exceed the bandwidth of the oscilloscope (1 MHz). Therefore, the roll-off in Fig. 4.13 is considered a result of the narrow bandwidth of the oscilloscope. The lifetime of semiconducting YBCO can be estimated as shorter than 300 ns, a value comparable with that obtained by other groups [4.41-4.43].

The results presented in Fig. 4.14 were obtained at room temperature. However, low temperature measurements displayed a similar behavior. No significant effect of persistent photodoping has been observed at our excitation level (1 mW beam power, $40\ \mu\text{m}$ in diameter).

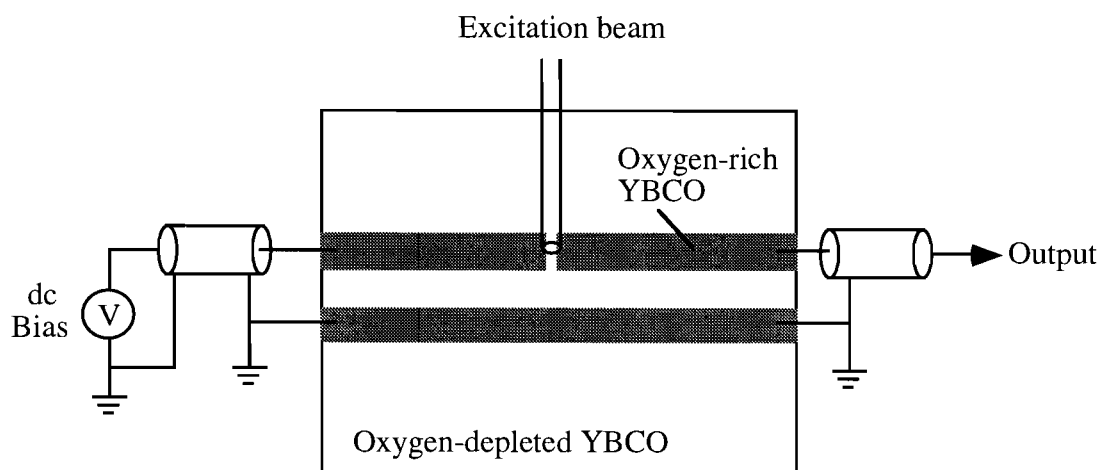


Fig. 4.12 Semiconducting YBCO photoconductive switch: experimental set-up.

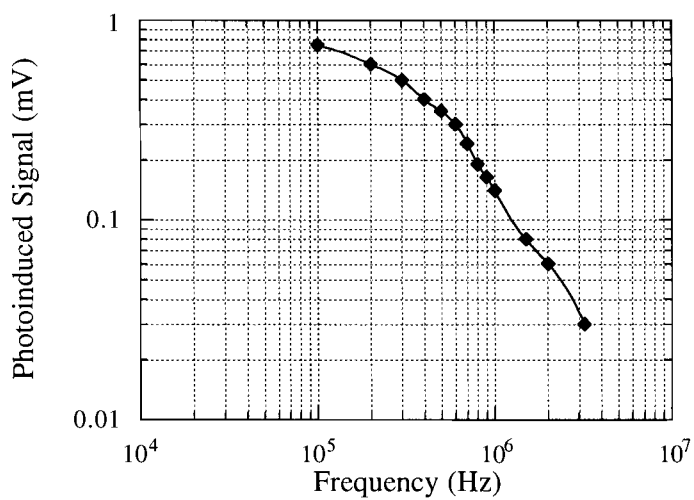


Fig. 4.13 Room temperature response of an oxygen-depleted YBCO photoconductive switch with 4- μm spacing. Bias at 25.6 V.

4.7 Summary

We have developed a laser-writing technique which is proven to be a practical and reliable method of patterning YBCO thin-film devices and circuits. The method results in planar structures with well-defined lines and undamaged crystalline structure. The superconducting properties of our oxygen-rich patterns are found to be as good as that of the original films. At the same time, the patterned oxygen-depleted regions are practically insulating at low temperatures. The nondestructive nature of laser writing makes it the only existing way of combining superconducting and semiconducting YBCO regions in the same film. The ability of erasing previously patterned structures is also extremely convenient for circuit restructuring and fault correction. Laser writing is capable of patterning through a top SrTiO₃ layer. Our test structures are shown to exhibit long-term stability. Furthermore, the method is free of photomasks and chemicals. And that prevents contamination of the film surface. In terms of cost, the technique does not require any vacuum equipment and/or pumps.

Various structures, such as microwave resonators, CPS transmission lines, field-effect devices [4.44] and photoconductive switches were successively fabricated using this method. We believe that laser writing will continue to play an important role in the new HTS electrical and optoelectronic applications.

References

Conventional Patterning

- [4.1] See, e.g., A. I. Braginski, Springer Proceedings in Physics, vol. **64**, H. Koch and H. Lübbig, eds., Springer-Verlag, Berlin, Heidelberg, (1992).
- [4.2] J. S. Martens, T. E. Zipperian, D. S. Ginley, V. M. Hietala, C. P. Tigges, and T. A. Plut, "The effects of processing sequences on the microwave surface resistance of TlCaBaCuO," J. Appl. Phys. **69**, 8268 (1991)

Laser Writing

- [4.3] M. Rothschild, J. H. C. Sedlacek, J. G. Black, and D. J. Ehrlich, "Laser patterning of Metal oxide superconductor films by reactive solid-state transformation," IEEE Electron Device Lett. **9**, 68 (1988)
- [4.4] M. Rothchild, J. H. C. Sedlacek, J. G. Black, and D. J. Ehrlich, "Reversible laser chemically induced phase transformations in thin-film Ba₂YCu₃O_x superconductors," Appl. Phys. Lett. **52**, 404, (1988)
- [4.5] R. R. Krchnavek, S. W. Chan, C. T. Rogers, F. De Rosa, M. K. Kelly, P. F. Miceli, and S. J. Allen, "Transport in reversibly laser-modified YBa₂Cu₃O_{7-x} superconducting thin films," J. Appl. Phys. **65**, 1802, (1989)
- [4.6] R. C. Dye, R. E. Muenchausen, N. S. Nogar, A. Mukherjee, and S. R. J. Brueck, "Laser writing of superconducting patterns on YBa₂Cu₃O_x films," Appl. Phys. Lett. **57**, 1149 (1990).
- [4.7] Y. Q. Shen, T. Freltoft, and P. Vase, "Laser writing and rewriting on YBa₂Cu₃O₇ films," Appl. Phys. Lett. **59**, 1365 (1991).
- [4.8] R. Sobolewski, W. Xiong, and W. Kula, "Patterning of thin-film high- T_c circuits by the laser-writing method," IEEE Trans. Appl. Supercon. **3**, 2896 (1993)
- [4.9] R. Sobolewski, W. Xiong, W. Kula, and J. R. Gavaler, "Laser patterning of Y-Ba-Cu-O thin-film devices and circuits," Appl. Phys. Lett. **64**, 643 (1994)
- [4.10] W. Xiong, W. Kula, and R. Sobolewski, "Fabrication of High- T_c superconducting electronic devices using the laser-writing technique," in *Advances in Cryogenic Engineering*, **40**, p. 385, edited by R. P. Reed et al., (Plenum Press, 1994).
- [4.11] W. Kula, W. Xiong, and R. Sobolewski, "Laser patterning of YBa₂Cu₃O_x thin films protected by *in-situ* grown SrTiO₃ cap layer," IEEE Trans. Appl. Supercond. **5**, 1177 (1995)

Oxygen Dependence

- [4.12] J. D. Jorgensen, B. W. Veal, A. P. Paulikas, L. J. Nowicki, G. W. Crabtree, H. Claus, and W.K. Kwok, "Structural properties of oxygen-deficient $\text{YBa}_2\text{Cu}_3\text{O}_{7-\delta}$," *Phys. Rev. B* **41**, 1863 (1990)
- [4.13] E. Osquiguil, M. Maenhoudt, B. Wuyts, and Y. Bruynseraede, "Controlled preparation of oxygen deficient $\text{YBa}_2\text{Cu}_3\text{O}_x$ films," *Appl. Phys. Lett.* **60**, 1627 (1992)

Laser Direct Writing in VLSI

- [4.14] D. J. Ehrlich, and J. Y. Tsao, in *VLSI Electronics: Microstructure Science*, vol. 7, p. 129, ed. N. G. Einspruch, Academic Press (1983)
- [4.15] D. J. Ehrlich and J. Y. Tsao, "Submicrometer-linewidth doping and relief definition in silicon by laser-controlled diffusion," *Appl. Phys. Lett.* **41**, 297 (1982)
- [4.16] D. J. Ehrlich, R. M. Osgood Jr., and T. F. Deutsch, "Laser chemical technique for rapid direct writing of surface relief in silicon," *Appl. Phys. Lett.* **38**, 1018 (1981)
- [4.17] D. J. Ehrlich, R. M. Osgood Jr., and T. F. Deutsch, "Laser microreaction for deposition of doped silicon films," *Appl. Phys. Lett.* **39**, 957 (1981)

Oxygen Diffusion in YBCO

- [4.18] J. Park, P. Kostic, and J. P. Singh, "Electrical conductivity and chemical diffusion in sintered $\text{YBa}_2\text{Cu}_3\text{O}_y$," *Mater. Lett.* **6**, 393 (1988)
- [4.19] K. N. Tu, S. I. Park, and C. C. Tsuei, "Diffusion of oxygen in superconducting $\text{YBa}_2\text{Cu}_3\text{O}_{7-\delta}$ oxide upon annealing in helium and oxygen ambients," *Appl. Phys. Lett.* **51**, 2158 (1988)
- [4.20] K. N. Tu, N. C. Yeh, S. I. Park, and C. C. Tsuei, "Diffusion of oxygen in superconducting $\text{YBa}_2\text{Cu}_3\text{O}_{7-\delta}$ ceramic oxides," *Phys. Rev. B* **39**, 304 (1989)
- [4.21] X. M. Xie, T. G. Chen, and Z. L. Wu, "Oxygen diffusion in the superconducting $\text{YBa}_2\text{Cu}_3\text{O}_{7-x}$," *Phys. Rev. B* **40**, 4549 (1989)
- [4.22] S. J. Rothman, J. L. Routbort, and J. E. Baker, "Tracer diffusion of oxygen in $\text{YBa}_2\text{Cu}_3\text{O}_{7-\delta}$," *Phys. Rev. B* **40**, 8852 (1989)
- [4.23] B. W. Veal, H. You, A. P. Paulikas, H. Shi, Y. Fang, and J. W. Downey, "Time-dependent superconducting behavior of oxygen-deficient $\text{YBa}_2\text{Cu}_3\text{O}_x$: possible annealing of oxygen vacancies at 300 K," *Phys. Rev. B* **42**, 4770 (1990)

- [4.24] J. L. Tallon and M. P. Staines, "Oxygen self-diffusion coefficient in the superconductor $\text{YBa}_2\text{Cu}_3\text{O}_{7-\delta}$ from internal friction measurements," *J. Appl. Phys.* **68**, 3998 (1990)
- [4.25] J. R. LaGraff, P. D. Han, and D. A. Payne, "Resistance measurements and oxygen out-diffusion near the orthorhombic-tetragonal phase transformation in single-crystal $\text{YBa}_2\text{Cu}_3\text{O}_{7-\delta}$," *Phys. Rev. B* **43**, 441 (1991)
- [4.26] Y. Chen, J. Zhang, Z. Wu, "Oxygen diffusion in *c*-axis-oriented $\text{YBa}_2\text{Cu}_3\text{O}_x$ films," *Supercond. Sci. Technol.* **5**, 463, 1992
- [4.27] J. R. LaGraff, P. D. Han, and D. A. Payne, "Oxygen in-diffusion and out-diffusion in single crystal $\text{YBa}_2\text{Cu}_3\text{O}_{7-\delta}$," in *Defects in Materials*, eds. P. D. Bristowe, J. E. Epperson, J. E. Griffith, and Z. Liliental-Weber, *Mat. Res. Soc. Symp. Proc.* **209**, 801 (1991)

***In situ* Oxygenation**

- [4.28] E. S. Hellman, D. G. Schlom, N. Missert, K. Char, J. S. Harris, M. R. Beasley, A. Kapitulnik, T. H. Geballe, J. N. Eckstein, S. L. Weng, and C. Webb, "Molecular-beam epitaxy and deposition of high- T_c superconductors," *J. Vac. Sci. Technol. B* **6**, 799 (1989)
- [4.29] N. Missert, R. Hammond, J. E. Mooj, V. Matijasevic, P. Rosenthal, T. H. Geballe, A. Kapitulnik, M. R. Beasley, S. S. Laderman, C. Liu, E. Garwin, and R. Barton, "In situ growth of superconducting YBaCuO using reactive electron-beam coevaporation," *IEEE Trans. Magn.* **MAG-25**, 2418 (1989)
- [4.30] T. Goto, H. Matsunoto, T. Hirai, "Preparation of superconducting $\text{YBa}_2\text{Cu}_3\text{O}_{7-x}$ films by ECR plasma sputtering," *Jpn. J. Appl. Phys.* **28**, L88 (1989)
- [4.31] R. M. Silver, A. B. Berezin, M. Wendman and A. L. de Lozanne, "As-deposited superconducting Y-Ba-Cu-O thin films on Si, Al_2O_3 , and SrTiO_3 substrates," *Appl. Phys. Lett.* **52**, 2174 (1988)
- [4.32] T. Terashima, Y. Bando, K. Iijima, K. Yamamoto, and K. Hirata, "Epitaxial growth of $\text{YBa}_2\text{Cu}_3\text{O}_{7-x}$ thin films on (110) SrTiO_3 single crystals by activated evaporation," *Appl. Phys. Lett.* **53**, 2232 (1988)
- [4.33] X. D. Wu, A. Inam, T. Venkatesan, C. C. Chang, E. W. Chase, P. Barboux, J. M. Tarascon, and B. Wilkens, "Low-temperature preparation of high T_c superconducting thin films," *Appl. Phys. Lett.* **52**, 754 (1988)
- [4.34] Z. P. Zheng, Q. Y. Ying, S. Witanachchi, Z. Q. Huang, D. T. Shaw, and H. S. Kwok, "***," *Appl. Phys. Lett.* **54**, 954 (1989)

- [4.35] G. Koren, A. Gupta, and R. J. Baseman, "Role of atomic oxygen in the low-temperature growth of $\text{YBa}_2\text{Cu}_3\text{O}_{7-\delta}$ thin films by laser ablation," *Appl. Phys. Lett.* **54**, 1920 (1989)

Oxygen Ordering

- [4.36] B. W. Veal, A. P. Paulikas, H. You, H. Shi, Y. Fang, and J. D. Downey, "Observation of temperature-dependent site disorder in $\text{YBa}_2\text{Cu}_3\text{O}_{7-\delta}$ below 150 °C," *Phys. Rev. B* **42**, 6305 (1990)
- [4.37] G. Nieva, E. Osquiguil, J. Guimpel, M. Maenhoudt, B. Wuyts, Y. Bruynseraede, M. B. Maple, and I. K. Schuller, "Photoinduced enhancement of superconductivity," *Appl. Phys. Lett.* **60**, 2159 (1992)

Semiconducting/Superconducting Interface

- [4.38] C. M. Ray, H. Mathias, L. R. Testardi, and S. Skirius, "High dielectric constant and nonlinear electric response in nonmetallic $\text{YBa}_2\text{Cu}_3\text{O}_{6+\delta}$," *Phys. Rev. B* **45**, 10639 (1992)
- [4.39] R. Sobolewski, W. Xiong, W. Kula, and B. McIntyre, "Electrical and structural properties of the YBCO superconducting-semiconducting interface," *Physica B* **194-196**, 2143 (1994)

Microwave Testing

- [4.40] W. N. Maung, D. P. Butler, W. Xiong, W. Kula, and R. Sobolewski, "Propagation characteristics of monolithic YBaCuO coplanar strip transmission lines fabricated by laser-writing patterning technique," *IEEE Microwave and Guided Wave Lett.* **4**, 132 (1994)

Lifetime of Photoexcited Carriers

- [4.41] G. Yu, A. J. Heeger, G. Stucky, N. Herron, and E. M. McCarron, L. Cong, G. C. Spalding, C. A. Nordman, and A. M. Goldman, "Phase separation of photogenerated carriers and photoinduced superconductivity in high- T_c materials," *Phys. Rev. B* **45**, 4964 (1992)
- [4.42] F. A. Hegmann, J. S. Preston, "Origin of the fast photoresponse of epitaxial $\text{YBa}_2\text{Cu}_3\text{O}_{7-\delta}$ thin films," *Phys. Rev. B* **48**, 16023 (1993)
- [4.43] M. Johnson, "Nonbolometric photoresponse of $\text{YBa}_2\text{Cu}_3\text{O}_{7-\delta}$ films," *Appl. Phys. Lett.* **59**, 1371 (1991)

FET Structure

- [4.44] W. Kula and R. Sobolewski, "Charging effect in partially oxygen-depleted superconducting Y-Ba-Cu-O thin films," *Phys. Rev. B* **49**, 6428 (1994)

5 FEMTOSECOND OPTICAL RESPONSE

5.1 Introduction

In this Chapter, we investigate the nonequilibrium optical response by a femtosecond pump-probe technique. We first give a brief review of the sources and models of pump-probe signals. Then we study the relaxation of photoexcitation in YBCO thin films containing several different oxygen contents. The experiments performed in this Chapter are trying to explain the origins of the optical response in YBCO and to depict the material's band structure.

5.1.1 Pump-probe technique

With the advance of femtosecond laser pulses [5.1-5.4], femtosecond spectroscopy has emerged as a powerful tool for the investigation of transient nonequilibrium processes in solid state materials [5.5-5.30]. Due to the difference in the heat capacities between the electrons and lattice, it is possible to excite by femtosecond lasers a non-equilibrium distribution of electrons with temperatures much higher than that of the lattice. The hot carriers then lose their energy by scattering with carriers, LO phonons, and acoustic phonons. Hence, femtosecond-resolved relaxation of photo-excited carriers contains valuable information about *e-ph* coupling strength and other carrier dynamics.

Standard pump-probe experiments measure the difference in reflection and transmission before and after pulsed-laser excitation. In case of a non-degenerate two-band semiconductor, the band filling term of the observed difference in absorption can be expressed as

$$\Delta\alpha = \alpha_0 (f_v - f_c - 1), \quad (5.1)$$

where f_c and f_v are the probability of electron occupancy in the conduction and valence bands after photoinjection, respectively, and α_0 is the linear absorption coefficient for interband transition. Therefore, bandfilling results in PB signals.

For small changes in optical constants, the normalized differential reflectivity $\Delta R/R$ can be expressed as

$$\Delta R/R = [(\partial R/\partial \epsilon_1)\Delta \epsilon_1 + (\partial R/\partial \epsilon_2)\Delta \epsilon_2] / R, \quad (5.2)$$

where ϵ_1 and ϵ_2 are the real and imaginary parts of the dielectric constant.

Any change in the electron distribution will affect the interband transition which is directly related to ϵ_2 . Hence, electron temperature rise by laser heating is expected to generate $\Delta R/R$ with a sign determined by the probe energy.

Besides the PB from the band filling, PA is also possible to contribute to the differential signals. Sources for induced absorption include intra-band free-carrier absorption, excitation of carriers trapped in localized states, and nonlinear two-photon absorption. Among them, transition from localized states has the biggest transition cross section because it is a dipole-allowed first-order process.

Band renormalization or bandgap shrinkage are significant contributions for bandedge excitation of small-gap semiconductors. However, the effect of band renormalization is negligible in our study because of the large CT gap (~ 1.7 eV) of the semiconducting YBCO and the pump energy (2 eV) far above the band edge.

For superconductors, the optical conductivity σ is written in term of the two fluid model as

$$\sigma = N_n \sigma_n + N_s \sigma_s , \quad (5.3)$$

where N_n and N_s are the relative density of the normal (Drude) and the superconducting electrons, σ_n and σ_s are their respective optical conductivities.

The generation of QP leads to an increase in N_n at the expense of N_s . The change in dielectric constants is then expressed as [5.16, 5.24]

$$\Delta\epsilon_1 \approx \delta N_{qp} \omega_p^2 / \omega^4 \tau^2 , \quad (5.4a)$$

$$\Delta\epsilon_2 \approx \delta N_{qp} \omega_p^2 / \omega^3 \tau , \quad (5.4a)$$

where δN_{qp} is the fraction of photogenerated QP, ω_p is the plasma frequency, $1/\tau$ is the scattering rate of Drude carriers.

According to Eq. (5.2), QP generation caused change in $\Delta\epsilon_1$ and $\Delta\epsilon_2$ will result in a change of transient reflectivity.

5.1.2 Fermi smearing model

For d-band metals, Fermi smearing has been successfully applied in modeling the sign change of differential reflection ΔR and transmission ΔT signals [5.11, 5.12]. The schematic diagram in Fig. 5.1 shows how the change in Fermi distribution by laser heating would affect the absorption. Fermi smearing model predicts that the PB and PA occur for probe energies above and below E_F , respectively. Therefore, the sign flip in differential signals corresponds to probing across E_F . At E_F , no differential signal is supposed to be observed.

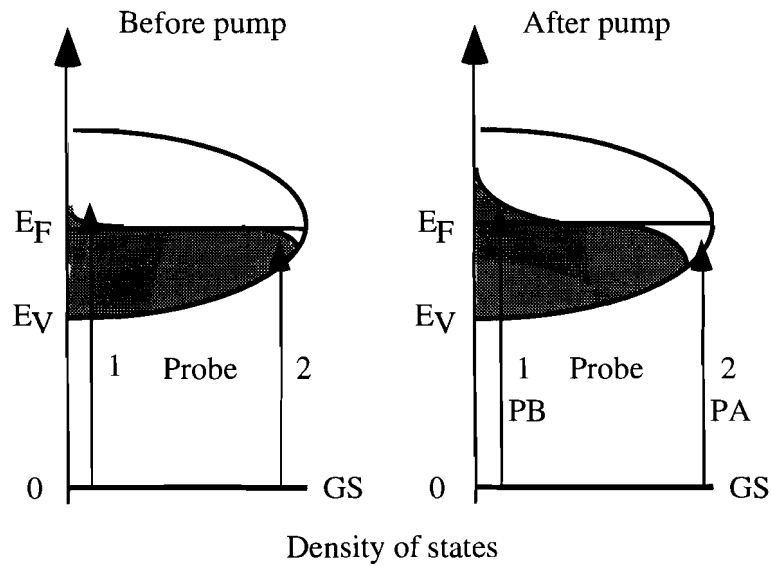


Fig. 5.1 Schematic of the Fermi smearing model. Photoinduced bleaching (PB) and absorption (PA) are observed by probe above and below the Fermi level, respectively.

To quantitatively simulate the ΔR and ΔT signals, the Fermi distribution is expressed as a function of electron temperature and probe energy

$$f(\hbar\omega, T) = 1/\{1+\exp([\hbar\omega-(E_F-E_C)]/k_B T)\} , \quad (5.5)$$

$$\Delta f(\hbar\omega, T_e) = f(\hbar\omega, T_e) - f(\hbar\omega, T_0) , \quad (5.6)$$

where E_c is the separation between the ground state and the conduction band, T_0 and T_e are the electron temperatures before and after the pump excitation, respectively, and $\hbar\omega$ the photon energy.

Figure 5.2 shows a sign flip in the distribution function when probe energy crosses the Fermi level. According to Fermi smearing model, no sign change can be produced by changing the pump intensity alone.

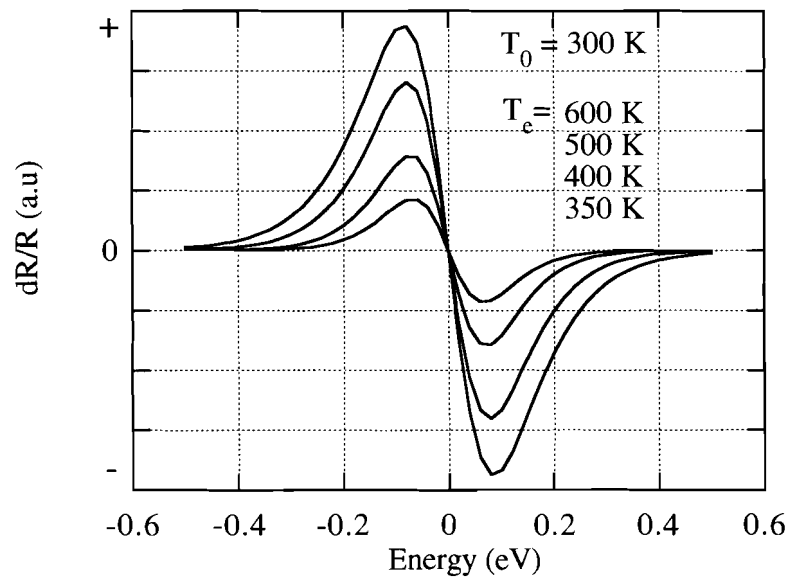


Fig. 5.2 Fermi smearing of differential signals. Energy zero is set to be $E_F - E_v$.

5.1.3 Nonequilibrium electron heating

The heat generated by the pump pulse is also subjected to diffuse out of the excited area. However, due to the short (ps) measurement window of our experiments, the slow thermal diffusion process can be neglected. Therefore, the temporal profiles of the electron and lattice temperatures T_e and T_L can be modeled as [5.21, 5.29]

$$C_e(T_e)[dT_e/dt] = -g(T_e - T_L), \quad (5.7a)$$

$$C_L[dT_L/dt] = g(T_e - T_L), \quad (5.7b)$$

where $C_e = \gamma T_e$ is the electronic specific heat, $C_L = C(T_L/\Theta)^3$ is the lattice specific heat, Θ is the Debye temperature, $g = 3\hbar\gamma\lambda\langle\omega^2\rangle/\pi k_B$ is the coupling constant, and $\lambda\langle\omega^2\rangle$ is the e - ph coupling constant.

According to the above equations, an initial fast decay in differential signals is expected, as the electron temperature drops quickly by e - ph coupling. After thermal equilibrium is reached among the electron and lattice systems, a slow bolometric component is predicted to represent the heat diffusion process.

From Eqs. (5.7a) and (5.7b), the electron temperature can be expressed by the following nonlinear differential equation:

$$T_e[d^2T_e/dt^2] + [dT_e/dt]^2 + (3\hbar/\pi k_B)\lambda\langle\omega^2\rangle[1 + (\gamma/C_L)T_e][dT_e/dt] = 0, \quad (5.8)$$

where the variables are the electron temperatures and the e - ph coupling constant.

Transient reflectivity can be also expressed as

$$\Delta R \approx a\Delta T_e + b\Delta T_L \quad (5.9)$$

For given boundary conditions $T_e(0)$ and $T_e(\infty)$, time-resolved $\Delta R/R$ can be numerically fitted by adjusting the e - ph coupling constant $\lambda\langle\omega^2\rangle$ in Eq. (5.8). As a result, the strength of the e - ph coupling is obtained from the pump-probe results.

5.2 Experimental

Optical density of YBCO films was measured using a Perkin-Elmer Lambda-9 spectrometer. The femtosecond pump-probe response was investigated in the temperature range between room temperature and 12 K. Figure 5.3 shows the experimental set-up of our pump-probe system. Laser pulses of 120 fs in duration were generated by a colliding-pulse-mode-locked laser and further amplified by a copper vapor laser at a repetition rate of 8.5 KHz. While the pump energy was fixed at 2 eV, variable probe energies were obtained from the white-light continuum. Pump and probe beams were cross-polarized and focused on the sample surface with a diameter of 30 μm . With the pump energy of 10 nJ per pulse, the injected carrier density is estimated to be $3 \times 10^{20} \text{ cm}^{-3}$. Lock-in and differential detection techniques were used to enhance the signal-to-noise ratio. Time-resolved transient changes in both R and T were measured simultaneously so that the $\Delta\alpha$ and the unperturbed absorption coefficient (α_0) could be obtained by numerical fitting. Low temperature measurements were performed in a continuous He-flow optical cryostat using 2 eV pump and probe pulses.

The measured reflection and transmission can be expressed as functions of the real (n) and imaginary (k) part of refractive index:

$$T = \Delta T + T_0 = T(n, k), \quad (5.10a)$$

$$R = \Delta R + R_0 = R(n, k), \quad (5.10b)$$

Consequently, values of n, k, and absorption coefficient ($\alpha = 4\pi k/\lambda$) can be converted from the measured T and R by solving numerically Eqs. (5.10) [5.15]. Fabry-Perot effects are included in the fitting program to eliminate the artifact of interference. Figure 5.4 shows an example conversion of n and k from a set of measured $\Delta R/R$ and $\Delta T/T$ data in a semiconducting YBCO thin film.

As described in Section 3.4, semiconducting YBCO-on-MgO thin films of 200-nm thick were fabricated using *rf* magnetron sputtering and in-situ annealing in 100 mTorr of Ar. Oxygen-doped YBCO-on-LaAlO₃ samples of 200-nm thick were off-axis sputtered and annealed to obtain samples with T_c 's of 30 K, 55 K, and 60 K, as well as $T_c \approx 90$ K.

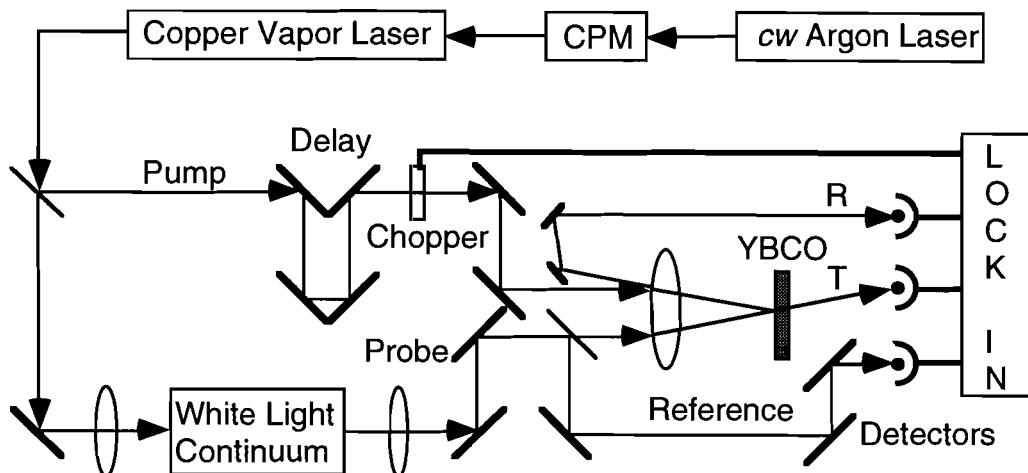


Fig. 5.3 Experimental set-up of an ultrafast pump-probe system.

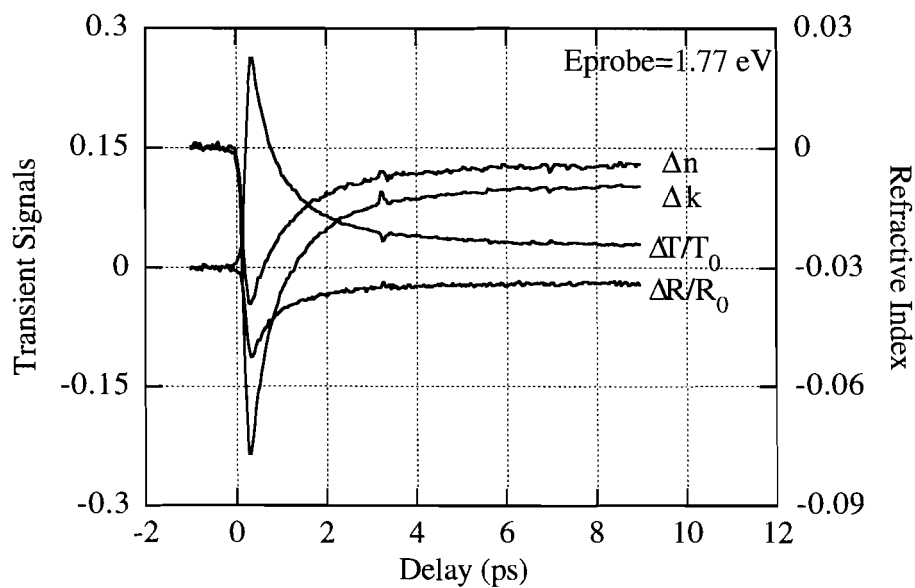


Fig. 5.4 Converting n and k from ΔR and ΔT data taken from a semiconducting YBCO film.

5.3 Results and Discussion

5.3.1 Semiconducting YBCO

Recent femtosecond studies by Matsuda *et al.* [5.30] have observed both PB and PA signals in insulating cuprates. The initial subpicosecond decay of the bleaching was assigned to the emission of two magnons; however, the origin of the induced absorption below 1.6 eV was not fully understood. As we outlined in Chapter 2, semiconducting $\text{YBa}_2\text{Cu}_3\text{O}_x$ ($x < 6.3$) is considered as a charge-transfer insulator with a CT gap between the Cu-3d upper Hubbard band and the O-2p band. Several corresponding band diagrams have been proposed based on Raman [5.31, 5.32], photoconductivity [5.33, 5.34], and photoluminescence [5.35] studies. Moreover, transient photoconductivity investigation [5.33] as well as our photoconductive switch measurement (see Sec. 4.6.2) have shown a long lifetime (>10 ns) for photo-excited carriers in insulating YBCO.

In this Section, we explore the mechanisms of the nonequilibrium optical response in oxygen-poor semiconducting YBCO by means of femtosecond pump-probe technique. We investigate the transient response as a function of probe energy from 1.65 to 2.10 eV and ambient temperature between 12 to 300 K.

Figure 5.5 shows the room temperature linear absorption spectrum of an oxygen-depleted $\text{YBa}_2\text{Cu}_3\text{O}_x$ ($x \sim 6.0$) film. Two main absorption features near 1.78 and 2.8 eV are clearly resolved. These two peaks are related to the CT transition between the filled Cu-3d UHB and the empty O-2p band (in the hole picture) [5.31, 5.34] (see also Sec. 2.3). In addition, a broad band tail is observed below the fundamental absorption peak near 1.78 eV. Low-temperature photoconductivity studies have indicated that the lowest interband transition occurs at 1.5 eV [5.34]. Therefore, it can be concluded that all probe energies used in our study (>1.65 eV) are greater than the CT gap. Thus, bleaching is expected as a result of band filling. Also shown in Fig. 5.5 are the values of α_0 (dots) obtained from the numerical fitting of our pump-probe data. The good agreement between our data points and the linear absorption curve demonstrates the effectiveness of our fitting program.

Figure 5.6 displays the normalized transient absorption at probe energies from 1.65 to 2.1 eV. As expected, bleaching ($\Delta\alpha < 0$) is observed at all wavelengths immediately after the excitation. The pulse width-limited rise of the bleaching is due to the efficient redistribution of photo-excited carriers by carrier-carrier (CC) scattering. As in the case of conventional semiconductors such as GaAs [5.7], CC

scattering occurs on a sub-100 fs time scale when the injected carrier density is higher than 10^{19} cm^{-3} . The redistributed carriers, which now occupy the previously empty states, block the possible transitions across the CT gap.

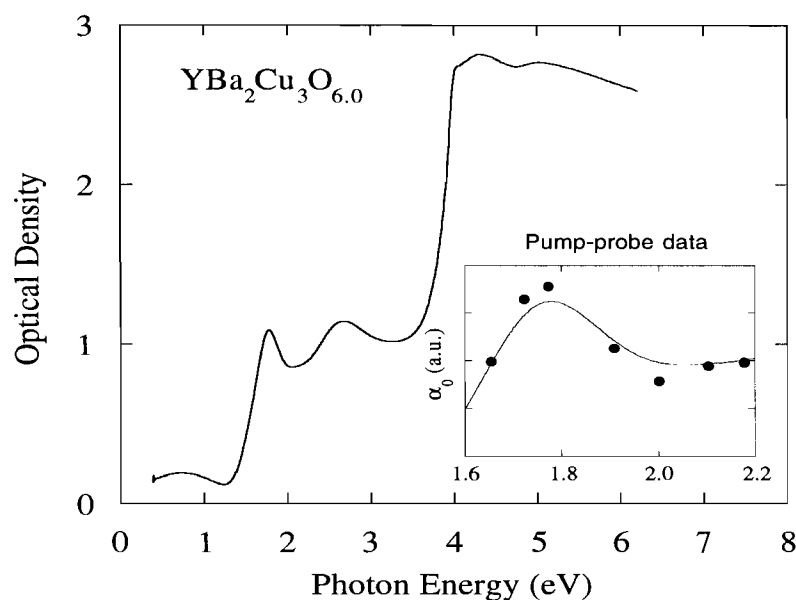


Fig. 5.5 Linear absorption spectrum of semiconducting YBCO. Solid dots in the inset are obtained from our pump-probe measurements.

The excess energy of the excited carriers is then transferred to the lattice. Since the carrier lifetime ($>10 \text{ ns}$) is much longer than our 10-ps measurement window, one would expect carrier accumulation near the band edge prior to recombination. As a consequence, for photon energies near the band edge, the recovery of bleaching should become a slow process. In some cases, the bleaching could even increase with time as the carriers cool down to near room temperature. Instead, we observe that recovery is slowest near 1.9 eV (650 nm), rather than near the band edge (1.65 eV or 750 nm). Close to the band edge, the bleaching disappears in a few picoseconds. Further, the signal even becomes positive after 5 ps (Fig. 5.6), indicating induced absorption. The appearance of induced absorption at 1.65 eV suggests that the photoinjected carriers can be further excited.

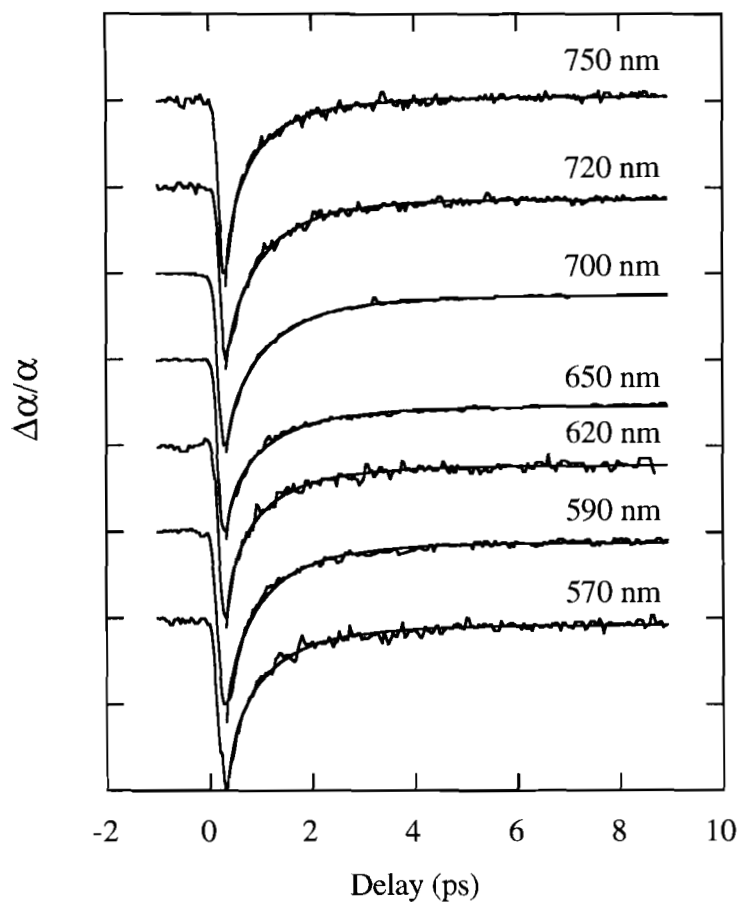


Fig. 5.6 Differential absorption of semiconducting YBCO at several probe energies. The smooth lines are stretched-exponential fits.

The relaxation measured by the recovery of the bleaching in Fig. 5.6 cannot be fitted by a simple exponential function. Instead, it follows a stretched exponential. The smooth solid lines in Fig. 5.6 are the fits produced by a stretched exponential plus a constant term

$$\Delta\alpha/\alpha = C_1 \exp[-(t/\tau)^\beta] + C_2. \quad (5.10)$$

While the stretched term models the relaxation of hot carriers, the constant term represents the excess heat that escapes by the much slower process of heat diffusion (bolometric process). The fits provide essentially constant values for $\tau \approx 0.6$ ps and $\beta \approx 0.7$ over the whole investigated spectral range at room temperature. The stretched exponential decay indicates the co-existence of multiple processes that cannot be represented by a unique time constant [5.36, 5.37].

Stretched-exponential decay has been considered as a universal law in describing any dispersive systems [5.36]. For a system at equilibrium, any deviation (Δ) from the equilibrium can be expressed as [5.37]

$$d\Delta/dt = -v\Delta , \quad (5.11)$$

In case of a constant rate v , the decay follows a simple exponential relation $\Delta = \Delta_0 \exp(-vt)$. However, if there coexist many time scales, a stretched-exponential decay is expected

$$\Delta = \Delta_0 \exp[-(t/\tau)^\beta] , \quad (5.12)$$

where τ is a time constant, β is the dispersive factor and $0 < \beta < 1$.

The stretched exponential is well understood in the case of multiple trapping. Given a distribution of localized states such as $\exp(-E/k_B T_0)$, it has been found that both τ and β are temperature dependent [5.36, 5.37]

$$\beta = T/T_0 , \quad (5.12a)$$

$$\tau = \tau_0 \exp(E_a/k_B T) , \quad (5.12b)$$

To test the above model, we performed low-temperature measurements. Figure 5.7 shows time-resolved $\Delta T/T$ as a function of temperature. The recovery of $\Delta T/T$ is slightly faster at lower temperatures. As in Fig. 5.6, the relaxation process can be accurately fitted by a stretched-exponential (the smooth solid lines in Fig. 5.7).

Figure 5.8 plots the time constant τ and dispersion factor β obtained from the stretched-exponential fitting in Fig 5.7 as a function of temperature. Unlike in the case of multiple trapping where $\beta = T/T_0$, our value of β is independent of temperature. Moreover, the time constant τ cannot be fitted by a thermally activated exponential. Instead, it decreases with decreasing temperature. Therefore, our results cannot be explained by the multiple trapping. We believe that the increase in decay rate at low temperature may be related to the emission of acoustic phonons.

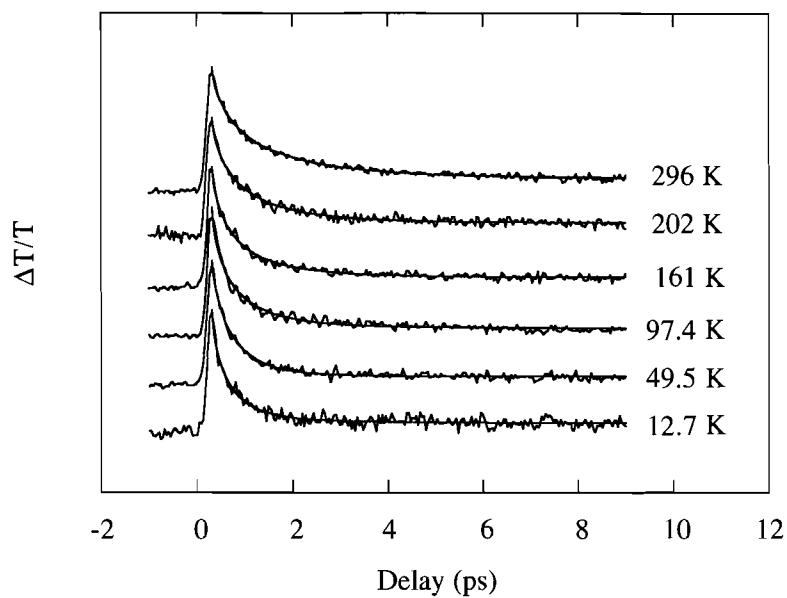


Fig. 5.7 $\Delta T/T$ of semiconducting YBCO at several temperatures. Fitting using $\Delta T/T = C_1 \exp[-(t/\tau)^\beta] + C_2$ is shown in solid smooth lines.

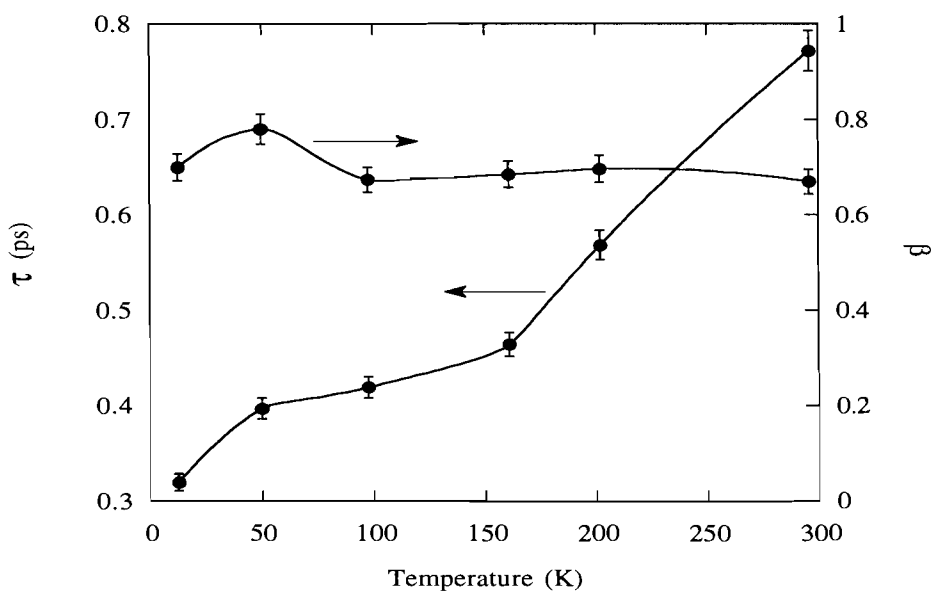


Fig. 5.8 Stretched-exponential parameters for the data from Fig. 5.8. Solid lines are guides to the eye.

In Fig. 5.9, the transient absorption spectra from Fig. 5.6 are plotted for different delays. The maximum bleaching occurs at ~ 320 fs, consistent with the pulse-width limited rise time and fast CC scattering. Moreover, the maximum bleaching is at 1.9 eV, an energy at which no spectral peak in the linear absorption is observed. There is no observable spectral shift of the 1.9-eV peak with time over a 10 ps window. The decay in Fig. 5.9 shows clearly that the slowest recovery occurs near 1.9 eV instead of at the band edge. The small increase in absorption at 1.65 eV after 5 ps indicates that induced absorption overcomes bleaching. From the injected carrier density of about $3 \times 10^{20} \text{ cm}^{-3}$ and the magnitude of induced absorption ($\sim 300 \text{ cm}^{-1}$), we deduce a transition cross section of about $3 \times 10^{-18} \text{ cm}^2$. Due to the partial cancellation of the induced absorption by bleaching, the real transition cross-section for free-carrier absorption could be larger than this. Nevertheless, the above value is consistent with free-carrier absorption involving extended states and is much smaller than the dipole-allowed transitions from carriers trapped in the localized states. Therefore, the most likely bleaching cancellation process is the free-carrier absorption inside the O-2p band.

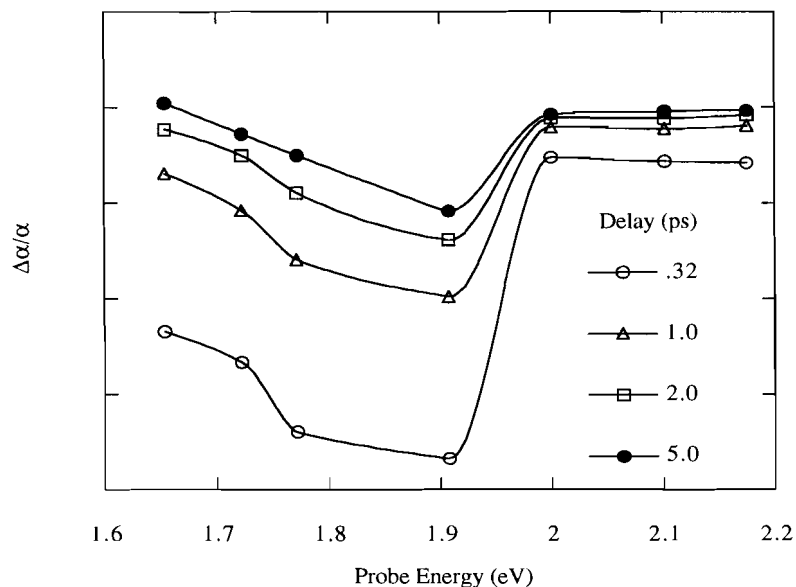


Fig. 5.9 Differential absorption spectrum at several delays after the maximum bleaching.

Free-carrier absorption inside the O-2p band depends strongly on the probe energy. At probe energy larger than the band width of O-2p band, no intraband transition is available and only bleaching exists. Below that threshold energy, however, induced absorption and bleaching coexist and cancel with each other. The net result is an increase of the recovery rate of the bleaching and eventually induced absorption. Consequently, the fact that the fastest recovery occurs near 1.9 eV corresponds to the threshold for free-carrier absorption. The recovery peak near 1.9 eV should be related to the bandwidth of the O-2p band. For smaller probe energies, the induced absorption is stronger because more occupied states are available for intraband transitions. As a result, the recovery rate of the differential signals increases drastically towards the band edge.

5.3.2 YBCO thin film with $T_c \approx 30$ K

As discussed in detail in Chapter 2, oxygen doping of semiconducting YBCO results in a O-T phase transition. The corresponding electronic structure changes from semiconducting to metallic at room temperature. The filling of chain O(1) sites removes electrons from the CuO_2 plane and creates free holes in the conduction band. As in other d-band metals, Fermi smearing is expected to contribute to the differential signal in the metallic YBCO.

Figure 5.10 plots the optical density of a YBCO thin film with $T_c = 30$ K. Comparing with that of semiconducting YBCO (Fig. 5.5), the CT peak near 1.8 eV drops significantly, but it is still visible. Simultaneously, free-carrier absorption term increases drastically at low energies.

Transient $\Delta R/R$ of a 30-K YBCO sample is shown in Fig. 5.11. Bleaching signals are observed for all three probe energies. The sources of the bleaching could be either the Fermi smearing or the band filling across the CT gap. However, due to the low oxygen doping, the Fermi level is expected to lie far below our probe energies. Thus, the bleaching is most likely the consequence of band filling.

Figure 5.12 demonstrates the intensity dependence of the bleaching probed at 1.91 eV. The inset shows a linear relation between the maximum bleaching and pump intensity. This fact further supports that band filling is the origin of bleaching in our 30-K YBCO sample.

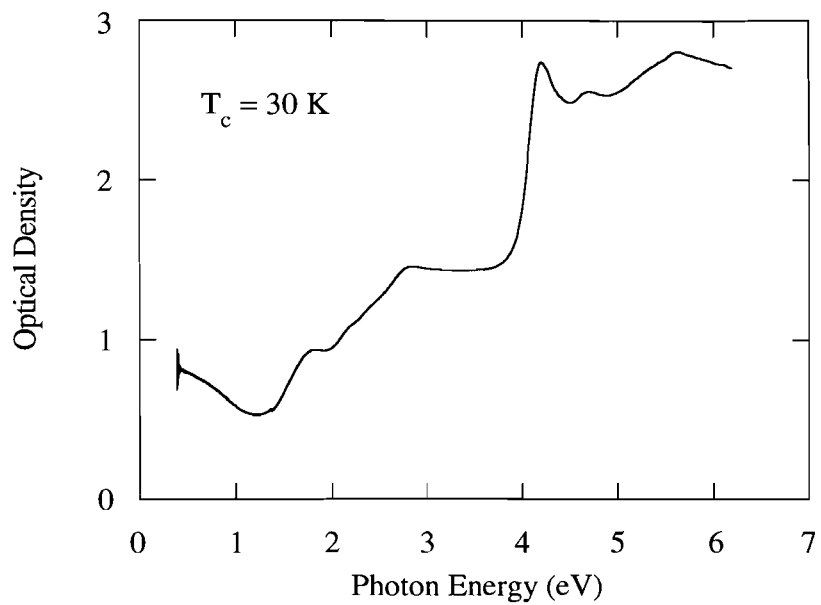


Fig. 5.10 Linear absorption spectrum of YBCO with $T_c=30$ K.

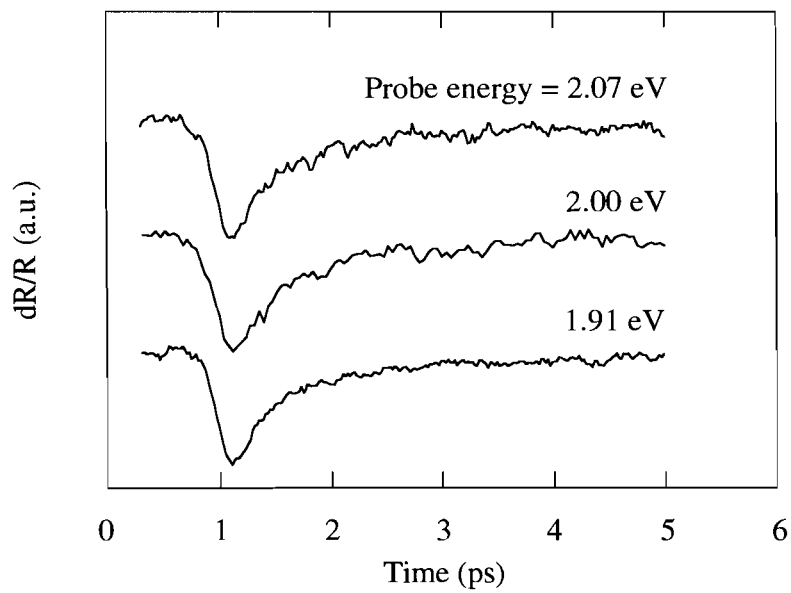


Fig. 5.11 Transient reflection of YBCO with $T_c=30$ K.

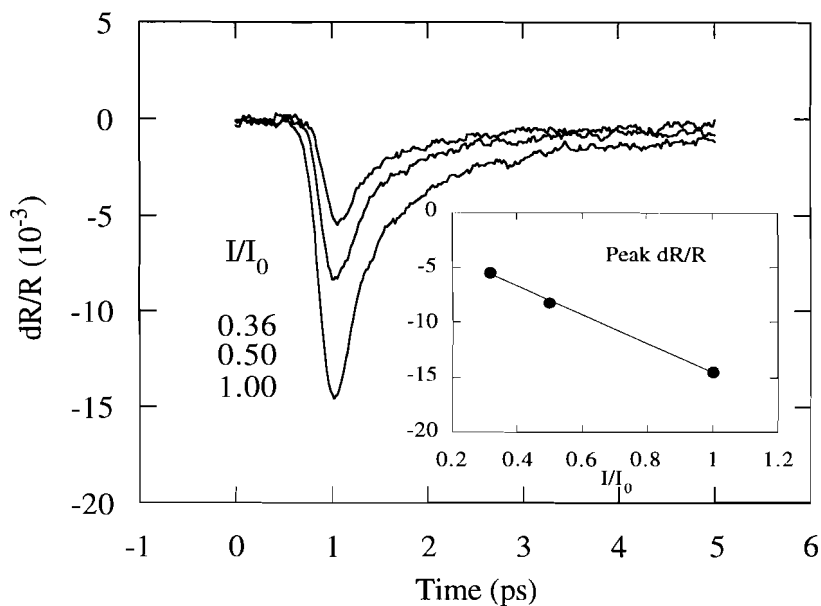


Fig. 5.12 Pump intensity dependence of a $T_c=30$ K YBCO thin film. Maximum intensity $I_0=300 \mu\text{J}/\text{cm}^2$. Probe at 1.91 eV.

5.3.3 YBCO thin film with $T_c \approx 60$ K

Further oxygen doping continues to raise the T_c until a plateau is reached near 60 K. Figure 5.13 presents the optical density for a YBCO thin film with $T_c \approx 60$ K. While the free-carrier absorption keeps increasing at the low-energy end, the CT feature below 2 eV becomes hardly distinguishable.

White-light investigation of $\Delta R/R$ in a $T_c=55$ K YBCO thin film is displayed in Fig. 5.14. Both positive and negative signals are observed in the fast components. In terms of the Fermi smearing model, the sign flip between 2.07 and 2.10 eV would be an indication of probing across the Fermi level. After the fast peak, the slow tail surprisingly increases with time instead of following a bolometric decay.

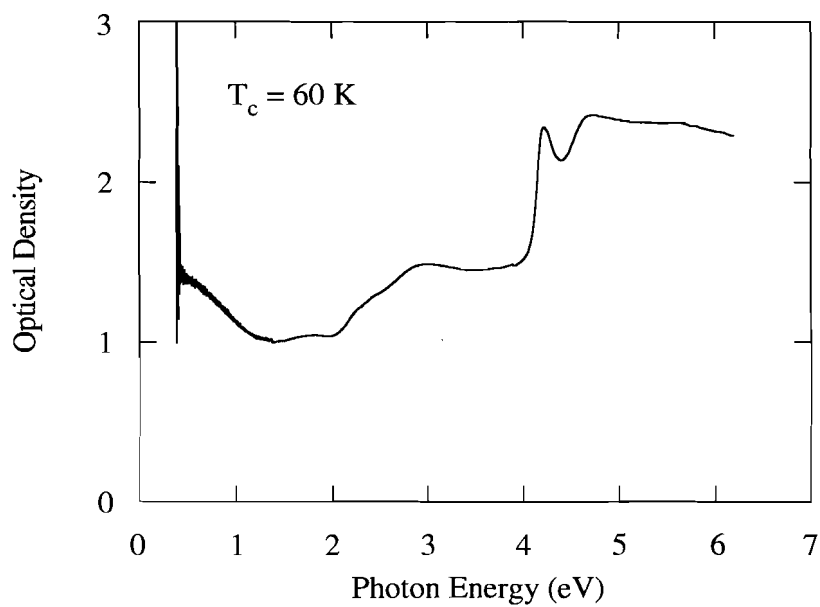


Fig. 5.13 Linear absorption spectrum of YBCO with $T_c=60$ K.

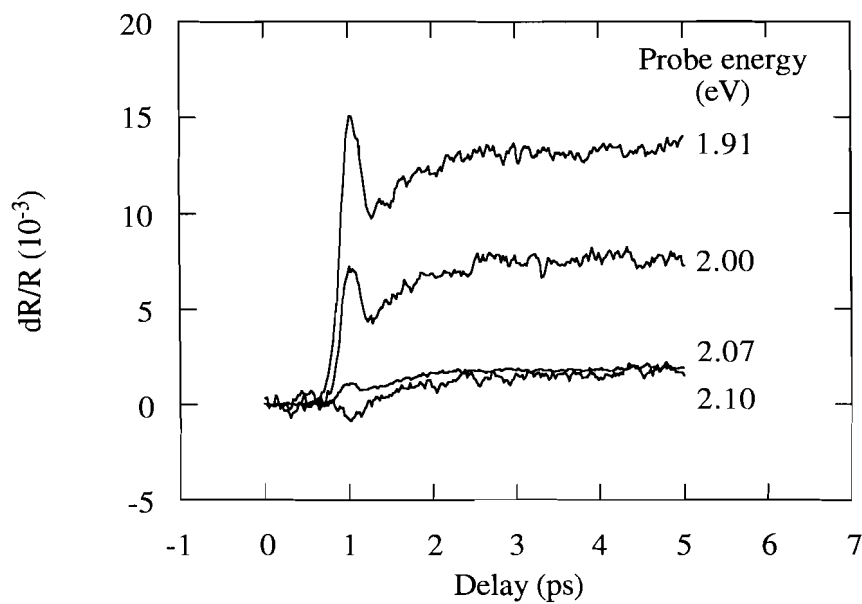


Fig. 5.14 $\Delta R/R$ of a YBCO film with $T_c=55$ K. Pump at $300 \mu\text{J}/\text{cm}^2$.

Figure 5.15 illustrates another white-light response of the 55-K film but with a much lower pump intensity. This time, the sign flip occurs between 1.65 and 1.72 eV. This value is about 0.4 eV lower than that of high intensity case. Hence, the energy level for sign flip appears to be dependent on the pump intensity. Such an observation cannot be explained by the standard Fermi smearing model (see Sec. 5.1.2). If the bleaching at low intensity corresponds to probe energy (1.91 eV) above the Fermi level, the increase of pump intensity would only enhance the bleaching (Fig. 5.2). Thus, the intensity dependence might be interpreted as a photoinduced shift in the Fermi level (photodoping).

White-light $\Delta R/R$ signals for a 60-K YBCO sample are presented in Fig. 5.16. The result is very similar to that of 55-K sample with a sign flip between 2.07 and 2.10 eV. The dependence of $\Delta R/R$ on pump intensity with a 2.0-eV probe is shown in Fig. 5.17. At high intensities, the fast peak is distinguishable from the slow component. The ratio between the fast peak and the slow tail drops significantly towards low pump intensity.

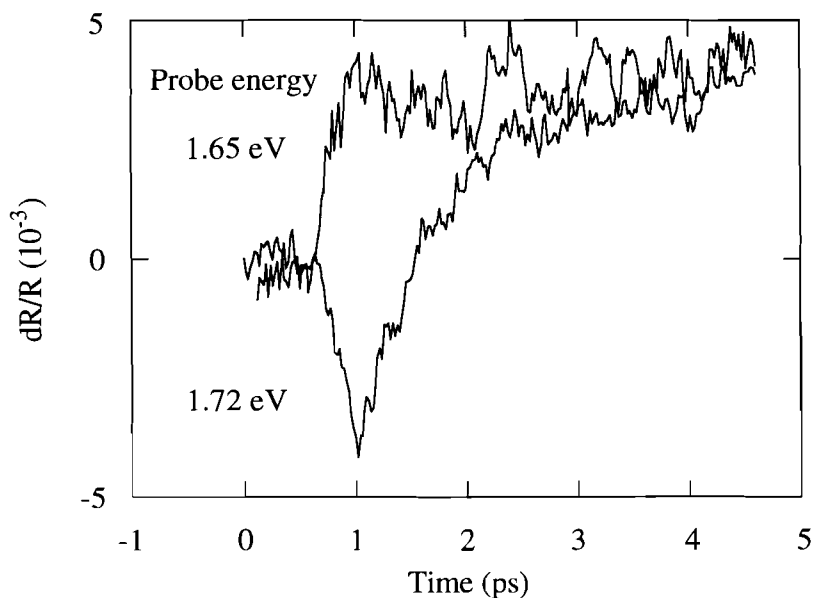


Fig. 5.15 $\Delta R/R$ of a YBCO film with $T_c=55$ K. Pump at $75 \mu\text{J}/\text{cm}^2$.

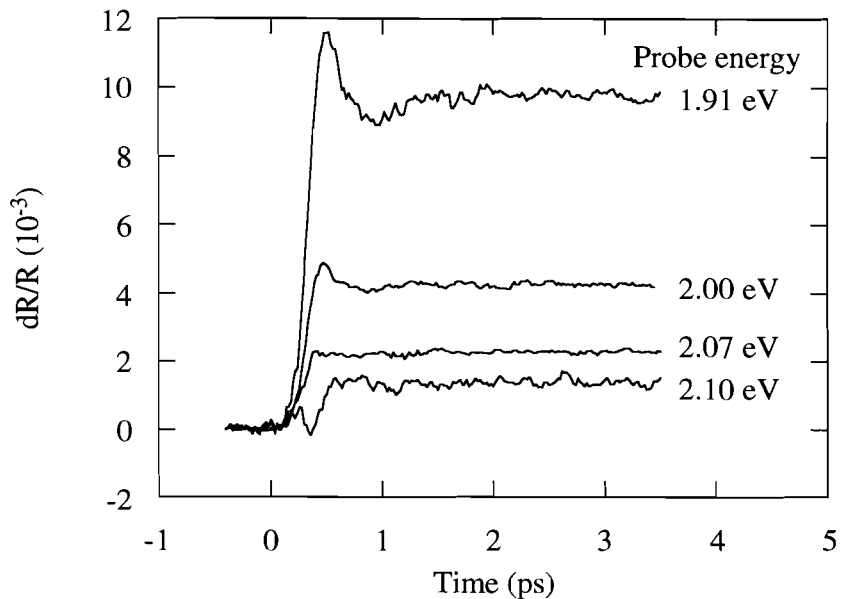


Fig. 5.16 $\Delta R/R$ of a $T_c=60$ K YBCO thin film. Pump at $160 \mu\text{J}/\text{cm}^2$.

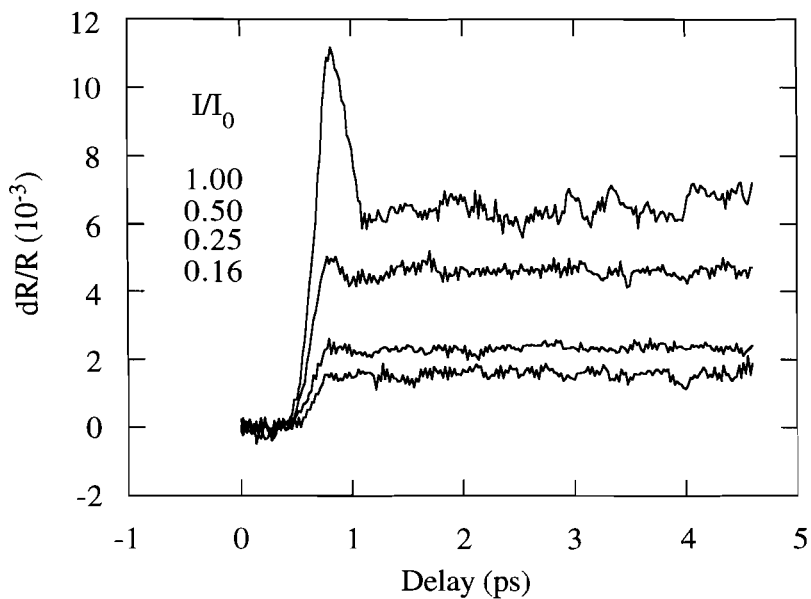


Fig. 5.17 Pump intensity dependence of a $T_c=60$ K YBCO thin film. Maximum intensity $I_0=300 \mu\text{J}/\text{cm}^2$. Probe at 2 eV.

The change in $\Delta R/R$ as a function of pump intensity is displayed in Fig. 5.18 for probing at 1.91 eV. Like the 55-K sample, the 60-K film exhibits a strong intensity dependence of the signal sign. Whereas the negative signal appears at low intensity, the positive peak occurs at high intensities.

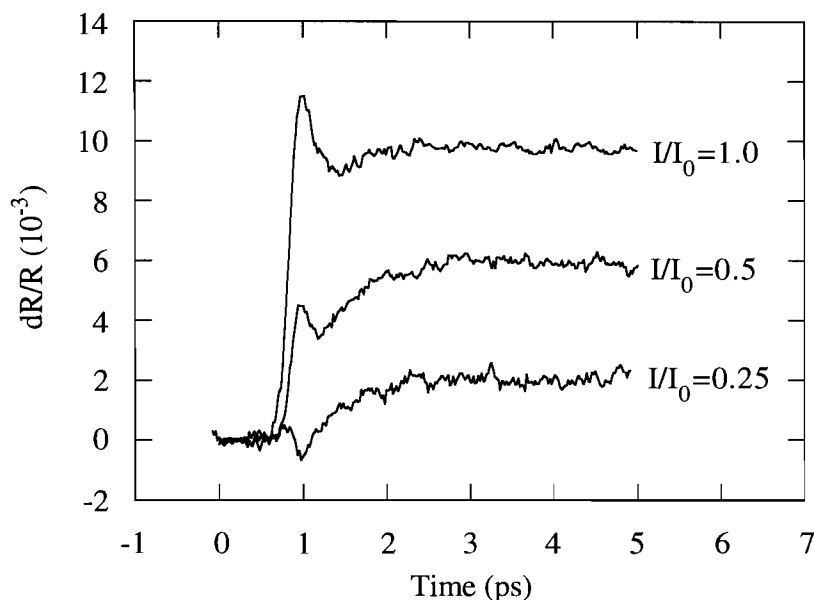


Fig. 5.18 Pump intensity dependence of a $T_c=60$ K YBCO thin film. Maximum intensity $I_0=160 \mu\text{J}/\text{cm}^2$. Probe at 1.91 eV.

Possible explanation for the strong intensity dependence seems to be related to the photodoping effect observed in partially doped YBCO [5.38-5.40]. At high intensities, either the charge-transfer and oxygen-ordering mechanisms proposed for photodoping could result in an up shift in the Fermi level of the CuO_2 plane. As a consequence, the probe energy which is above the E_F at low intensity becomes below the E_F at high intensity. Correspondingly, the sign of the peak signal changes from negative to positive with increasing pump intensity. Therefore, low intensity result is believed to reflect more accurately the original position of the Fermi level in our samples. The observations at low intensity indicate that E_F is below 1.9 eV for the 55-K and 60-K samples.

5.3.4 Fully oxygenated YBCO

In oxygen-rich YBCO, the maximum filling of O-p band results in a maximum Fermi energy. Figure 5.19 plots the optical density of a 90-K YBCO thin film. Below 2 eV, no feature associated with the interband transition across the CT gap is observed. Only the free-carrier term dominates at the low energy end. Like other d-band metals [5.11, 5.12], Fermi smearing is expected to govern the differential signal in this metallic phase of YBCO at room temperature.

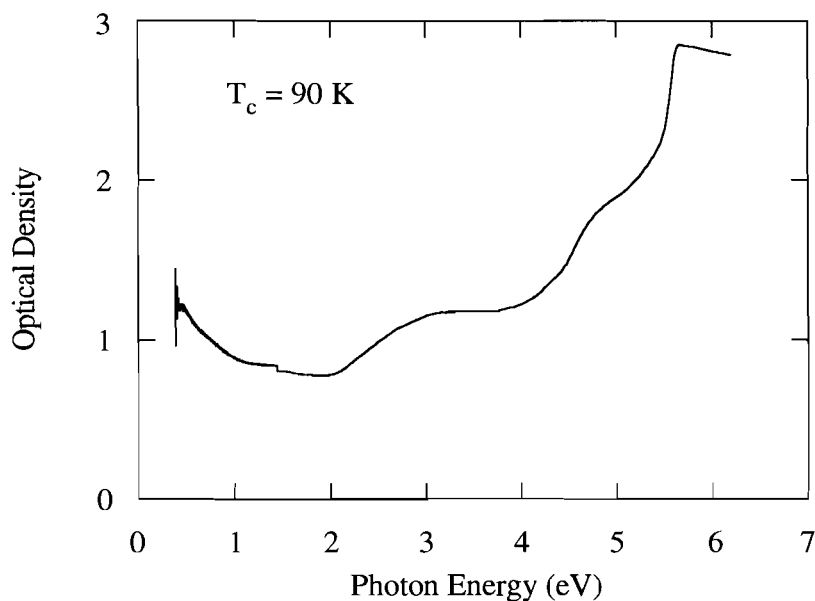


Fig. 5.19 Linear absorption spectrum of YBCO with $T_c=90$ K.

White-light probed $\Delta R/R$ of an oxygen-rich YBCO is displayed in Fig. 5.20. Similar profiles with a fast component followed by a long-lasting plateau are observed for all probe energies. The fast component can be understood as the efficient cooling of hot electrons through e - ph coupling. The slow term, on the other hand, can be explained as the bolometric process of phonon diffusion. According to the Fermi smearing model, the positive $\Delta R/R$ peak indicates a Fermi level higher than the probe energy. Hence, E_F of the oxygen-rich sample can be deduced as higher than 2.18 eV.

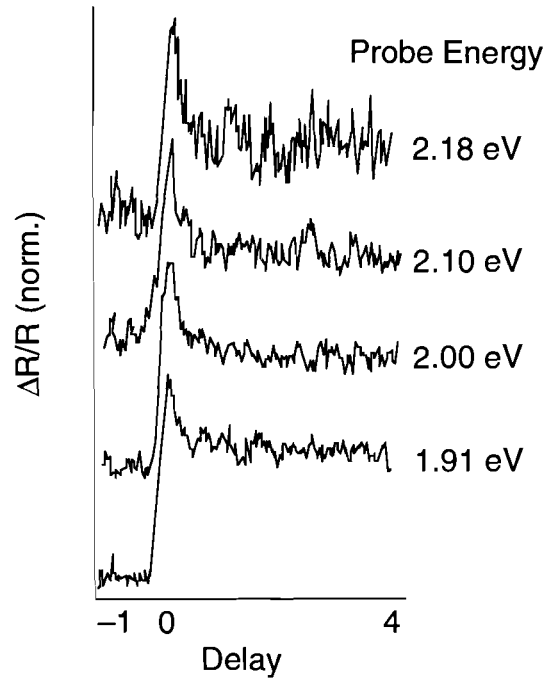


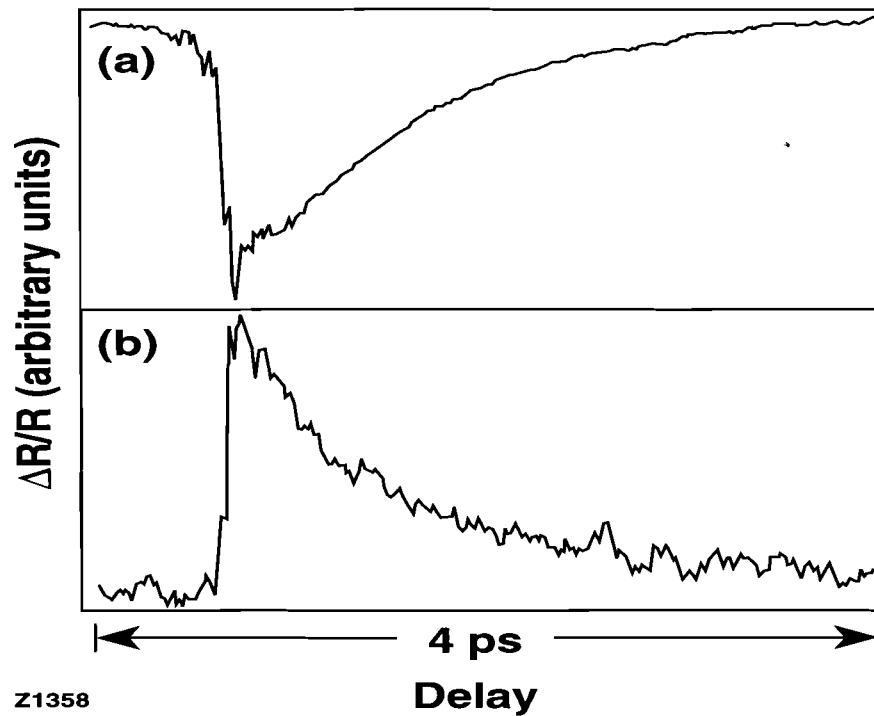
Fig. 5.20 Normalized $\Delta R/R$ ($\sim 10^{-3}$) of an oxygen-rich YBCO thin film.

5.3.5 Nonequilibrium Superconductivity

Cryogenic testing at 2-eV pump and probe energies has been performed to investigate the recovery of nonequilibrium superconductivity. Figure 5.21 presents $\Delta R/R$ at the temperature of 12 K for (a) a 280-nm thick YBCO film with $T_c=89.5$ K and (b) a 80-nm thick YBCO film with $T_c=83$ K. At low pump intensity ($\sim 1 \mu\text{J}/\text{cm}^2$), both samples display a fast recovery of $\Delta R/R$ in less than 4 ps. However, the signal sign of the optically thin sample is opposite to that of the optically thick sample. The sign reversal between the optically thick and thin samples can be explained by the thin-film effect [5.25].

Under high-level excitations, the same oxygen-rich YBCO samples behave completely differently. Figure 5.22 displays $\Delta R/R$ for a YBCO sample at two high excitation levels. At the excitation level of $\sim 20 \mu\text{J}/\text{cm}^2$, the estimated QP number is $\sim 10^{21} \text{ cm}^{-3}$, and is comparable to the total free-carrier concentration in YBCO. Thus, nearly all of the Cooper pairs are destroyed and the sample undergoes a superconducting-to-normal transition. The signal in Fig. 5.22(a) shows an instant thermalization of carriers (initial rise) followed by a fast e - ph coupling decay and a slow heat diffusion term. In fact, the transient is very similar to that observed at room

temperatures (Fig. 5.20). At the excitation level of $\sim 100 \mu\text{J}/\text{cm}^2$, the decay is dominant by the heat diffusion process [Fig. 5.22(b)].



Z1358

Fig. 5.21 Normalized $\Delta R/R$ ($\sim 10^{-4}$) at $T=25 \text{ K}$ of (a) a 280-nm thick YBCO film with $T_c=89.5 \text{ K}$ and (b) a 80-nm thick YBCO film with $T_c=83 \text{ K}$. The pump intensity was $\sim 1 \mu\text{J}/\text{cm}^2$.

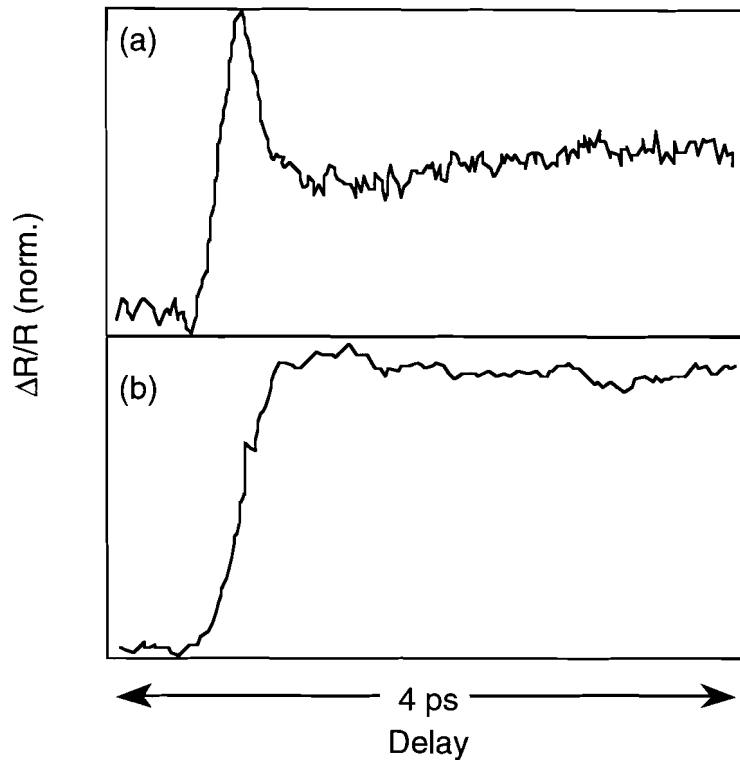


Fig. 5.22 Normalized $\Delta R/R$ ($\sim 10^{-3}$) at $T=12$ K measured on a 200-nm-thick YBCO film with $T_c=87$ K. The pump intensity was (a) $\sim 20 \mu\text{J}/\text{cm}^2$ and (b) $\sim 100 \mu\text{J}/\text{cm}^2$.

5.4 Summary

After systematic studies of the transient optical response of YBCO thin films with various oxygen contents, we obtained valuable information regarding the band structure as well as the carrier dynamics in this material.

In semiconducting YBCO, a charge-transfer gap has been directly probed. The fast relaxation below 1.9 eV is attributed to free-carrier absorption inside the broad O-2p band. Transient signals in both white-light and low-temperature measurements follow exactly a stretched-exponential decay rather than a simple exponential law. Apart from the case of multiple trapping where $\beta = T/T_0$ and $\tau \sim \exp(E_a/k_B T)$, the fits of our data show a temperature-independent β and a characteristic time τ which decreases with temperature. Therefore, our results cannot be explained by the carriers trapped in localized states. By separating the

contributions from photo-induced bleaching and free-carrier absorption, we concluded that the peak in the decay rate near 1.9 eV corresponds to the bandwidth of the O-2p band.

At low oxygen doping level, the 30-K film displays a PB as a result of band filling across the CT gap. With further oxygen doping, the 55-K and 60-K samples show that signal sign depends strongly on the pump intensity. The intensity dependence of the signal sign is found to be in contrary to the standard Fermi smearing model. However, it can be explained by Fermi smearing if photodoping is considered in partially oxygen-depleted samples. Intensity dependence is expected once E_F is shifted by either charge-transfer process in the CuO_2 plane or the oxygen ordering in the CuO chain layers. To minimize the intensity-dependent shift in E_F , low intensity pumping is preferred. Low intensity white-light probing indicates that the Fermi energy is below 1.91 eV in both the 55-K and 60-K samples.

Room-temperature response in fully oxygenated samples is found to follow the nonequilibrium electron heating model previously developed for d-band metals. The fast component corresponds to the energy loss of electrons through $e-ph$ coupling and the slow term represents the bolometric heat diffusion process. The Fermi level in the 90-K sample is found to be above 2.18 eV.

At temperatures below T_c , the response of superconducting YBCO depends drastically on the pump intensity. At low excitation levels ($\sim 1 \mu\text{J}/\text{cm}^2$), nonbolometric response is observed, with a sign difference between the optically thin and thick films. At high excitation levels ($> 15 \mu\text{J}/\text{cm}^2$), bolometric response appears as a result of excess QP generation that destroy the superconductivity. In the latter case, the response is identical to that observed at room temperature and again can be explained with the help of nonequilibrium electron heating.

References

Femtosecond Lasers

- [5.1] R. L. Fork, C. V. Shank, R. Yen, and C. A. Hirlimann, "Femtosecond optical pulses," *IEEE J. Quantum Elec.* QE-19, 500 (1983)
- [5.2] W. H. Knox, M. C. Downer, R. L. Fork, and C. V. Shank, "Amplified femtosecond optical pulses and continuum generation at 5-kHz repetition rate," *Optics Lett.* 9, 552 (1984)
- [5.3] J. A. Valdmanis, R. L. Fork, and J. P. Gordon, "Generation of optical pulses as short as 27 femtoseconds directly from a laser balancing self-phase modulation, group-velocity dispersion, saturable absorption, and saturable gain," *Optics Lett.* 10, 131 (1985)
- [5.4] J. A. Valdmanis and R. L. Fork, "Design considerations for a femtosecond pulse laser balancing self phase modulation, group velocity dispersion, saturable absorption, and saturable gain," *IEEE J. Quantum Elec.* QE-22, 112 (1986)

Pump-Probe on Semiconductors

- [5.5] C. V. Shank, R. Yen, and C. Hirliman, "Time-resolved reflectivity measurements of femtosecond-optical-pulse-induced phase transitions in silicon," *Phys. Rev. Lett.* **50**, 454 (1983)
- [5.6] G. C. Cho, W. Kütt, and H. Kurz, "Subpicosecond time-resolved coherent-phonon oscillations in GaAs," *Phys. Rev. Lett.* **65**, 764 (1990)
- [5.7] T. Gong, P. M. Fauchet, J. F. Young, and P. J. Kelly, "Femtosecond gain dynamics due to initial thermalization of hot carriers injected at 2 eV in GaAs," *Phys. Rev. B* 44, 6542 (1991)
- [5.8] P. M. Fauchet, D. Hulin, R. Vanderhaghen, A. Mourchid, and W. L. Nighan Jr., "The properties of free carriers in amorphous silicon," *J. Non-Crystal. Solids* **141**, 76 (1992)
- [5.9] A. Esser, H. Heesel, H. Kurz, C. Wang, G. N. Parsons, and G. Lucovsky, "Femtosecond spectroscopic study of ultrafast carrier relaxation in hydrogenated amorphous silicon *a*-Si:H," *J. Appl. Phys.* 73, 1235 (1993)
- [5.10] L. H. Acioli, M. Ulman, F. Vallée, and J. G. Fujimoto, "Femtosecond carrier dynamics in the presence of a cold plasma in GaAs and AlGaAs," *Appl. Phys. Lett.* **63**, 666 (1993)

Pump-Probe on Metals

- [5.11] G. L. Eesley, "Generation of nonequilibrium electron and lattice temperatures in copper by picosecond laser pulses," *Phys. Rev. B* **33**, 2144 (1986)
- [5.12] R. W. Schoenlein, W. Z. Lin, and J. G. Fujimoto, and G. L. Eesley, "Femtosecond studies of nonequilibrium electronic processes in metals," *Phys. Rev. Lett.* **58**, 1680 (1987)
- [5.13] W. S. Fann, R. Storz, H. W. K. Tom, and J. Bokor, "Direct measurement of nonequilibrium electron-energy distributions in subpicosecond laser-heated gold films," *Phys. Rev. Lett.* **68**, 2834 (1992)
- [5.14] C. K. Sun, F. Vallee, L. Acioli, E. P. Ippen, and J. G. Fujimoto, "Femtosecond investigation of electron thermalization in gold," *Phys. Rev. B* **48**, 12365 (1993)

Converting of Refractive Index

- [5.15] T. Gong, Phd dissertation, Ch. 2, p. 22, EE Dept., Princeton University, 1991

Pump-Probe on HTS

- [5.16] S. G. Han, Z. V. Vardeny, O. G. Symko, and G. Koren, "Femtosecond optical detection of quasiparticle dynamics in high- T_c $\text{YBa}_2\text{Cu}_3\text{O}_{7-\delta}$ superconducting thin films," *Phys. Rev. Lett.* **65**, 2708, (1990)
- [5.17] G. L. Eesley, J. Heremans, M. S. Meyer, and G. L. Doll, "Relaxation time of the order parameter in a high-temperature superconductor," *Phys. Rev. Lett.* **65**, 3445, (1990)
- [5.18] J. M. Chwalek, C. Uher, J. F. Whitaker, and G. A. Mourou, "Femtosecond optical absorption studies of nonequilibrium electronic processes in high T_c superconductors," *Appl. Phys. Lett.* **57**, 1696, (1990)
- [5.19] W. Albrecht, Th. Kruse, and H. Kurz, "Time-resolved observation of coherent phonons in superconducting $\text{YBa}_2\text{Cu}_3\text{O}_{7-\delta}$ thin films," *Phys. Rev. Lett.* **69**, 1451, (1992)
- [5.20] S. V. Chekalin, V. M. Farztdinov, V. V. Golovlyov, V. S. Letokhov, Yu. E. Lozovik, Yu. A. Matveets, and A. G. Stepanov, "Femtosecond spectroscopy of $\text{YBa}_2\text{Cu}_3\text{O}_{7-\delta}$: electron-phonon-interaction measurement and energy-gap observation," *Phys. Rev. Lett.* **67**, 3860, (1991)
- [5.21] S. D. Brorson, A. Kazeroonian, J. S. Moodera, D. W. Face, T. K. Cheng, E. P. Ippen, M. S. Dresselhaus, and G. Dresselhaus, "Femtosecond room-temperature measurement of the electron-phonon coupling constant λ in metallic superconductors," *Phys. Rev. Lett.* **64**, 2172, (1990)
- [5.22] D. W. Face, S. D. Brorson, A. Kazeroonian, J. S. Moodera, T. K. Cheng, G. L. Doll, M. S. Dresselhaus, G. Dresselhaus, E. P. Ippen, T. Venkatesan, X. D.

- Wu, and A. Inam, "Femtosecond thermomodulation studies of low and high- T_c superconductors," *IEEE Trans. Mag.* **Mag-27**, 1556, (1991)
- [5.23] A. S. Kazeroonian, T. K. Cheng, S. D. Brorson, Q. Li, E. P. Ippen, X. D. Wu, T. Venkatesan, S. Etemad, M. S. Dresselhaus, and G. Dresselhaus, "Probing the Fermi level of $Y_{1-x}Pr_xBa_2Cu_3O_{7-\delta}$ by femtosecond spectroscopy," *Solid State Commun.* **7**, 95, (1991)
- [5.24] D. H. Reitze, A. M. Weiner, A. Inam, and S. Etemad, "Fermi-level dependence of femtosecond response in nonequilibrium high- T_c superconductors," *Phys. Rev. Lett.* **46**, 14306, (1992)
- [5.25] T. Gong, L. X. Zheng, W. Xiong, W. Kula, Y. Kostoulas, R. Sobolewski, and P. M. Fauchet, "Femtosecond optical response of Y-Ba-Cu-O thin films: the dependence on optical frequency, excitation intensity, and electric current," *Phys. Rev. B* **47**, 14495, (1993)
- [5.26] W. Albrecht, Th. Kruse, K. Leo, and H. Kurz, "Oxygen dependence of the Fermi-level and electron-phonon coupling constant in $YBa_2Cu_3O_x$ films," *Appl. Phys. A* **56**, 463, (1993)
- [5.27] L. Shi, T. Gong, W. Xiong, X. Weng, Y. Kostoulas, R. Sobolewski, and P. M. Fauchet, "Femtosecond reflectivity of 60 K Y-Ba-Cu-O thin films," *Appl. Phys. Lett.* **64**, 1150, (1994)
- [5.28] A. L. Dobryakov, V. V. Golovlev, V. S. Letokhov, Y. E. Lozovik, Y. A. Matveets, A. G. Stepanov, V. M. Farztdinov, and S. V. Chekalin, "Femtosecond spectroscopy of $YBa_2Cu_3O_{7-\delta}$ superconductors. Measurement of the electron-phonon coupling parameter and observation of the superconducting gap," *Optics and Spectroscopy*, **76**, 871 (1994)
- [5.29] W-S. Zeng, W-Z. Lin, D. Mo, F. P. Pi, Z-J. Xia, Y-H. Zhou, and G-C. Xiong, Z. "Femtosecond relaxation dynamics of electronic processes and electron-phonon coupling in $YBa_2Cu_3O_{7-\delta}$ and $PrBa_2Cu_3O_7$ epitaxial films," *Phys. B* **96**, 5 (1994)
- [5.30] K. Matsuda, I. Hirabayashi, K. Kawamoto, and T. Nabatame, T. Tokizaki, and A. Nakamura, "Femtosecond spectroscopic studies of the ultrafast relaxation process in the charge-transfer state of insulating cuprates," *Phys. Rev. B* **50**, 4097 (1994)

Raman Spectra

- [5.31] E. T. Heyen, J. Kircher, and M. Cardona, "Resonant Raman scattering in insulating $YBa_2Cu_3O_6$ as a probe of its electronic structure," *Phys. Rev. B* **45**, 3037 (1992)

- [5.32] R. Liu, D. Salamon, M. V. Klein, S. L. Cooper, W. C. Lee, S-W. Cheong, and D. M. Ginsberg, "Novel Raman-active electronic excitations near the charge-transfer gap in insulating cuprates," *Phys. Rev. Lett.* **71**, 3709 (1993)

Photoconductivity

- [5.33] G. Yu, A. J. Heeger, G. Stucky, N. Herron, and E. M. McCarron, L. Cong, G. C. Spalding, C. A. Nordman, and A. M. Goldman, "Phase separation of photogenerated carriers and photoinduced superconductivity in high- T_c materials," *Phys. Rev. B* **45**, 4964 (1992)
- [5.34] G. Yu, C. H. Lee, D. Mihailovic, A. J. Heeger, C. Fincher, N. Herron, and E. M. McCarron, "Photoconductivity in insulating $YBa_2Cu_3O_{6+x}$: from Mott-Hubbard insulator to Fermi glass via oxygen doping," *Phys. Rev. B* **48**, 7545 (1993)

Photoluminescence

- [5.35] V. N. Denisov, C. Taliani, A. G. Mal'shukov, V. M. Burlakov, E. Schönherr, and G. Ruani, "Infrared-excited Raman scattering and photoluminescence of deep intragap states in semiconducting $YBa_2Cu_3O_{6+x}$," *Phys. Rev. B* **48**, 16714 (1993)

Stretched Exponential

- [5.36] H. Scher, M. F. Shlesinger, and J. T. Bendler, "Time-scale invariance in transport and relaxation," *Physics Today*, **Jan.**, p. 26, 1991
- [5.37] R. A. Street, in *Hydrogenated Amorphous Silicon*, p.203, (Cambridge University Press, Cambridge, 1991)

Photodoping

- [5.38] G. Nieva, E. Osquiguil, J. Guimpel, M. Maenhoudt, B. Wuyts, Y. Bruynseraede, M. B. Maple, and I. K. Schuller, "Photoinduced enhancement of superconductivity," *Appl. Phys. Lett.* **60**, 2159 (1992)
- [5.39] E. Osquiguil, M. Maenhoudt, B. Wuyts, Y. Bruynseraede, D. Lederman, and I. K. Schuller, "Photoexcitation and oxygen ordering in $YBa_2Cu_3O_x$ films," *Phys. Rev. B* **49**, 3675 (1994)
- [5.40] V. I. Kudinov, I. L. Chaplygin, A. I. Kirilyuk, N. M. Kreines, R. Laiho, E. Lähderanta, and C. Ayache, "Persistent photoconductivity in $YBa_2Cu_3O_{6+x}$ films as a method of photodoping toward metallic and superconducting phases," *Phys. Rev. B* **47**, 9017 (1993)

6 CONCLUSIONS

Fabrication techniques as well as optical response of HTS YBCO thin films have been investigated in this work.

High quality YBCO thin films have been deposited on various substrates using *in-situ* RF magnetron sputtering. Superconducting properties of the sputtered YBCO films have been monitored by performing cryogenic testing. YBCO samples with various oxygen contents have been fabricated by a controlled high-temperature annealing in either vacuum or flowing Ar/N₂. Microbridges, coplanar striplines and waveguides have been photolithographically patterned and lifted off.

For non-destructive patterning of YBCO films, a laser-writing technique has been developed to selectively modify the phases of YBCO on highly localized area. Laser-assisted oxygen *in-* and *out-*diffusion have been successfully implemented for patterning oxygen-rich (superconducting) or oxygen-depleted (semiconducting) features. The oxygen-rich patterns demonstrated the superconducting properties identical to that of the as-deposited films, whereas the oxygen-deplete lines display a typical semiconducting transport which can be characterized by Mott's variable-range hopping. Linear resistive characteristics has been observed at the interface between the superconducting and semiconducting YBCO. The ability of erasing and rewriting of laser-written YBCO patterns provides great flexibility for circuit restructuring and error correction in YBCO circuit design. Laser writing is also capable of modifying the oxygen content of YBCO through a SrTiO₃ top layer. Microwave testing has confirmed the low loss of coplanar transmission lines patterned by laser writing. Photoconductive investigation of a laser-written switch indicated a long lifetime of photoexcited carriers in semiconducting YBCO. Long-term (up to 2 years) stability has been observed in our laser-written patterns. Moreover, laser writing enables the patterning of YBCO structures without expensive photomasks and vacuum systems.

Femtosecond pump-probe experiments have been performed on YBCO thin films with several different oxygen contents. Photoresponse in semiconducting YBCO corresponds to the band filling across the CT gap. Instead of the expected slower relaxation towards the band edge, an abrupt increase in the relaxation appears below 1.9 eV. We assign this behavior to free-carrier absorption inside the broad O-2p band. By separating the contributions from photo-induced bleaching and free-carrier absorption, we conclude that the peak in the decay rate near 1.9 eV corresponds to the bandwidth of the O-2p band.

Transient signals in both white-light and low-temperature measurements follow a stretched-exponential decay rather than a simple exponential. Unlike in the case of multiple trapping where $\beta = T/T_0$ and $\tau \sim \exp(E_a/k_B T)$, the fits of our data show a temperature-independent β and a characteristic time τ which decreases with temperature. Therefore, our results cannot be related to the carriers trapped in localized states.

PB signals of 30-K film are very similar to those of semiconducting YBCO, indicating band-filling dominant response. Because of the low oxygen doping level, the contribution from Fermi smearing is negligible. At the intermediate doping level, the response of 55-K and 60-K samples follows the Fermi smearing model except the observed dependence of the $\Delta R/R$ sign on the pump intensity. The intensity dependence is attributed to the shift in Fermi level by photodoping effect. Therefore, low-intensity measurements are believed to reflect more accurately the original position of E_F in the sample. White-light probing at low intensities indicates that the Fermi energy is below 1.91 eV for YBCO samples with T_c near 60 K.

Room-temperature response in fully oxygenated YBCO samples is found to follow the nonequilibrium electron heating model. The fast component corresponds to the energy loss of electrons through electron-phonon coupling and the slow term represents the bolometric heat diffusion process. The Fermi level in the 90-K sample is found to be above 2.18 eV.

At temperatures below T_c , nonequilibrium superconductivity in YBCO has been also investigated. The response is found to be dependent on the excitation level. For low pump intensity, nonbolometric, picosecond response is observed. Due to the thin film effect, a positive $\Delta R/R$ appears in optically thin films and the negative $\Delta R/R$ in optically thick films. At high pump intensity, however, bolometric response occurs even at $T \ll T_c$. This effect is due to the destruction of the superconducting state by excessive QP generation. The bolometric term corresponds to the slow heat diffusion process.